FEDERAL UNIVERSITY OF PERNAMBUCO
CENTER OF TECHNOLOGY AND GEOSCIENCES
DEPARTMENT OF CIVIL ENGINEERING
GRADUATE COURSE IN CIVIL ENGINEERING

TÚLIO DE MOURA CAVALCANTE

SIMULATION OF IMMISCIBLE TWO-PHASE FLOW IN 3-D NATURALLY FRACTURED RESERVOIRS USING A LOCALLY CONSERVATIVE METHOD, A PROJECTION-BASED EMBEDDED DISCRETE FRACTURE MODEL AND UNSTRUCTURED TETRAHEDRAL MESHES

Recife
2023

TÚLIO DE MOURA CAVALCANTE

SIMULATION OF IMMISCIBLE TWO-PHASE FLOW IN 3-D NATURALLY FRACTURED RESERVOIRS USING A LOCALLY CONSERVATIVE METHOD, A PROJECTION-BASED EMBEDDED DISCRETE FRACTURE MODEL AND UNSTRUCTURED TETRAHEDRAL MESHES

Thesis submitted to the Graduate Course in Civil Engineering of the Federal University of Pernambuco in partial fulfilment to obtain the degree of Doctor of Philosophy in Civil Engineering.

Concentration Area: Simulation and Management of Oil Reservoirs.

Advisor: Paulo Roberto Maciel Lyra, PhD.

Co-advisor: Darlan Karlo Elisiário de Carvalho, PhD.

Recife

2023

Catalogação na fonte:
Bibliotecária Sandra Maria Neri Santiago, CRB-4 / 1267

C377s Cavalcante, Túlio de Moura.
Simulation of immiscible two-phase flow in 3-D naturally fractured reservoirs using a locally conservative method, a projection-based embedded discrete fracture model and unstructured tetrahedral meshes / Túlio de Moura Cavalcante. – 2023.
142 f.: il., fig., tab. e siglas.

Orientador: Prof. Dr. Paulo Roberto Maciel Lyra.
Coorientador: Prof. Dr. Darlan Karlo Elisiário de Carvalho.
Tese (Doutorado) – Universidade Federal de Pernambuco. CTG. Programa de Pós-Graduação em Engenharia Civil. Recife, 2023.
Inclui referências.

1. Engenharia civil. 2. Simulação numérica. 3. Escoamento bifásico de água e óleo. 4. Reservatórios heterogêneos e anisotrópicos. 5. Reservatórios fraturados. 6. pEDFM. 7. MPFA-D. 8. DMP. I. Lyra, Paulo Roberto Maciel (Orientador). II. Carvalho, Darlan Karlo Elisiário de (Coorientador). III. Título.

UFPE

624 CDD (22. ed.) BCTG/2023-70

TÚLIO DE MOURA CAVALCANTE

SIMULATION OF IMMISCIBLE TWO-PHASE FLOW IN 3-D NATURALLY FRACTURED RESERVOIRS USING A LOCALLY CONSERVATIVE METHOD, A PROJECTION-BASED EMBEDDED DISCRETE FRACTURE MODEL AND UNSTRUCTURED TETRAHEDRAL MESHES

Tese apresentada ao Programa de Pós-Graduação em Engenharia Civil da Universidade Federal de Pernambuco, Centro de Tecnologia e Geociências, como requisito para obtenção do título de Doutor em Engenharia Civil, Área de Simulação e Gerenciamento de Reservatórios de Petróleo.

Aprovada em 10/03/2023

Orientador: Prof. Dr. Paulo Roberto Maciel Lyra – UFPE
Coorientador: Prof. Dr. Darlan Karlo Elisiário de Carvalho - UFPE

BANCA EXAMINADORA

participação por videoconferênc
Prof. Dr. Ramiro Brito Willmersdorf (examinador interno)
Universidade Federal de Pernambuco

participação por videoconferência
Prof. Dr. Philippe Remy Bernard Devloo (examinador externo)
Universidade Estadual de Campinas

participação por videoconferência
Prof. Dr. Márcio Arab Murad (examinador externo)
Laboratório Nacional de Computação Cientifica

participação por videoconferênc
Prof. Dr. Márcio Rodrigo de Araújo Souza (examinador externo)
Universidade Federal da Paraíba

participação por videoconferência
Prof. Dr. Igor Fernandes Gomes (examinador interno)
Universidade Federal de Pernambuco

Do Senhor muitos dons eu recebi,
A esperteza do cálculo e do texto,
Livramento da fome e do cabresto,
Foi de graça e não porque mereci.
Não teria com o que retribuir,
Mas dedico-Lhe a tese apresentada,
Que não traz grande coisa revelada,
Mas que a alguém vai servir alguma vez.
Grande é Deus que, do nada, tudo fez
E eu, com tudo nas mãos, não faço nada.

ACKNOWLEDGMENTS

I thank God for having kept me alive and healthy, without myself having done anything to deserve such grace.

I would like to thank my parents, Geraldo and Ângela, for their examples of determination, appreciation for knowledge and honesty and for providing me with a solid academic education since an early age.

I thank my brother Douglas for his usual fellowship.

I thank my beloved Thayane for being my strength, no matter the circumstances.

I would like to thank professors Darlan and Paulo Lyra for their guidance and help in the development of this research work, as well as in writing this and all other texts that resulted from this work.

I thank the other researchers who contributed to this work, namely, Artur Castiel, Ricardo Lira Filho and Twany Correia, beyond prof. Hadi Hajibeygi.

I thank FACEPE for funding this work and the people of Pernambuco for funding FACEPE.

Agradeço a Deus por ter me guardado vivo e saudável, sem que eu tenha feito nada para merecer tamanha graça.

Agradeço aos meus pais, Geraldo e Ângela, pelos exemplos de determinação, de apreço pelo conhecimento e de honestidade e por terem me oportunizado uma formação acadêmica sólida desde muito cedo.

Agradeço ao meu irmão Douglas pelo companheirismo de sempre.

Agradeço à minha amada Thayane por ser minha força, não importando as circunstâncias.

Agradeço aos professores Darlan e Paulo Lyra pela orientação e pela ajuda no desenvolvimento desse trabalho de pesquisa, bem como na escrita desse e de todos os outros textos que foram frutos do trabalho.

Agradeço aos outros pesquisadores que contribuíram com esse trabalho, a saber, Artur Castiel, Ricardo Lira Filho e Twany Correia, além do prof. Hadi Hajibeygi.

Agradeço à FACEPE por financiar esse trabalho e ao povo de Pernambuco, por financiar a FACEPE.

RESUMO

O escoamento de fluidos em meios porosos fraturados é um fenômeno muito relevante, pois a maior parte das reservas de petróleo remanescentes no mundo residem neste tipo de formações, além de as fraturas também estarem presentes em camadas menos profundas da crosta, o que as torna influentes também na extração de água e na dispersão de resíduos. O escoamento bifásico de água e óleo em reservatórios pode ser descrito matematicamente por um conjunto de equações diferenciais parciais não-lineares, cuja modelagem constitui-se num grande desafio, devido à complexidade dos ambientes deposicionais, além da presença das fraturas. Nesses casos, é particularmente complexo construir malhas computacionais estruturadas capazes de representar adequadamente o reservatório. No presente trabalho, uma nova estratégia foi desenvolvida para simular o escoamento bifásico imiscível em meios porosos fraturados 3-D, usando malhas não-estruturadas tetraédricas. Tal estratégia é baseada em um método de volumes finitos com aproximação de fluxo por múltiplos pontos que utiliza o chamado "estêncil de diamante" (MPFA-D), considerando um modelo de fratura discreta embutida baseado em projeção (pEDFM) para incluir as influências das fraturas no modelo global do reservatório. O MPFA-D é uma formulação robusta e flexível, capaz de lidar com tensores de difusão altamente heterogêneos, possivelmente descontínuos, e anisotrópicos, inclusive não-ortotrópicos, e que alcança taxas de convergência de segunda ordem para a variável escalar e de primeira ordem para o seu gradiente. No entanto, como outros métodos MPFA lineares, ele não garante formalmente soluções monótonas ou que respeitem o Princípio do Máximo Discreto (DMP) e pode produzir oscilações espúrias no campo de pressão para tensores de permeabilidade com razão de anisotropia elevada ou para malhas distorcidas. Para lidar com este problema e impor a observância do DMP, foi desenvolvida uma alternativa de correção não-linear para o MPFA-D. Além disso, o modelo de fratura adotado evita a complexidade adicional de alinhar fraturas com arestas ou faces da malha computacional que discretiza o domínio correspondente ao meio poroso, tornando a construção dessa malha mais flexível e menos suscetível a refinamentos localizados excessivos. Os termos de saturação do modelo matemático são discretizados segundo o método de Euler avançado, no contexto de um esquema numérico totalmente implícito. Os métodos numéricos propostos, bem como o simulador composto por eles, foram testados frente a problemas encontrados na literatura e outros elaborados

pelo autor, visando demonstrar a robustez e a flexibilidade da ferramenta de simulação computacional desenvolvida.

Palavras-chave: Simulação numérica; Escoamento bifásico de água e óleo; Reservatórios heterogêneos e anisotrópicos; Reservatórios Fraturados; pEDFM; MPFA-D; DMP.

ABSTRACT

Fluid flow in fractured porous media is a very relevant phenomenon, since most of the remaining oil reserves in the world reside in this type of formations, in addition to the fact that fractures are also present in shallower layers of the crust, which makes them influential also in water extraction and waste dispersion. The two-phase flow of oil and water in reservoirs can be mathematically described by a set of non-linear partial differential equations, whose modeling constitutes a great challenge, due to the complexity of the depositional environments, in addition to the presence of fractures. In these cases, it is particularly complex to construct structured computational meshes capable of adequately representing the reservoir. In the present work, a new strategy was developed to simulate immiscible two-phase flow in 3-D fractured porous media, using tetrahedral unstructured meshes. Such a strategy is based on a finite volume method with multipoint flux approximation that uses the so-called "diamond stencil" (MPFA-D), considering a projection-based embedded discrete fracture model (pEDFM) to include the influences of the fractures in the global reservoir model. The MPFA-D is a robust and flexible formulation, capable of handling highly heterogeneous, possibly discontinuous, and anisotropic, even non-orthotropic, diffusion tensors, and which achieves second-order convergence rates for the scalar variable and first-order convergence rates for its gradient. However, like other linear MPFA methods, it does not formally guarantee monotonic solutions or those that respect the Discrete Maximum Principle (DMP) and can produce spurious oscillations in the pressure field for permeability tensors with high anisotropy ratio or for distorted meshes. To deal with this problem and enforce DMP compliance, an alternative non-linear defect correction for MPFA-D was developed. Furthermore, the adopted fracture model avoids the additional complexity of aligning fractures with edges or faces of the computational mesh that discretizes the domain corresponding to the porous medium, making the construction of this mesh more flexible and less susceptible to excessive localized refinements. The saturation terms of the mathematical model are discretized according to the backward Euler method, in the context of a fully implicit numerical scheme. The proposed numerical methods, as well as the simulator composed by them, were tested against problems found in the literature and others elaborated by the author, aiming to demonstrate the robustness and flexibility of the developed computational simulation tool.

Keywords: Numerical simulation; Two-phase flow of oil and water; Heterogeneous and anisotropic reservoirs; Fractured Reservoirs; pEDFM; MPFA-D; DMP.

LIST OF FIGURES

LIST OF TABLES

LIST OF ACRONYMS

CDT	Cross Diffusion Terms.
CV	Control Volume.
DMP	Discrete Maximum Principle
EDFM	Embedded Discrete Fracture Model.
FIM	Fully Implicit Method.
FVM	Finite Volume Method
MPFA	Multi-Point Flux Approximation.
MPFA-D	Multi-Point Flux Approximation with “Diamond” Stencil.
MPFA-DNL	Multi-Point Flux Approximation with “Diamond” Stencil and Non-Linear Defect Correction.
pEDFM	Projection-Based Embedded Discrete Fracture Model.
TPFA	Two-Point Flux Approximation.

LIST OF SYMBOLS

ϕ	Rock Porosity.
S_α	Saturation of phase α.
$k_{r\alpha}$	Relative permeability of phase α.
$\mathbf{K}$	Permeability tensor.
ρ_α	Density of phase α.
$c_{f\alpha}$	Compressibility of phase α.
μ_α	Viscosity of phase α.
λ_α	Mobility of phase α.
Ω_m	Domain representing the rock matrix.
Ω_{f_k}	Domain representing the k-th fracture within Ω_m.
n	Amount of something.
$\hat{k}$	k-th tetrahedron discretizing Ω_m.
$\check{k}_i$	i-th polygon discretizing Ω_{f_k}.
$\Omega_{\hat{k}}$	Volume of cell $\hat{k}$.
$\Omega_{\check{k}_i}$	Area of cell $\check{k}_i$.
k	k-th vertex of the mesh discretizing Ω_m.
$\bar{k}$	k-th face of the mesh discretizing Ω_m.
$\vec{N}_{\bar{k}}$	Area normal vector to $\bar{k}$.
$\vec{n}_{\bar{k}}$	Unitary normal vector to $\bar{k}$.

CONTENTS

1 INTRODUCTION

This first chapter briefly presents all the topics covered in this work, from the problem that motivated it to the proposed solutions. Beyond this, it summarizes the objectives and the organization of this thesis.

1.1 SIMULATION OF FLUID FLOW IN RESERVOIRS

A reservoir rock is a subsurface mineral volume having sufficient porosity and permeability that allow the migration and accumulation of hydrocarbons under adequate conditions (MAGOON, 2004). The fluids displacements in this type of environment is a very relevant phenomenon for mankind and its simulation is a very important tool in order to get information that permit the proper management of the hydrocarbons production, maximizing the economic return of the process (PEACEMAN, 1977; EWING, 1983; CHEN; HUAN; MA, 2006). Among the many strategies for extracting oil, there is the strategy in which water is injected to maintain a high pressure in the reservoir and keep continuously forcing the hydrocarbons out. In this case, assuming that the pressure of the reservoir does not drops sufficiently to lead to the appearance of a gas phase, this process can be simplified as a two-phase flow, that is the object of study of this work, and which, after considering some simplifying hypotheses, can be mathematically described as a set of nonlinear partial differential equations.

It should be noted that the majority of the remaining exploitable reservoirs around the world are fractured structures (BEYDOUN, 1998), in addition to the fact that fractures are also present in less deep layers of the crust, which makes them also influential in water extraction and waste dispersion (MATTHÄI, 2018). In this context, the influence of the presence of the fractures on the two-phase flow must be correctly considered, since it potentially introduces discontinuities on the pressure and/or on the velocity fields (MARTIN; JAFFRÉ; ROBERTS, 2005). Modeling this problem represents a great challenge, because depositional environments are geometrically complex media, in which some properties (e.g., permeability) may vary many orders of magnitude over small distances, in addition to the presence of the fractures themselves (CRUMPTON; SHAW; WARE, 1995; CARVALHO; WILLMERSDORF; LYRA, 2009). These environments are usually anisotropic, since the sedimentary layers can be deposited in different ways, giving different preferential directions to the fluids flows (CARVALHO; WILLMERSDORF; LYRA, 2009; CAVALCANTE et al., 2020), what

makes particularly complex, in such cases, to construct structured meshes aiming to model them (AAVATSMARK et al., 1998a).

1.2 MODELING FRACTURED RESERVOIRS

There are many strategies developed to handle these fractures in the context of simulation of fluid flow in porous media. Among these schemes, traditional methods, which do not treat the fractures as additional degrees of freedom, have some remarkable limitations. Transmissibility multipliers, for example, are very dependent on the mesh (MANZOCCHI et al., 1999; NILSEN; LIE; NATVIG, 2012); Dual-continuum models (BARENBLATT; ZHELTOV; KOCHINA, 1960; WARREN; ROOT, 1963; KAZEMI et al., 1976) require a very complex basis of parameters to guarantee a precise solution and are still not capable to deal with high fracture density and localized anisotropy, while the models that represent fractures explicitly may be more accurate and "physics oriented" (HOTEIT; FIROOZABADI, 2008). Also, the explicit discrete fracture representation may be more suitable for multiphase flow problems, because if the constitutive relations for capillary pressures and relative permeabilities are known, they can be included directly into the models (BERRE; DOSTER; KEILEGAVLEN, 2019).

The word "fracture" may be used to represent a discontinuity in porous media throughout various length of scales, from a few millimeters to hundreds of meters. It is not feasible to handle all types of fractures explicitly. Thus, fractures are usually classified according to their length (or characteristic length), so that the small-scale ones are treated through some kind of homogenization (upscaling) method, while the large-scale ones are represented explicitly (LEE; LOUGH; JENSEN, 2001; LI; LEE, 2008). The present research focuses on large-scale fractures.

Explicit fracture representation methods can be divided into two groups, based on the type of the discretization: conforming mesh and non-conforming mesh methods. For the first group, the mesh needs to accommodate the fracture positions, which are placed at the cell edges (in 2-D) or faces (in 3-D). This condition is critical when it is necessary to discretize small angles and small distances and can lead to excessive mesh refinements. This is not necessary for the second group, in which the fractures may cross the rock matrix mesh cells.

The second group is less restrictive in terms of mesh construction, so that the fractures may cross the rock matrix mesh cells. In this context, there are the embedded

discrete fracture models (EDFM) (LI; LEE, 2008; MOINFAR et al., 2014; SHAKIBA; SEPEHRNOORI, 2015), in which the degrees of freedom of the rock matrix and fractures are discretized separately, but the structure of the coupling is similar to that of dual-continuum methods, with the difference that the coupling term is modeled directly in terms of discrete variables directly (BERRE; DOSTER; KEILEGAVLEN, 2019).

The EDFM produce good solutions for high permeability fractures, however, their application is limited whenever the fracture permeability is much lower than that of the rock matrix. In order to overcome the limitations of EDFM, the projection-based embedded discrete fracture models (pEDFM) (JIANG; YOUNIS, 2017; ŢENE et al., 2017; RAO et al., 2020) were developed. Based on the projections of the areas of fractures on some faces of the cells in which they are contained, this strategy computes the interaction between the fractures and the neighboring cells sharing those faces that receive the projections, enriching the model.

The pEDFM itself also evolved in order to overcome other limitations. From the original method (ŢENE et al., 2017), Jiang and Younis (2017) proposed two modifications: a generalized formula for the effective flow area of the modified matrix-matrix connection and a new fracture-matrix transmissibility calculation aiming to avoid the flow between a fracture contained in a ultra-low permeability cell and its neighboring cells. Rao et al. (2020) proposed another modification of the fracture-matrix transmissibility calculation to avoid the flow from a high permeability fracture through a neighbor cell containing a ultra-low permeability fracture, and included fracture-fracture interactions in their model, enriching the pEDFM again. Besides, they have presented a new strategy to choose the cell face for the fractures areas projections. Recently, the pEDFM has been extended to be applied on corner-point grids (HOSSEINIMEHR et al., 2022), which are still structured computational meshes. In this work, the EDFM and a simplified version of the pEDFM were applied to include, in our model, the influences of the fractures in the fluid flow, using flexible unstructured tetrahedral meshes for the first time in literature.

The transmissibility terms and flux expressions corresponding to matrix-matrix, matrix-fracture and fracture-fracture interactions risen from the proposed EDFM and pEDFM will be applied in the numerical formulation developed in this work for the simulation of biphasic flows in fractured reservoirs.

1.3 NUMERICAL FORMULATIONS

The equations governing the phenomenon of interest in this text, after several simplifying considerations, are obtained combining the mass conservation law and the Darcy's law. The resulting mathematical model, in which phase saturation and phase pressure are functions of time and spatial position, is addressed in Chapter 2.

Discretizing the pressure terms of this mathematical model may represent a challenging problem for traditional numerical methods, such as the classical Two Point Flux Approximation (TPFA) Finite Volume Method (FVM), which is monotone (KEILEGAVLEN; AAVATSMARK, 2011), but it does not even guarantees convergence for general full diffusion tensors or non k-orthogonal meshes (AAVATSMARK et al., 1998a, 1998b; EDWARDS; ROGERS, 1998). On the other hand, the Galerkin Finite Element Method (GFEM) (CROSS, 1985; CIARLET, 2002), the Mixed-Finite Element Method (MFEM) (RAVIART; THOMAS, 1977; DURÁN, 2008) or even the sturdier linear Multipoint Flux Approximation (MPFA) formulations (AAVATSMARK et al., 1998a, 1998b, 2008; EDWARDS; ROGERS, 1998; AAVATSMARK, 2002; KLAUSEN; EIGESTAD, 2004; CHEN et al., 2008; GAO; WU, 2011) are commonly convergent for arbitrary diffusion tensors and general meshes, but may transgress the Discrete Maximum Principle (DMP), generating spurious oscillations for the scalar pressure field and incorrect fluxes when performing more extreme tests with high anisotropy ratios or distorted meshes (KEILEGAVLEN; AAVATSMARK, 2011) or even the presence of discontinuities, as fractures.

A notable example is the MPFA which uses diamond stencil (MPFA-D) (GAO; WU, 2011; CONTRERAS et al., 2016; LIRA FILHO et al., 2021), which is a locally conservative linearity-preserving finite volume method developed to be applicable to any polygonal 2-D meshes and general heterogeneous, possibly discontinuous, full-tensor diffusion coefficients. In this scheme, the vertex unknowns are interpolated as a weighted average of the neighboring cell-centered unknowns, from the impositions of flux continuity and the divergence-free field condition, considering an auxiliary control volume, in order to obtain a fully cell-centered formulation. In 2-D, the MPFA-D scheme has second order accuracy for the pressure field and more than first order accuracy for fluxes (GAO; WU, 2011). Even though it is very robust for problems involving high anisotropy and distorted meshes, it is not monotone and may therefore violate DMP (QUEIROZ et al., 2014; CONTRERAS et al., 2016).

In the context of 3-D models, there are, in literature, different vertex-centered and cell-centered finite volume formulations developed to discretize the diffusion terms. The control-volume based finite element method (CVFEM) (BALIGA; PATANKAR, 1980, 1988; HSU, 1981; MALISKA, 1995), for example, was, from the beginning, designed to be extensible to 3-D (MUIR; RABI BALIGA, 1986). Aavatsmark et al. (AAVATSMARK; BARKVE; MANNSETH, 1998; AAVATSMARK et al., 2001; AAVATSMARK; EIGESTAD; KLAUSEN, 2007) presented and studied the convergence behavior of the extension to 3-D of their original MPFA method on structured grids. Hermeline (2007, 2009) proposed two different ways to extend the discrete duality finite volume (DDFV) (ANDREIANOV; BOYER; HUBERT, 2007) to 3-D. The second one (HERMELINE, 2009) is locally conservative, presenting second order accuracy for the scalar variable, and, at least, first order accuracy for fluxes on all tested polyhedral meshes, even for distorted and non-matching grids. Pal and Edwards (2007) presented an extension to 3-D of the family of Control Volume Distributed MPFA (CVD-MPFA) methods which is applicable to different types of polyhedral meshes. They present convergence tests emphasizing the quadrature parametrization, with second order accuracy for the scalar variable and first order accuracy for gradients, achieving "super convergence" depending on the mesh and the chosen support region. Besides, they have presented monotonicity studies, showing the optimal quadrature condition to minimize, but not necessarily eliminate, spurious oscillations. Wolff et al. (2013) presented an extension to 3-D of the well-known L-method (AAVATSMARK et al., 2008), with interesting results compared with the classical linear TPFA method. Gao and Wu (WU; GAO, 2014; GAO; WU, 2015), developed, using the linearity-preserving criterion, an interpolation-based and positivity-preserving nonlinear two-point flux approximation finite volume method (NLFV-TPFA) for unstructured polygonal meshes, which is also extensible for 3-D applications. For smooth problems, their scheme presents second order accuracy for the scalar variable and first order accuracy for gradients. Another nonlinear monotone finite volume scheme was developed by Lian, Sheng and Yuan (2017), with their own way of eliminating the vertex unknowns in the context of a diamond scheme and which is applicable for unstructured tetrahedral meshes. Wang, Hang and Yuan (2017) presented their pyramid scheme applicable to polyhedral meshes, showing second order accuracy in several problems with scalar diffusion coefficients, including discontinuous or non-linear ones. Yang and Gao (2019) proposed a finite volume scheme with another explicit interpolation strategy for the vertex unknowns. Their formulation

presents second-order accuracy for the scalar variable and higher than first order accuracy for fluxes on some 2-D and 3-D meshes. Lira Filho et al. (2021) presented a tridimensional extension of the MPFA-D with explicit weighting for the vertex unknowns, showing second-order accuracy for the scalar variable and first order accuracy for its gradient on arbitrary tetrahedral meshes. As in the original 2-D version of Gao and Wu (2011), the method is unable to fulfill the DMP for challenging applications. Finally, Dong and Kang (2021, 2022) presented a least square based interpolation for MPFA-D, which is more robust than previous strategies in terms of handling full tensors and ensuring the DMP, but that still does not guarantee satisfying this condition for all cases.

The efforts to overcome these limitations are not recent. The DMP satisfaction for finite elements approximations was addressed by Ciarlet and Raviart (1973), Korotov, Křížek and Neittaanmäki (2000) and Burman and Ern (2004). Le Potier (2005, 2009) presented a non-linear FVM satisfying the DMP and Cancès, Cathala and Le Potier (2013) presented a non-linear technique to correct a general FVM in order to satisfy the DMP. Pal and Edwards (2006, 2011) proposed flux-splitting strategies to improve the monotonicity behavior of FVM and impose DMP compliance based on a backward correction. Chen et al. (2008) have proposed their MPFA with an enriched stencil (MPFA-E), in order to mitigate spurious oscillations for the scalar field. Kuzmin, Shashkov and Svyatskiy (2009) presented a nonlinear constrained finite element scheme, in which they perform an algebraic matrix splitting followed by a slope limiting to impose DMP. Other finite volume formulations using two-steps strategies, as those presented by Su, Dong and Wu (2018) and Zhao, Sheng and Yuan (2020), also presents good results in terms of DMP. Finally, Cavalcante et al. (2022) presented a nonlinear defect correction to be applied on the MPFA-D of Lira Filho et al. (2021), but extensible to general MPFA methods, in order to ensure the DMP. Their repairing strategy is based on the fact that the MPFA-D flux expression can be naturally divided into two parts: the TFPA flux portion and the flux portion associated with the cross-diffusion terms (CDT). This flux splitting (EDWARDS, 2000; PAL; EDWARDS, 2006, 2011), in which the linear TPFA portion of the flux provides a solution that is free from spurious oscillations, is followed by local DMP imposition through a non-linear CDT flux limiting, as it is the potential source of the spurious oscillations in the scalar field. The MPFA-D with a non-linear defect correction (MPFA-DNL) aims to limit the CDT flux in order to obtain solutions that comply with the DMP, and that are locally conservative and capable of reproducing piecewise linear solutions exactly.

1.4 OBJECTIVES AND CONTRIBUTIONS OF THIS WORK

The major objective of this work is to develop a computational tool to simulate immiscible two-phase flow in naturally fractured porous media, using a projection-based embedded discrete fracture model (pEDFM) and unstructured tetrahedral meshes, considering effects of gravity and compressibility.

In this context, the specifics objectives are:

- Develop a MPFA-D formulation for unstructured tetrahedral meshes, to discretize the matrix-matrix flux terms.
- Investigate interpolation strategies do be applied on MPFA-D.
- Develop an adaptation of pEDFM to handle the fractures on tetrahedral meshes, to discretize the matrix-fracture and the fracture-fracture flux terms and to modify the matrix-matrix flux terms.
- Test the new numerical strategies presented through the solution of classical problems from the literature or elaborated by the author, in order to verify the accuracy or even the functionality of these proposed techniques.

The main contributions of this work are the presentation of a locally conservative numerical method capable of handling with full tensors and unstructured tetrahedral grids in context of diffusion problems in 3-D (MPFA-D), including a non-linear defect correction for it (MPFA-DNL), to be used in case of DMP violation; the application of this MPFA-D in context of a fully implicit scheme, in order to compose the numerical strategy used to simulate two-phase flow in 3-D; and the presentation of a non-conforming mesh fracture model (pEDFM) to be applied on unstructured tetrahedral grids, enabling a highly flexible simulator of fluid flow in fractured reservoirs, not only in terms of anisotropy (due to MPFA-D), but also in terms of geometry and mesh generation.

1.5 TEXT ORGANIZATION

The next chapters of this text are organized as following: the chapter 2 presents the mathematical modelling of the immiscible two-phase flow in porous media, including the possibility of presence of fractures; the chapter 3 shows the development of the MPFA-D for tetrahedral meshes and of the MPFA-DNL; the chapter 4 presents fracture modelling strategies, shortly passing by some classical methods and presenting the

pEDFM, used here in this work; the chapter 5 shows the applications of the proposed numerical formulations and of the computational simulation tool composed by them and the chapter 6 presents the conclusions of this researching work.

2 MATHEMATICAL MODEL

This chapter presents the mathematical model used here to describe the fluid flows in a porous reservoir rock, starting with some simplifying assumptions, followed by some fundamental concepts about rock and fluid properties which are important to the comprehension of the mathematical model, followed by the governing equations, including the auxiliary conditions.

2.1 ASSUMPTIONS

Fluid flows in porous media is a very complex phenomenon, which would lead to a complex mathematical model, so, aiming to simplify it, the following assumptions were considered:

A1. Immiscible two-phase flow of oil (o) and water (w).

A2. The rock (porous media) is fully saturated by fluids.

A3. Rock and fractures are not deformable.

A4. Thermal, chemical and capillary effects, as well as the dispersion and adsorption effects, are all neglected.

A5. The Darcy's law is applicable.

2.2 ROCK AND FLUID PROPERTIES

For the study of fluid flows in porous media, as in oil reservoirs, an important property is the ratio of pore volume (available to be occupied by the fluid) to the total volume of the medium (V_R^T). This ratio is called porosity (ϕ). In a reservoir rock, there are some isolated pores, while others are interconnected, then two types of porosity can be calculated, the total porosity, which considers all the pores of the rock sample, and the effective porosity, which account only volume of the interconnected ones (V_R) (ERTEKIN; ABOU-KASSEM; KING, 2001). In the remainder of this text, the term porosity is used to refer to the effective porosity, because it indicates, the capacity of the reservoir to accumulate fluids that can be displaced (exploitable fluids), then:

$$\phi = \frac{V_R}{V_R^T} \tag{2.1}$$

Since the rock here is considered to be not deformable, the value of ϕ is constant. Considering that there are several fluid phases within the porous media, the saturation of a phase α (S_α) is the ratio of the volume occupied by this phase (V_α) to the total pore volume:

$$S_\alpha = \frac{V_\alpha}{V_R} \tag{2.2}$$

Considering a fully saturated porous media we can write:

$$\sum_\alpha S_\alpha = 1 \tag{2.3}$$

As referred above (see assumption A1), the scope of this work is the study of oil (o) and water (w) immiscible two-phase flow, then the Eq. (2.3) becomes:

$$S_w + S_o = 1 \tag{2.4}$$

Other important property to define is permeability, which is the capacity of a porous medium to transmit fluids through its interconnected pores. If the porous medium is completely saturated by only one phase, this capacity is called absolute permeability (**K**), referred from now just as permeability. A rock sample, however, is not necessarily equally permeable in all directions, i.e., it is a potentially anisotropic medium. That is why the permeability is generally described as a tensor, which can be represented by a symmetric matrix. Using Cartesian coordinates in 3-D, the permeability tensor would be:

$$\mathbf{K}(\vec{x}) = \begin{bmatrix} \mathrm{K}_{xx} & \mathrm{K}_{xy} & \mathrm{K}_{xz} \\ \mathrm{K}_{xy} & \mathrm{K}_{yy} & \mathrm{K}_{yz} \\ \mathrm{K}_{xz} & \mathrm{K}_{yz} & \mathrm{K}_{zz} \end{bmatrix} \tag{2.5}$$

where $\vec{x}$ is the position vector.

If there are more than one phase filling the porous media, it is necessary to consider the mobility of a phase α (λ_α) in the presence of other phases, which is calculated as (FANCHI, 2006):

$$\lambda_\alpha = \frac{k_{r\alpha}}{\mu_\alpha} \tag{2.6}$$

in which $k_{r\alpha}$ is the relative permeability of the phase α, which can be defined, for oil and water, as (COREY, 1954; ISLAM, 2015):

$$k_{rw} = (S_n)^{n_w};\ k_{ro} = (1 - S_n)^{n_o}; \tag{2.7}$$

in which n_w and n_o are parameters that can assume different values (KOZDON; MALLISON; GERRITSEN, 2011), but, in this work, they are $n_w = n_o = 1$. Besides, S_n is the normalization of the water phase saturation with respect to the irreducible water saturation (S_{wi}) and the residual oil saturation (S_{or}), defined as (CHEN; HUAN; MA, 2006; ISLAM, 2015):

$$S_n = \frac{S_w - S_{wi}}{1 - S_{wi} - S_{or}} \tag{2.8}$$

in which S_{wi} is defined as the water saturation that would remain after a complete drainage process, i.e., the S_w bellow which the water could not be displaced anymore due to the rock-fluid interactions. In the same way, S_{or} is the minimum remainder oil saturation after a complete imbibition processes (ERTEKIN; ABOU-KASSEM; KING, 2001).

Besides, μ_α is the viscosity of the phase α, i.e., the measure of the resistance of the fluid to the flow. This property relates the shear stress applied to a fluid and the gradient of the velocity acquired by it as result of the load (FOX; PRITCHARD; MCDONALD, 2010).

Considering the fluid phases as continuous medium, in which any property of it can be defined in any point, if m_α and V_α are, respectively, the mass and the volume of a phase α, the specific mass (or density, ρ_α) of it is defined as (FOX; PRITCHARD; MCDONALD, 2010):

$$\rho_\alpha = \lim_{\delta V_\alpha \to V_\alpha^r} \frac{\delta m_\alpha}{\delta V_\alpha} \tag{2.9}$$

where V_α^r is the representative elementary volume above which the density becomes stable, i.e., an average defined value can be deterministically determined. However, if the fluid phase is compressible, its density also may vary as function of pressure. In this context, we define the phase compressibility as:

$$c_{f\alpha} = \frac{1}{\rho_\alpha}\frac{\partial \rho_\alpha}{\partial p} \tag{2.10}$$

2.3 GOVERNING EQUATIONS

The equations used to model the immiscible two-phase flow (oil and water) in heterogeneous and anisotropic porous media are presented here. Considering a phase α, the mass conservation law is defined, in a 3-D domain Ω_m (representing the reservoir rock), as following:

$$\frac{\partial}{\partial t}(\phi \rho_\alpha S_\alpha) + \nabla \cdot (\rho_\alpha \vec{v}_\alpha) = \rho_\alpha q_\alpha \tag{2.11}$$

in which $\vec{v}_\alpha$ is the phase velocity and q_α is the source or sink term of the phase. The fluid flow also obeys the Darcy's law (see assumption A5) which is an empirical law proposed by Henry Darcy to describe the displacement of a fluid through a porous media (DARCY, 1856). Despite being an empiric law, later studies led to a general form of the Darcy's law for the laminar flow of a phase α in presence of other phases (BEAR, 1972; PEACEMAN, 1977; EWING, 1983), which is largely used in reservoir simulation and is defined as following:

$$\vec{v}_\alpha = -\lambda_\alpha \mathbf{K}(\nabla p_\alpha - \rho_\alpha \vec{g}) \tag{2.12}$$

in which $\vec{g} = g\,\nabla z$ with g being the gravity acceleration modulus and z being the depth of the point where $\vec{v}_\alpha$ is calculated. Beyond this, p_α is the phase pressure, with $\alpha = o, w$. In this work, according to assumption A4, the fluid pressure is $p = p_o = p_w$.

Therefore, the equation describing the flow of a phase α in a porous media is the combination of Eq. (2.11) and Eq. (2.12), that can be summarized as:

$$\frac{\partial}{\partial t}(\phi\rho_\alpha S_\alpha) - \nabla \cdot [\rho_\alpha \lambda_\alpha \mathbf{K}(\nabla p_\alpha - \rho_\alpha \vec{g})] = \rho_\alpha q_\alpha \tag{2.13}$$

Thus, Eq. (2.13) written for both phases (oil and water) together with Eq. (2.4) and with the adequate initial and boundary conditions (still to be presented) compose the mathematical model for the phenomenon of interest. It is a coupled scheme (ERTEKIN; ABOU-KASSEM; KING, 2001; FANCHI, 2006), that is appropriate to the study of compressible flow.

In case of considering incompressible flow, the restriction given in Eq. (2.4) and summing Eq. (2.11) written for both phases (oil and water), we have:

$$\nabla \cdot (\vec{v}_o + \vec{v}_w) = q_o + q_w \tag{2.14}$$

which can be used to find the solution only for pressure in segregate schemes (PEACEMAN, 1977). In this context, the Eq. (2.11) could be used to update the saturation field of the phase α in the following form:

$$\phi \frac{\partial S_\alpha}{\partial t} + \nabla \cdot \vec{v}_\alpha = q_\alpha \tag{2.15}$$

If there are fractures within Ω_m (see Figure 1), it is necessary to consider, in the mathematical model, the phase flux between it and a domain Ω_{f_k} representing the k-th of these 2-D fractures within Ω_m. Thus, the Eq. (2.11) becomes:

$$\frac{\partial}{\partial t}(\phi\rho_\alpha S_\alpha)_m + \nabla \cdot (\rho_\alpha \vec{v}_\alpha)_m = (\rho_\alpha q_\alpha)_m + \sum_{k=1}^{n_{frac}} (\rho_\alpha \varphi_\alpha)_{m,f_k} \tag{2.16}$$

in which n_{frac} is the number of fractures within Ω_m and $(\rho_\alpha \varphi_\alpha)_{m,f_k}$ is the phase flux between Ω_m and Ω_{f_k} defined accordingly to the work of Hajibeygi, Karvounis and Jenny (2011). Similarly, considering a domain Ω_{f_k}, for phase α, we can write:

$$\frac{\partial}{\partial t}(\phi\rho_\alpha S_\alpha)_{f_k} + \nabla\cdot(\rho_\alpha\vec{v}_\alpha)_{f_k} = (\rho_\alpha q_\alpha)_{f_k} + (\rho_\alpha\varphi_\alpha)_{f_k,m} + \sum_{j=1}^{n_{frac}}(\rho_\alpha\varphi_\alpha)_{f_k,f_j;\,k\neq j} \tag{2.17}$$

in which $(\rho_\alpha\varphi_\alpha)_{f_k,m}$ and $(\rho_\alpha\varphi_\alpha)_{f_k,f_j}$ are defined analogously to $(\rho_\alpha\varphi_\alpha)_{m,f_k}$.

2.4 INITIAL AND BOUNDARY CONDITIONS

In order to obtain a complete description of the problem, it is necessary to define appropriate auxiliary initial and boundary conditions. In this case, considering Ω_m, its contour Γ_m is defined as:

$$\Gamma_m = \Gamma_m^D \cup \Gamma_m^N \cup \Gamma_m^P \cup \Gamma_m^I \tag{2.18}$$

where Γ_m^D and Γ_m^N represent the boundaries with prescribed pressures (Dirichlet boundary conditions), and prescribed fluxes (Neumann boundary conditions), respectively, and Γ_m^P and Γ_m^I represent the production and injection wells, respectively. Therefore, these auxiliary conditions are typically given by (AZIZ; SETTARE, 1979; CONTRERAS et al., 2016):

$$\begin{array}{ccc} p(\vec{x},t) = g_D & on & \Gamma_m^D\times[0,t] \\ \vec{v}\cdot\vec{n} = g_N & on & \Gamma_m^N\times[0,t] \\ S_w(\vec{x},t) = \bar{S}_w & on & \Gamma_m^I\times[0,t] \\ S_w(\vec{x},0) = \bar{S}_w^0 & on & \Omega_m \end{array} \tag{2.19}$$

where t is the time variable, g_D is a prescribed scalar function for pressure and g_N is a prescribed scalar function for flux. Moreover, $\vec{n}$ is the outward unitary normal vector to the control surface, $\vec{v} = \vec{v}_w + \vec{v}_o$ is the total flow velocity, $\bar{S}_w$ is the prescribed water saturation on injection well and $\bar{S}_w^0$ is the initial water saturation distribution throughout the reservoir. Besides, pressure or flux can be prescribed in the wells as:

$$\begin{aligned} p(\vec{x},t) &= g_{\mathcal{W},1} \quad on \quad \Gamma_m^{\mathcal{W}} \times [0,t] \\ \int_{\Gamma_{\mathcal{W}}} \vec{v}\cdot\vec{n}\,\partial\Gamma_{\mathcal{W}} &= g_{\mathcal{W},2} \quad on \quad \Gamma_m^{\mathcal{W}} \times [0,t] \end{aligned} \quad with \quad \mathcal{W} = I,P \tag{2.20}$$

where $g_{\mathcal{W},1}$ and $g_{\mathcal{W},2}$ are prescribed scalar functions for pressure and flux, respectively. In case of Eq. (2.14), the conditions for saturation are not applicable. Moreover, all the fractures are considered to be completely contained in Ω_m, so there are not any boundary conditions pertaining to them. The initial water saturation throughout the fractures follows the same spatial distribution given by $\bar{S}_w^0$.

Figure 1 – 3-D domain containing 2-D fractures.

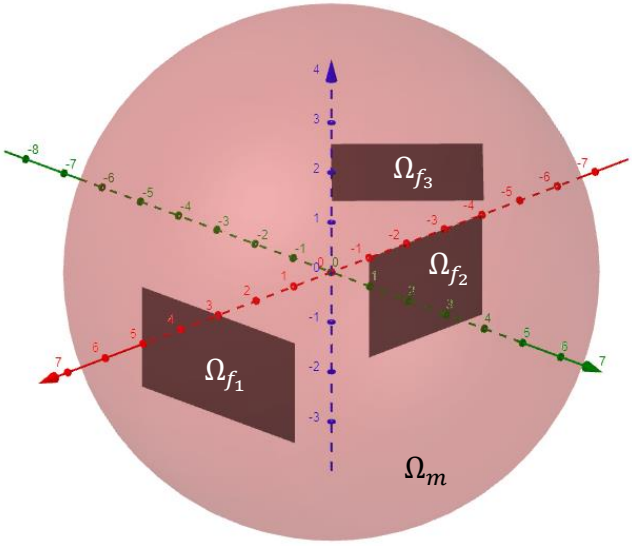

Source: The author (2023).

3 NUMERICAL FORMULATION

It is usually very hard (even impossible) to obtain analytical solutions for the system of equations risen from the mathematical model presented in the previous chapter, this is the reason why it is necessary to use numerical formulations to find the solutions for this type of problems (CHEN; HUAN; MA, 2006). This section presents some numerical strategies used here for this purpose.

3.1 GOVERNING EQUATIONS

In order to obtain the finite volume discretization of Eq. (2.16), it is necessary to integrate it on Ω_m:

$$\int_{\Omega_m} \frac{\partial}{\partial t}(\phi \rho_\alpha S_\alpha)\, \partial\Omega_m + \int_{\Omega_m} \nabla \cdot (\rho_\alpha \vec{v}_\alpha)\, \partial\Omega_m = \int_{\Omega_m} \rho_\alpha q_\alpha\, \partial\Omega_m + \sum_{k=1}^{n_{frac}} \int_{\Omega_m} (\rho_\alpha \varphi_\alpha)_{m,f_k}\, \partial\Omega_m \tag{3.1}$$

Considering that Ω_m is discretized by n_{tetra} tetrahedral control volumes (CV) and that Ω_{f_k} is discretized by n_{polyg}^k polygonal CV, we can rewrite Eq. (3.1) as:

$$\sum_{t=1}^{n_{tetra}} \int_{\Omega_{\hat{t}}} \frac{\partial}{\partial t}(\phi \rho_\alpha S_\alpha)\, \partial\Omega_{\hat{t}} + \sum_{t=1}^{n_{tetra}} \int_{\Omega_{\hat{t}}} \nabla \cdot (\rho_\alpha \vec{v}_\alpha)\, \partial\Omega_{\hat{t}} = \sum_{t=1}^{n_{tetra}} \int_{\Omega_{\hat{t}}} \rho_\alpha q_\alpha\, \partial\Omega_{\hat{t}} + \sum_{t=1}^{n_{tetra}} \sum_{k=1}^{n_{frac}} \sum_{i=1}^{n_{polyg}^k} \int_{\Omega_{\hat{t}}} (\rho_\alpha \varphi_\alpha)_{\hat{t},\check{k}_i}^{\tau+1}\, \partial\Omega_{\hat{t}} \tag{3.2}$$

in which $\hat{t}$ is the t-th tetrahedral CV discretizing Ω_m, $\Omega_{\hat{t}}$ is the volume of $\hat{t}$ and $\check{k}_i$ is the i-th polygonal CV discretizing Ω_{f_k}. Thus, considering just $\hat{t}$, we have:

$$\int_{\Omega_{\hat{t}}} \frac{\partial}{\partial t}(\phi \rho_\alpha S_\alpha)\, \partial\Omega_{\hat{t}} + \int_{\Omega_{\hat{t}}} \nabla \cdot (\rho_\alpha \vec{v}_\alpha)\, \partial\Omega_{\hat{t}} = \int_{\Omega_{\hat{t}}} \rho_\alpha q_\alpha\, \partial\Omega_{\hat{t}} + \sum_{k=1}^{n_{frac}} \sum_{i=1}^{n_{polyg}^k} \int_{\Omega_{\hat{t}}} (\rho_\alpha \varphi_\alpha)_{\hat{t},\check{k}_i}^{\tau+1}\, \partial\Omega_{\hat{t}} \tag{3.3}$$

Discretizing the derivative in the first term of Eq. (3.3) using the backward Euler method, applying the Gauss Divergence Theorem on its second term and considering an implicit scheme (CHEN; HUAN; MA, 2006), we have:

$$\int_{\Omega_{\hat{t}}} \phi \frac{(\rho_\alpha S_\alpha)^{\tau+1} - (\rho_\alpha S_\alpha)^{\tau}}{\Delta t}\, \partial\Omega_{\hat{t}} + \int_{\Gamma_{\hat{t}}} [\rho_\alpha (\vec{v}_\alpha \cdot \vec{n})]^{\tau+1}\, \partial\Gamma_{\hat{t}} = \int_{\Omega_{\hat{t}}} (\rho_\alpha q_\alpha)^{\tau+1}\, \partial\Omega_{\hat{t}} + \sum_{k=1}^{n_{frac}} \sum_{i=1}^{n_{polyg}^k} \int_{\Omega_{\hat{t}}} (\rho_\alpha \varphi_\alpha)_{\hat{t},\check{k}_i}^{\tau+1}\, \partial\Omega_{\hat{t}} \tag{3.4}$$

in which $\Gamma_{\hat{t}}$ is the set of boundary surfaces of $\hat{t}$, τ is the time step index and $\vec{n}$ is the outward normal vector of $\Gamma_{\hat{t}}$. Applying the mean value theorem on the first integral term on the left-hand side and on the first integral term in right-hand side, we have:

$$\phi_{\hat{t}} \Omega_{\hat{t}} \frac{(\rho_\alpha S_\alpha)_{\hat{t}}^{\tau+1} - (\rho_\alpha S_\alpha)_{\hat{t}}^{\tau}}{\Delta t} + \int_{\Gamma_{\hat{t}}} [\rho_\alpha (\vec{v}_\alpha \cdot \vec{n})]^{\tau+1}\, \partial\Gamma_{\hat{t}} = \Omega_{\hat{t}} (\rho_\alpha q_\alpha)_{\hat{t}}^{\tau+1} + \sum_{k=1}^{n_{frac}} \sum_{i=1}^{n_{polyg}^k} \int_{\Omega_{\hat{t}}} (\rho_\alpha \varphi_\alpha)_{\hat{t},\check{k}_i}^{\tau+1}\, \partial\Omega_{\hat{t}} \tag{3.5}$$

in which $\phi_{\hat{t}}$, ρ_α, S_α and q_α are taken as the mean value, respectively, of rock porosity and of density, saturation and source term of phase α, at $\Omega_{\hat{t}}$. Following the work of Ţene et al. (2017), we can consider that:

$$\int_{\Omega_{\hat{t}}} (\rho_\alpha \varphi_\alpha)_{\hat{t},\check{k}_i}\, \partial\Omega_{\hat{t}} = (\rho_\alpha q_\alpha)_{\hat{t},\check{k}_i} = -\rho_\alpha \lambda_\alpha \mathfrak{T}_{\hat{t},\check{k}_i} \left(p_{\check{k}_i} - p_{\hat{t}}\right) \tag{3.6}$$

in which $\mathfrak{T}_{\hat{t},\check{k}_i}$ is the transmissibility term between $\hat{t}$ and $\check{k}_i$ to be defined in chapter 4. Moreover, $(\rho_\alpha q_\alpha)_{\hat{t},\check{k}_i}$ is the notation used from now for the flux between $\hat{t}$ and $\check{k}_i$ integrated on $\Omega_{\hat{t}}$. Then, we have:

$$\begin{aligned}\phi_{\hat{t}}\Omega_{\hat{t}}\frac{(\rho_\alpha S_\alpha)_{\hat{t}}^{\tau+1}-(\rho_\alpha S_\alpha)_{\hat{t}}^{\tau}}{\Delta t}+\int_{\Gamma_{\hat{t}}}[\rho_\alpha(\vec{v}_\alpha\cdot\vec{n})]^{\tau+1}\,\partial\Gamma_{\hat{t}}\\ =\Omega_{\hat{t}}(\rho_\alpha q_\alpha)_{\hat{t}}^{\tau+1}+\sum_{k=1}^{n_{frac}}\sum_{i=1}^{n_{polyg}^{k}}(\rho_\alpha q_\alpha)_{\hat{t},\check{k}_i}^{\tau+1}\end{aligned} \tag{3.7}$$

Performing the same development from Eq. (2.17) and considering that $\int_{\Omega_{\hat{t}}}(\rho_\alpha\varphi_\alpha)_{\hat{t},\check{k}_i}\,\partial\Omega_{\hat{t}}=-\int_{\Omega_{\check{k}_i}}(\rho_\alpha\varphi_\alpha)_{\check{k}_i,\hat{t}}\,\partial\Omega_{\check{k}_i}$ (HOSSEINIMEHR et al., 2022), in which $\Omega_{\check{k}_i}$ is the area of the polygon $\check{k}_i$, we can also write a similar expression for $\check{k}_i$:

$$\begin{aligned}\phi_{\check{k}_i}\Omega_{\check{k}_i}\frac{(\rho_\alpha S_\alpha)_{\check{k}_i}^{\tau+1}-(\rho_\alpha S_\alpha)_{\check{k}_i}^{\tau}}{\Delta t}+\int_{\Gamma_{\check{k}_i}}[\rho_\alpha(\vec{v}_\alpha\cdot\vec{n})]^{\tau+1}\,\partial\Gamma_{\check{k}_i}\\ =\Omega_{i_j}(\rho_\alpha q_\alpha)_{\check{k}_i}^{\tau+1}-\sum_{t=1}^{n_{tetra}}(\rho_\alpha q_\alpha)_{\hat{t},\check{k}_i}^{\tau+1}+\sum_{h=1}^{n_{frac}}\sum_{y=1}^{n_{polyg}^{h}}(\rho_\alpha q_\alpha)_{\check{k}_i,\check{h}_y;\,k\neq h}^{\tau+1}\end{aligned} \tag{3.8}$$

in which $(\rho_\alpha q_\alpha)_{\check{k}_i,\check{h}_y}$ is defined analogously to $(\rho_\alpha q_\alpha)_{\hat{t},\check{k}_i}$ (see chapter 4). Remembering that $\hat{t}$ is a tetrahedral cell and that $\check{k}_i$ is a polygonal cell, and using again the mean value theorem to evaluate the integral terms of Eq. (3.7) and Eq. (3.8) on each face (or edge) of $\hat{t}$ and $\check{k}_i$, these equations can be rewritten as:

$$\begin{aligned}\phi_{\hat{t}}\Omega_{\hat{t}}\frac{(\rho_\alpha S_\alpha)_{\hat{t}}^{\tau+1}-(\rho_\alpha S_\alpha)_{\hat{t}}^{\tau}}{\Delta t}+\sum_{\bar{F}\in\Gamma_{\hat{t}}}\left[\rho_\alpha\left(\vec{v}_\alpha\cdot\vec{N}_{\bar{F}}\right)\right]^{\tau+1}\\ =\Omega_{\hat{t}}(\rho_\alpha q_\alpha)_{\hat{t}}^{\tau+1}+\sum_{k=1}^{n_{frac}}\sum_{i=1}^{n_{polyg}^{k}}(\rho_\alpha q_\alpha)_{\hat{t},\check{k}_i}^{\tau+1}\end{aligned} \tag{3.9}$$

in which $\vec{N}_{\bar{F}}$ is the outward area normal vector of the face $\bar{F}$ and:

$$\phi_{\check{k}_i}\Omega_{\check{k}_i}\frac{(\rho_\alpha S_\alpha)_{\check{k}_i}^{\tau+1}-(\rho_\alpha S_\alpha)_{\check{k}_i}^{\tau}}{\Delta t}+\sum_{\dot{E}\in\Gamma_{\check{k}_i}}\left[\rho_\alpha\left(\vec{v}_\alpha\cdot\vec{N}_{\dot{E}}\right)\right]^{\tau+1}$$
$$=\Omega_{\check{k}_i}(\rho_\alpha q_\alpha)_{\check{k}_i}^{\tau+1}-\sum_{t=1}^{n_{tetra}}(\rho_\alpha q_\alpha)_{\hat{t},\check{k}_i}^{\tau+1} \qquad (3.10)$$
$$+\sum_{h=1}^{n_{frac}}\sum_{y=1}^{n_{polyg}^{h}}(\rho_\alpha q_\alpha)_{\check{k}_i,\check{h}_y;\,k\neq h}^{\tau+1}$$

in which $\vec{N}_{\dot{E}}$ is the length normal vector of the edge $\dot{E}$, outward to $\check{k}_i$. The second term on the left-hand side of Eq. (3.9), referred from now as pressure terms (because of the velocity definition according Darcy's Law), must be determined. The strategy used here with this objective is a finite volume scheme using a multipoint flux approximation with a diamond stencil (MPFA-D), that will be described in section 3.2. In the same way, the second term on the left-hand side of Eq. (3.10) also need to be determined, as well as the second and the third terms on the right-hand side of the same equation, and the second term on the right-hand side of Eq. (3.9).

As mentioned, the Eq. (3.9) and Eq. (3.10) represent an implicit scheme. In this context, aiming to get a stable formulation, we take the value of ρ_α from the CV upwind to the flow (CHEN; HUAN; MA, 2006). Then, in order to get the solution for the numerical scheme, we write Eq. (3.9) and Eq. (3.10) in residual form and obtain:

$$(r_\alpha)_{\hat{t}}^{\tau+1}=\Omega_{\hat{t}}(\rho_\alpha q_\alpha)_{\hat{t}}^{\tau+1}-\phi_{\hat{t}}\Omega_{\hat{t}}\frac{(\rho_\alpha S_\alpha)_{\hat{t}}^{\tau+1}-(\rho_\alpha S_\alpha)_{\hat{t}}^{\tau}}{\Delta t}-\sum_{\bar{F}\in\Gamma_{\hat{t}}}\left[\rho_\alpha\left(\vec{v}_\alpha\cdot\vec{N}_{\bar{F}}\right)\right]^{\tau+1}$$
$$+\sum_{k=1}^{n_{frac}}\sum_{i=1}^{n_{polyg}^{k}}(\rho_\alpha q_\alpha)_{\hat{t},\check{k}_i}^{\tau+1} \qquad (3.11)$$

and:

$$(r_\alpha)_{\check{k}_i}^{\tau+1} = \Omega_{\check{k}_i}(\rho_\alpha q_\alpha)_{\check{k}_i}^{\tau+1} - \phi_{\check{k}_i}\Omega_{\check{k}_i}\frac{(\rho_\alpha S_\alpha)_{\check{k}_i}^{\tau+1} - (\rho_\alpha S_\alpha)_{\check{k}_i}^{\tau}}{\Delta t} - \sum_{\dot{E}\in\Gamma_{\check{k}_i}}\left[\rho_\alpha(\vec{v}_\alpha\cdot\vec{N}_{\dot{E}})\right]^{\tau+1} - \sum_{t=1}^{n_{tetra}}(\rho_\alpha q_\alpha)_{\hat{t},\check{k}_i}^{\tau+1} + \sum_{h=1}^{n_{frac}}\sum_{y=1}^{n_{polyg}^{h}}(\rho_\alpha q_\alpha)_{\check{k}_i,\check{h}_{y;\,k\neq h}}^{\tau+1} \tag{3.12}$$

This way, writing the Eq. (3.11) and Eq. (3.12) for each CV ($\hat{t}$ and $\check{k}_i$) of the computational mesh at each time step (τ), we get a non-linear system of equations that can be linearized and solved by the Newton-Raphson (NR) method (CHEN; HUAN; MA, 2006). Therefore, for each NR iteration (υ) we can write:

$$r_\alpha^{\upsilon+1} \approx r_\alpha^{\upsilon} + \left(\frac{\partial r_\alpha}{\partial p}\right)^{\upsilon}\delta p^{\upsilon+1} + \left(\frac{\partial r_\alpha}{\partial S}\right)^{\upsilon}\delta S^{\upsilon+1} \tag{3.13}$$

in which $r_\alpha = [r_{\alpha,m} \quad r_{\alpha,f}]^T$ is the vector of the residuals for each degree of freedom in the domains Ω_m and Ω_{f_k} (with $k = 1$ to n_{frac}) and, similarly, $\delta p = [\delta p_m \quad \delta p_f]^T$ and $\delta S = [\delta S_m \quad \delta S_f]^T$. Therefore, considering both phases (oil and water), we can write:

$$\begin{bmatrix} r_{w,m} \\ r_{w,f} \\ r_{o,m} \\ r_{o,f} \end{bmatrix}^{\upsilon} + \mathcal{J}^{\upsilon}\begin{bmatrix} \delta p_m \\ \delta p_f \\ \delta S_m \\ \delta S_f \end{bmatrix}^{\upsilon+1} = 0 \rightarrow \begin{bmatrix} \delta p_m \\ \delta p_f \\ \delta S_m \\ \delta S_f \end{bmatrix}^{\upsilon+1} = -\{\mathcal{J}^{\upsilon}\}^{-1}\begin{bmatrix} r_{w,m} \\ r_{w,f} \\ r_{o,m} \\ r_{o,f} \end{bmatrix}^{\upsilon} \tag{3.14}$$

in which the Jacobian matrix ($\mathcal{J}$) is defined as:

$$\mathcal{J} = \begin{bmatrix} \begin{bmatrix} \mathcal{J}_{wp}^{mm} & \mathcal{J}_{wp}^{mf} \\ \mathcal{J}_{wp}^{fm} & \mathcal{J}_{wp}^{ff} \end{bmatrix} & \begin{bmatrix} \mathcal{J}_{wS}^{mm} & \mathcal{J}_{wS}^{mf} \\ \mathcal{J}_{wS}^{fm} & \mathcal{J}_{wS}^{ff} \end{bmatrix} \\ \begin{bmatrix} \mathcal{J}_{op}^{mm} & \mathcal{J}_{op}^{mf} \\ \mathcal{J}_{op}^{fm} & \mathcal{J}_{op}^{ff} \end{bmatrix} & \begin{bmatrix} \mathcal{J}_{oS}^{mm} & \mathcal{J}_{oS}^{mf} \\ \mathcal{J}_{oS}^{fm} & \mathcal{J}_{oS}^{ff} \end{bmatrix} \end{bmatrix} \tag{3.15}$$

in which:

$$\mathcal{J}_{\alpha p}^{\beta\gamma} = \frac{\partial r_{\alpha,\beta}}{\partial p_{\gamma}} \text{ with } \alpha = w, o \text{ and } \beta, \gamma = m, f \tag{3.16}$$

The convergence criteria for the iterative process is defined as (HOSSEINIMEHR et al., 2022):

$$\left(\frac{\|r_w^{v+1}\|_2}{\|r_w^0\|_2} < \epsilon_w \text{ or } \frac{\|r_w^{v+1}\|_2}{\|RHS_w\|_2} < \epsilon_w\right) \text{and} \left(\frac{\|r_o^{v+1}\|_2}{\|r_o^0\|_2} < \epsilon_o \text{ or } \frac{\|r_o^{v+1}\|_2}{\|RHS_o\|_2} < \epsilon_o\right) \text{and} \left(\frac{\|\delta p\|_2}{\|p\|_2} < \epsilon_p \text{ and } \frac{\|\delta S\|_2}{\|S\|_2} < \epsilon_S\right) \tag{3.17}$$

in which ϵ_w, ϵ_o, ϵ_p and ϵ_S are tolerances defined by the user, and $\|S\|_2$ is the L-2 norm of saturation vector, what is analogous for the other terms. Moreover, all the prescribed terms associated to phase α will comprise its "right-hand side" (RHS_α). In cases in which there are not Dirichlet boundary conditions or Neumann boundary conditions with values different than zero, $RHS_\alpha = \rho_\alpha q_\alpha$.

3.2 PRESSURE TERM DISCRETIZATION FOR TETRAHEDRAL CELLS

In this section we present the development of the MPFA-D expression used to discretize the second terms in Eq. (3.5) and Eq. (3.7), considering a 3-D domain that is discretized using a tetrahedral mesh. The flux expression was developed as stated by Lira Filho et al. (2021), but with different strategies for the interpolation of the vertex unknowns. Besides, in this section we also present a non-linear defect correction strategy that was developed to avoid problems with DMP violation that can happen when using linear MPFA formulations, particularly for applications involving highly distorted meshes and strongly anisotropic permeability tensors.

3.2.1 Finite volume discretization

Consider a tetrahedral control volume $\hat{L}$, formed by vertices I, J, K and Q (see Figure 2), to be a primary cell of the tetrahedral mesh used to discretize a domain Ω. $\vec{S}_I^{\hat{L}}$ (see Figure 2) is the outward normal area vector of the opposite face to the vertex I in the tetrahedron $\hat{L}$ (analogously for the other vertices). Considering the second term on the left-hand side of Eq. (3.5), we have:

$$\int_{\Gamma_{\hat{L}}} \rho_\alpha(\vec{v}_\alpha \cdot \vec{n})\, \partial\Gamma_{\hat{L}} = \sum_{I \in \hat{L}} \rho_\alpha\left(\vec{v}_\alpha \cdot \vec{S}_I^{\hat{L}}\right) \tag{3.18}$$

The flux expression $\vec{v}_\alpha \cdot \vec{S}_I^{\hat{L}}$ is what we need to determine to define our formulation.

3.2.2 Gradient expression under the linearity-preserving criterion

Applying the Gauss's Divergence Theorem to this tetrahedron and considering a scalar field u, we have (ARFKEN; WEBER; HARRIS, 2013):

$$\int_{\Omega_{\hat{L}}} \nabla u\, \partial\Omega_{\hat{L}} = \int_{\Gamma_{\hat{L}}} u\, \partial\vec{\Gamma}_{\hat{L}} \tag{3.19}$$

Integrating, using the Mean Value Theorem, and considering that $u_{\bar{I}}$ is the mean value of u at $\bar{I}$, the opposite face to the vertex I in this tetrahedron (analogously to the vertices J, K and Q), we can write:

$$\nabla u = \frac{1}{\Omega_{\hat{L}}}\left(u_{\bar{I}}\vec{S}_I^{\hat{L}} + u_{\bar{J}}\vec{S}_J^{\hat{L}} + u_{\bar{K}}\vec{S}_K^{\hat{L}} + u_{\bar{Q}}\vec{S}_Q^{\hat{L}}\right) \tag{3.20}$$

Using Taylor expansion for multivariable functions (DUISTERMAAT; KOLK, 2010) to find a second order approximation for $u_{\bar{I}}$, $u_{\bar{J}}$, $u_{\bar{K}}$ and $u_{\bar{Q}}$ over the control surfaces of the tetrahedral control volume, we can write:

$$\begin{aligned}\nabla u = \frac{1}{\Omega_{\hat{L}}}\Bigg[&\left(\frac{u_J + u_K + u_Q}{3}\right)\vec{S}_I^{\hat{L}} + \left(\frac{u_I + u_K + u_Q}{3}\right)\vec{S}_J^{\hat{L}} + \left(\frac{u_I + u_J + u_Q}{3}\right)\vec{S}_K^{\hat{L}} \\ &+ \left(\frac{u_I + u_J + u_K}{3}\right)\vec{S}_Q^{\hat{L}}\Bigg]\end{aligned} \tag{3.21}$$

However, Eq. (3.21) can be rearranged, as:

$$\nabla u = \frac{1}{3\Omega_{\hat{L}}}\left[\left(\vec{S}_I^{\hat{L}} + \vec{S}_J^{\hat{L}} + \vec{S}_K^{\hat{L}}\right)u_Q + \left(\vec{S}_I^{\hat{L}} + \vec{S}_J^{\hat{L}} + \vec{S}_Q^{\hat{L}}\right)u_K + \left(\vec{S}_I^{\hat{L}} + \vec{S}_Q^{\hat{L}} + \vec{S}_K^{\hat{L}}\right)u_J + \left(\vec{S}_Q^{\hat{L}} + \vec{S}_J^{\hat{L}} + \vec{S}_K^{\hat{L}}\right)u_I\right] \tag{3.22}$$

But, for the considered tetrahedron, the following identity holds:

$$\vec{S}_I^{\hat{L}} + \vec{S}_J^{\hat{L}} + \vec{S}_K^{\hat{L}} + \vec{S}_Q^{\hat{L}} = 0 \tag{3.23}$$

Therefore, we can write the expression for the mean value of the gradient within a tetrahedral control volume, as:

$$\nabla u = -\frac{1}{3\Omega_{\hat{L}}}\left(u_I\vec{S}_I^{\hat{L}} + u_J\vec{S}_J^{\hat{L}} + u_K\vec{S}_K^{\hat{L}} + u_Q\vec{S}_Q^{\hat{L}}\right) \tag{3.24}$$

3.2.3 MPFA-D inner face unique flux expression for a 3-D tetrahedral mesh

Consider the configuration shown in Figure 3, with two tetrahedrons ($\hat{L}$ and $\hat{R}$) in a 3-D mesh sharing the face $\bar{F} = IJK$. Additionally, consider the auxiliary tetrahedra $\hat{\mathcal{L}}$ and $\hat{\mathcal{R}}$ (also shown in Figure 3). Then, writing the scalar variable gradient expression, as shown in Eq. (3.24), to the tetrahedron $\hat{\mathcal{L}} = \hat{L}IJK$, we have:

$$\nabla u = -\frac{1}{3\Omega_{\hat{\mathcal{L}}}}\left(u_I\vec{S}_I^{\hat{\mathcal{L}}} + u_J\vec{S}_J^{\hat{\mathcal{L}}} + u_K\vec{S}_K^{\hat{\mathcal{L}}} + u_{\hat{L}}\vec{S}_{\hat{L}}^{\hat{\mathcal{L}}}\right) \tag{3.25}$$

The expression in Eq. (3.25) can be replaced Eq. (2.12), but first it is convenient to rewrite this last equation as:

$$\vec{v}_\alpha = \vec{v}_\alpha^{\,p} + \vec{v}_\alpha^{\,g} \tag{3.26}$$

in which $\vec{v}_\alpha^{\,p} = -\lambda_\alpha \mathbf{K}\nabla p$ (pressure term) and $\vec{v}_\alpha^{\,g} = \lambda_\alpha \rho_\alpha \not{g}\mathbf{K}\nabla z$ (gravitational term), according to Eq. (2.12). All the following development presented for $\vec{v}_\alpha^{\,p}$ is analogous for $\vec{v}_\alpha^{\,g}$. Thus, $\vec{v}_\alpha^{\,p}$ can be written for the tetrahedron $\hat{\mathcal{L}}$, based in Eq. (3.25) and considering that pressure (p) is the scalar variable we are looking at, as:

$$\vec{v}_{\alpha}^{p} = \frac{\lambda_{\alpha}}{3\Omega_{\hat{\mathcal{L}}}} \mathbf{K}_{\hat{L}} \left[\left(p_I \vec{S}_I^{\hat{\mathcal{L}}} + p_J \vec{S}_J^{\hat{\mathcal{L}}} + p_K \vec{S}_K^{\hat{\mathcal{L}}} + p_{\hat{L}} \vec{S}_{\hat{L}}^{\hat{\mathcal{L}}} \right) \right] \tag{3.27}$$

where $\mathbf{K}_{\hat{L}}$ is the permeability (diffusion) tensor associated to the tetrahedron $\hat{L}$ (note that $\hat{\mathcal{L}} \subset \hat{L}$). Note that λ_{α} (and ρ_{α} in case of $\vec{v}_{\alpha}^{g}$) are evaluated on the face $\bar{F}$ shared by $\hat{L}$ and $\hat{R}$. Then, the expression corresponding to the flux through the face $\bar{F}$, to be applied in Eq. (3.18), is:

$$\vec{v}_{\alpha}^{p} \cdot \vec{S}_{\hat{L}}^{\hat{\mathcal{L}}} = \frac{\lambda_{\alpha}^{\bar{F}}}{3\Omega_{\hat{\mathcal{L}}}} \mathbf{K}_{\hat{L}} \left(p_I \vec{S}_I^{\hat{\mathcal{L}}} + p_J \vec{S}_J^{\hat{\mathcal{L}}} + p_K \vec{S}_K^{\hat{\mathcal{L}}} + p_{\hat{L}} \vec{S}_{\hat{L}}^{\hat{\mathcal{L}}} \right) \cdot \vec{S}_{\hat{L}}^{\hat{\mathcal{L}}} \tag{3.28}$$

Figure 2 – Tetrahedral control volume $\hat{L}$.

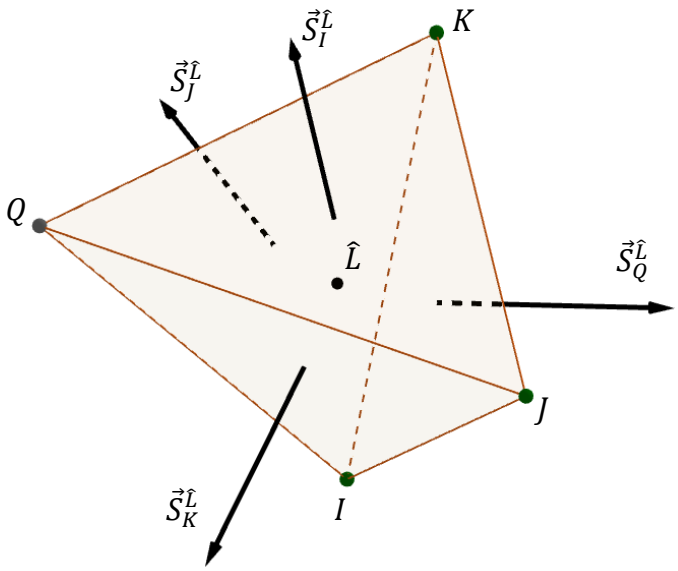

Source: The author (2023).

In the same way, the flux trough that same face, with respect to the tetrahedron $\hat{\mathcal{R}} = IJK\hat{R}$ (see Figure 3) is:

$$\vec{v}_{\alpha}^{p} \cdot \vec{S}_{\hat{R}}^{\hat{\mathcal{R}}} = \frac{\lambda_{\alpha}^{\bar{F}}}{3\Omega_{\hat{\mathcal{R}}}} \mathbf{K}_{\hat{R}} \left(p_I \vec{S}_I^{\hat{\mathcal{R}}} + p_J \vec{S}_J^{\hat{\mathcal{R}}} + p_K \vec{S}_K^{\hat{\mathcal{R}}} + p_{\hat{R}} \vec{S}_{\hat{R}}^{\hat{\mathcal{R}}} \right) \cdot \vec{S}_{\hat{R}}^{\hat{\mathcal{R}}} \tag{3.29}$$

Defining:

$$\vec{N}_{\bar{F}} = \vec{S}_{\hat{L}}^{\hat{\mathcal{L}}} = -\vec{S}_{\hat{R}}^{\hat{\mathcal{R}}} = \left(\overrightarrow{JI} \times \overrightarrow{JK}\right)/2 \tag{3.30}$$

and then, according to Eq. (3.23), we have:

$$\begin{cases} \vec{S}_J^{\hat{\mathcal{L}}} = -\vec{N}_{\bar{F}} - \vec{S}_I^{\hat{\mathcal{L}}} - \vec{S}_K^{\hat{\mathcal{L}}} \\ \vec{S}_J^{\hat{\mathcal{R}}} = \vec{N}_{\bar{F}} - \vec{S}_I^{\hat{\mathcal{R}}} - \vec{S}_K^{\hat{\mathcal{R}}} \end{cases} \tag{3.31}$$

Figure 3 – Face IJK shared by the tetrahedrons $\hat{L}$ and $\hat{R}$, highlighting $\hat{\mathcal{L}}$ and $\hat{\mathcal{R}}$.

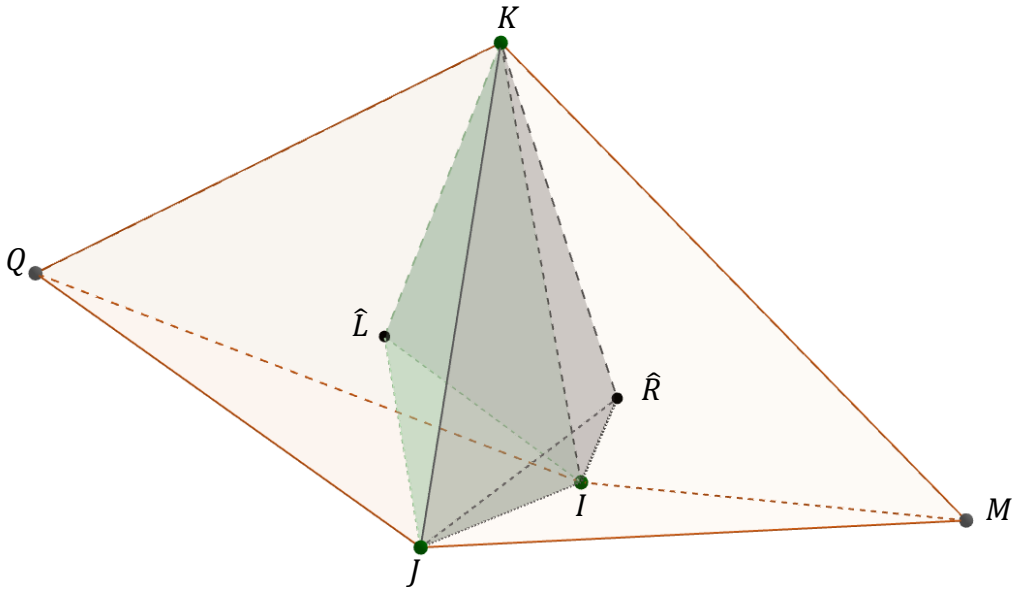

Source: The author (2023).

Then, substituting Eq. (3.31) in Eqs. (3.28) and (3.29), we obtain:

$$\vec{v}_\alpha^{\,p} \cdot \vec{S}_{\hat{L}}^{\hat{\mathcal{L}}} = \frac{\lambda_\alpha^{\bar{F}}}{3\Omega_{\hat{\mathcal{L}}}} \mathbf{K}_{\hat{L}} \left[\vec{S}_I^{\hat{\mathcal{L}}}(p_I - p_J) - \vec{N}_{\bar{F}}(p_J - p_{\hat{L}}) + \vec{S}_K^{\hat{\mathcal{L}}}(p_K - p_J)\right] \cdot \vec{N}_{\bar{F}} \tag{3.32}$$

and:

$$\vec{v}_\alpha^{\,p} \cdot \vec{S}_{\hat{R}}^{\hat{\mathcal{R}}} = -\frac{\lambda_\alpha^{\bar{F}}}{3\Omega_{\hat{\mathcal{R}}}} \mathbf{K}_{\hat{R}} \left[\vec{S}_I^{\hat{\mathcal{R}}}(p_I - p_J) + \vec{N}_{\bar{F}}(p_J - p_{\hat{R}}) + \vec{S}_K^{\hat{\mathcal{R}}}(p_K - p_J)\right] \cdot \vec{N}_{\bar{F}} \tag{3.33}$$

but:

$$\vec{S}_I^{\hat{L}} = \frac{\overrightarrow{JK} \times \overrightarrow{J\hat{L}}}{2};\ \vec{S}_K^{\hat{L}} = \frac{\overrightarrow{J\hat{L}} \times \overrightarrow{JI}}{2};\ \vec{S}_I^{\hat{R}} = \frac{\overrightarrow{J\hat{R}} \times \overrightarrow{JK}}{2};\ \vec{S}_K^{\hat{R}} = \frac{\overrightarrow{JI} \times \overrightarrow{J\hat{R}}}{2} \tag{3.34}$$

then, substituting the expressions of Eq. (3.34) in Eqs. (3.32) and (3.33), and after some algebraic manipulation, we have:

$$\begin{aligned} \vec{v}_\alpha^p \cdot \vec{S}_{\hat{L}}^{\hat{L}} = \frac{\lambda_\alpha^{\bar{F}}}{6\Omega_{\hat{L}}} \mathbf{K}_{\hat{L}} \Big[\left(\overrightarrow{J\hat{L}} \times \overrightarrow{JK}\right)(p_J - p_I) - 2\vec{N}(p_J - p_{\hat{L}}) \\ + \left(\overrightarrow{J\hat{L}} \times \overrightarrow{JI}\right)(p_K - p_J) \Big] \cdot \vec{N}_{\bar{F}} \end{aligned} \tag{3.35}$$

and:

$$\begin{aligned} \vec{v}_\alpha^p \cdot \vec{S}_{\hat{R}}^{\hat{R}} = \frac{\lambda_\alpha^{\bar{F}}}{6\Omega_{\hat{R}}} \mathbf{K}_{\hat{R}} \Big[\left(\overrightarrow{J\hat{R}} \times \overrightarrow{JK}\right)(p_J - p_I) + 2\vec{N}(p_{\hat{R}} - p_J) \\ + \left(\overrightarrow{J\hat{R}} \times \overrightarrow{JI}\right)(p_K - p_J) \Big] \cdot \vec{N}_{\bar{F}} \end{aligned} \tag{3.36}$$

But based on the quadruple product identity (WILLARD GIBBS; BIDWELL WILSON, 1901), using non coplanar basis and considering the already shown notation, we can write the following identities:

$$\begin{cases} \overrightarrow{J\hat{L}} = \dfrac{\langle -\vec{\tau}_{\bar{F}}^{JK}, \overrightarrow{J\hat{L}} \rangle}{2\left|\vec{N}_{\bar{F}}\right|^2} \overrightarrow{JI} + \dfrac{\langle \vec{\tau}_{\bar{F}}^{JI}, \overrightarrow{J\hat{L}} \rangle}{2\left|\vec{N}_{\bar{F}}\right|^2} \overrightarrow{JK} - \dfrac{h_{\hat{L}}^{\bar{F}}}{\left|\vec{N}_{\bar{F}}\right|} \vec{N}_{\bar{F}} \\ \overrightarrow{J\hat{R}} = \dfrac{\langle -\vec{\tau}_{\bar{F}}^{JK}, \overrightarrow{J\hat{R}} \rangle}{2\left|\vec{N}_{\bar{F}}\right|^2} \overrightarrow{JI} + \dfrac{\langle \vec{\tau}_{\bar{F}}^{JI}, \overrightarrow{J\hat{R}} \rangle}{2\left|\vec{N}_{\bar{F}}\right|^2} \overrightarrow{JK} + \dfrac{h_{\hat{R}}^{\bar{F}}}{\left|\vec{N}_{\bar{F}}\right|} \vec{N}_{\bar{F}} \end{cases} \tag{3.37}$$

where $\vec{\tau}_{\bar{F}}^{JK} = \vec{N}_{\bar{F}} \times \overrightarrow{JK}$ and $\vec{\tau}_{\bar{F}}^{JI} = \vec{N}_{\bar{F}} \times \overrightarrow{JI}$. Moreover, $h_{\hat{L}}^{\bar{F}}$ is the distance (height) between the centroid of $\hat{L}$ and the face $\bar{F}$ (analogously to $\hat{R}$). Then, substituting the expressions of Eq. (3.37) in Eqs. (3.35) and (3.36), we have:

$$\vec{v}_\alpha^{\,p}\cdot\vec{S}_{\hat{L}}^{\hat{\mathcal{L}}}=\frac{\lambda_\alpha^{\bar{F}}}{6\Omega_{\hat{\mathcal{L}}}}\mathbf{K}_{\hat{L}}\left[\left(\frac{\langle-\vec{\tau}_{\bar{F}}^{JK},\overrightarrow{J\hat{L}}\rangle}{2\left|\vec{N}_{\bar{F}}\right|^2}2\vec{N}_{\bar{F}}-\frac{h_{\hat{L}}^{\bar{F}}}{\left|\vec{N}_{\bar{F}}\right|}\vec{\tau}_{\bar{F}}^{JK}\right)(p_J-p_I)-2\vec{N}_{\bar{F}}(p_J-p_{\hat{L}})\right.$$
$$\left.+\left(-\frac{\langle\vec{\tau}_{\bar{F}}^{JI},\overrightarrow{J\hat{L}}\rangle}{2\left|\vec{N}_{\bar{F}}\right|^2}2\vec{N}_{\bar{F}}-\frac{h_{\hat{L}}^{\bar{F}}}{\left|\vec{N}_{\bar{F}}\right|}\vec{\tau}_{\bar{F}}^{JI}\right)(p_K-p_J)\right]\cdot\vec{N}_{\bar{F}} \tag{3.38}$$

and:

$$\vec{v}_\alpha^{\,p}\cdot\vec{S}_{\hat{R}}^{\hat{\mathcal{R}}}=\frac{\lambda_\alpha^{\bar{F}}}{6\Omega_{\hat{\mathcal{R}}}}\mathbf{K}_{\hat{R}}\left[\left(\frac{\langle-\vec{\tau}_{\bar{F}}^{JK},\overrightarrow{J\hat{R}}\rangle}{2\left|\vec{N}_{\bar{F}}\right|^2}2\vec{N}_{\bar{F}}+\frac{h_{\hat{R}}^{\bar{F}}}{\left|\vec{N}_{\bar{F}}\right|}\vec{\tau}_{\bar{F}}^{JK}\right)(p_J-p_I)+2\vec{N}_{\bar{F}}(p_{\hat{R}}-p_J)\right.$$
$$\left.+\left(-\frac{\langle\vec{\tau}_{\bar{F}}^{JI},\overrightarrow{J\hat{R}}\rangle}{2\left|\vec{N}_{\bar{F}}\right|^2}2\vec{N}_{\bar{F}}+\frac{h_{\hat{R}}^{\bar{F}}}{\left|\vec{N}_{\bar{F}}\right|}\vec{\tau}_{\bar{F}}^{JI}\right)(p_K-p_J)\right]\cdot\vec{N}_{\bar{F}} \tag{3.39}$$

Manipulating these expressions, we obtain:

$$\vec{v}_\alpha^{\,p}\cdot\vec{S}_{\hat{L}}^{\hat{\mathcal{L}}}=\frac{\lambda_\alpha^{\bar{F}}}{6\Omega_{\hat{\mathcal{L}}}}\left[\left(\frac{\langle\vec{\tau}_{\bar{F}}^{JK},\overrightarrow{\hat{L}J}\rangle}{\left|\vec{N}_{\bar{F}}\right|^2}\vec{N}_{\bar{F}}^T\mathbf{K}_{\hat{L}}\vec{N}_{\bar{F}}-\frac{h_{\hat{L}}^{\bar{F}}}{\left|\vec{N}_{\bar{F}}\right|}\vec{N}_{\bar{F}}^T\mathbf{K}_{\hat{L}}\vec{\tau}_{\bar{F}}^{JK}\right)(p_J-p_I)\right.$$
$$-2\vec{N}_{\bar{F}}^T\mathbf{K}_{\hat{L}}\vec{N}_{\bar{F}}(p_J-p_{\hat{L}}) \tag{3.40}$$
$$\left.+\left(\frac{\langle\vec{\tau}_{\bar{F}}^{JI},\overrightarrow{\hat{L}J}\rangle}{\left|\vec{N}_{\bar{F}}\right|^2}\vec{N}_{\bar{F}}^T\mathbf{K}_{\hat{L}}\vec{N}_{\bar{F}}-\frac{h_{\hat{L}}^{\bar{F}}}{\left|\vec{N}_{\bar{F}}\right|}\vec{N}_{\bar{F}}^T\mathbf{K}_{\hat{L}}\vec{\tau}_{\bar{F}}^{JI}\right)(p_K-p_J)\right]$$

and:

$$\vec{v}_\alpha^{\,p}\cdot\vec{S}_{\hat{R}}^{\hat{\mathcal{R}}}=\frac{\lambda_\alpha^{\bar{F}}}{6\Omega_{\hat{\mathcal{R}}}}\left[\left(\frac{\langle\vec{\tau}_{\bar{F}}^{JK},\overrightarrow{J\hat{R}}\rangle}{\left|\vec{N}_{\bar{F}}\right|^2}\vec{N}_{\bar{F}}^T\mathbf{K}_{\hat{R}}\vec{N}_{\bar{F}}-\frac{h_{\hat{R}}^{\bar{F}}}{\left|\vec{N}_{\bar{F}}\right|}\vec{N}_{\bar{F}}^T\mathbf{K}_{\hat{R}}\vec{\tau}_{\bar{F}}^{JK}\right)(p_I-p_J)\right.$$
$$+2\vec{N}_{\bar{F}}^T\mathbf{K}_{\hat{R}}\vec{N}_{\bar{F}}(p_{\hat{R}}-p_J) \tag{3.41}$$
$$\left.+\left(\frac{\langle\vec{\tau}_{\bar{F}}^{JI},\overrightarrow{J\hat{R}}\rangle}{\left|\vec{N}_{\bar{F}}\right|^2}\vec{N}_{\bar{F}}^T\mathbf{K}_{\hat{R}}\vec{N}_{\bar{F}}-\frac{h_{\hat{R}}^{\bar{F}}}{\left|\vec{N}_{\bar{F}}\right|}\vec{N}_{\bar{F}}^T\mathbf{K}_{\hat{R}}\vec{\tau}_{\bar{F}}^{JI}\right)(p_J-p_K)\right]$$

Finally, we can simplify these expressions as:

$$\vec{v}_\alpha^{\,p}\cdot\vec{S}_{\hat{L}}^{\hat{\mathcal{L}}}=\frac{\lambda_\alpha^{\bar{F}}}{6\Omega_{\hat{\mathcal{L}}}}\Big[\Big(\langle\vec{\tau}_{\bar{F}}^{JK},\overrightarrow{\hat{L}J}\rangle\,K_{\hat{L}\bar{F}}^{n}-h_{\hat{L}}^{\bar{F}}\big|\vec{N}_{\bar{F}}\big|K_{\hat{L}\bar{F}}^{JK}\Big)\big(p_J-p_I\big)-2\big|\vec{N}_{\bar{F}}\big|^2K_{\hat{L}\bar{F}}^{n}\big(p_J-p_{\hat{L}}\big)$$
$$+\Big(\langle\vec{\tau}_{\bar{F}}^{JI},\overrightarrow{\hat{L}J}\rangle\,K_{\hat{L}\bar{F}}^{n}-h_{\hat{L}}^{\bar{F}}\big|\vec{N}_{\bar{F}}\big|K_{\hat{L}\bar{F}}^{JI}\Big)\big(p_K-p_J\big)\Big] \tag{3.42}$$

and:

$$\vec{v}_\alpha^{\,p}\cdot\vec{S}_{\hat{R}}^{\hat{\mathcal{R}}}=\frac{\lambda_\alpha^{\bar{F}}}{6\Omega_{\hat{\mathcal{R}}}}\Big[\Big(\langle\vec{\tau}_{\bar{F}}^{JK},\overrightarrow{J\hat{R}}\rangle\,K_{\hat{R}\bar{F}}^{n}-h_{\hat{R}}^{\bar{F}}\big|\vec{N}_{\bar{F}}\big|K_{\hat{R}\bar{F}}^{JK}\Big)\big(p_I-p_J\big)+2\big|\vec{N}_{\bar{F}}\big|^2K_{\hat{R}\bar{F}}^{n}\big(p_{\hat{R}}-p_J\big)$$
$$+\Big(\langle\vec{\tau}_{\bar{F}}^{JI},\overrightarrow{J\hat{R}}\rangle\,K_{\hat{R}\bar{F}}^{n}-h_{\hat{R}}^{\bar{F}}\big|\vec{N}_{\bar{F}}\big|K_{\hat{R}\bar{F}}^{JI}\Big)\big(p_J-p_K\big)\Big] \tag{3.43}$$

where:

$$K_{\hat{k}\bar{F}}^{n}=\frac{\vec{N}_{\bar{F}}^{T}\mathbf{K}_{\hat{k}}\vec{N}_{\bar{F}}}{\big|\vec{N}_{\bar{F}}\big|^2};\;K_{\hat{k}\bar{F}}^{\beta\gamma}=\frac{\vec{N}_{\bar{F}}^{T}\mathbf{K}_{\hat{k}}\vec{\tau}_{\bar{F}}^{\beta\gamma}}{\big|\vec{N}_{\bar{F}}\big|^2};\;k=L,R;\;\beta,\gamma=I,J,K \tag{3.44}$$

Noting that $6\Omega_{\hat{\mathcal{R}}}=2\big|\vec{N}_{\bar{F}}\big|h_{\hat{R}}^{\bar{F}}$ (analogously to $\Omega_{\hat{\mathcal{L}}}$) and remembering that $\vec{N}_{\bar{F}}=\vec{S}_{\hat{L}}^{\hat{\mathcal{L}}}=-\vec{S}_{\hat{R}}^{\hat{\mathcal{R}}}$, we can rearrange the equations above as:

$$\frac{2\big|\vec{N}_{\bar{F}}\big|h_{\hat{L}}^{\bar{F}}}{K_{\hat{L}\bar{F}}^{n}}\vec{v}_\alpha^{\,p}\cdot\vec{N}_{\bar{F}}$$
$$=\lambda_\alpha^{\bar{F}}\Big[\Big(\langle\vec{\tau}_{\bar{F}}^{JK},\overrightarrow{\hat{L}J}\rangle-h_{\hat{L}}^{\bar{F}}\big|\vec{N}_{\bar{F}}\big|\frac{K_{\hat{L}\bar{F}}^{JK}}{K_{\hat{L}\bar{F}}^{n}}\Big)\big(p_J-p_I\big)-2\big|\vec{N}_{\bar{F}}\big|^2\big(p_J-p_{\hat{L}}\big) \tag{3.45}$$
$$-\Big(\langle\vec{\tau}_{\bar{F}}^{JI},\overrightarrow{\hat{L}J}\rangle-h_{\hat{L}}^{\bar{F}}\big|\vec{N}_{\bar{F}}\big|\frac{K_{\hat{L}\bar{F}}^{JI}}{K_{\hat{L}\bar{F}}^{n}}\Big)\big(p_J-p_K\big)\Big]$$

and:

$$\frac{2\left|\vec{N}_{\bar{F}}\right|h_{\hat{R}}^{\bar{F}}}{K_{\hat{R}\bar{F}}^{n}}\vec{v}_{\alpha}^{p}\cdot\vec{N}_{\bar{F}}$$
$$=\lambda_{\alpha}^{\bar{F}}\left[\left(\langle\vec{\tau}_{\bar{F}}^{JK},\overrightarrow{J\hat{R}}\rangle-h_{\hat{R}}^{\bar{F}}\left|\vec{N}_{\bar{F}}\right|\frac{K_{\hat{R}\bar{F}}^{JK}}{K_{\hat{R}\bar{F}}^{n}}\right)\left(p_{J}-p_{I}\right)+2\left|\vec{N}_{\bar{F}}\right|^{2}\left(p_{J}-p_{\hat{R}}\right)\right. \quad (3.46)$$
$$\left.-\left(\langle\vec{\tau}_{\bar{F}}^{JI},\overrightarrow{J\hat{R}}\rangle-h_{\hat{R}}^{\bar{F}}\left|\vec{N}_{\bar{F}}\right|\frac{K_{\hat{R}\bar{F}}^{JI}}{K_{\hat{R}\bar{F}}^{n}}\right)\left(p_{J}-p_{K}\right)\right]$$

Summing the Eq. (3.45) to Eq. (3.46) and after some algebraic manipulation, we can get the unique flux expression through face $\bar{F}$ as:

$$\vec{v}_{\alpha}^{p}\cdot\vec{N}_{\bar{F}}=-\lambda_{\alpha}^{\bar{F}}\mathfrak{K}_{\bar{F}}\left|\vec{N}_{\bar{F}}\right|\left[\left(p_{\hat{R}}-p_{\hat{L}}\right)-\frac{1}{2}\mathfrak{D}_{\bar{F}}^{JK}\left(p_{J}-p_{I}\right)+\frac{1}{2}\mathfrak{D}_{\bar{F}}^{JI}\left(p_{J}-p_{K}\right)\right] \quad (3.47)$$

in which $\lambda_{\alpha}^{\bar{F}}$ is taken from the CV upwind to the flow and with:

$$\mathfrak{K}_{\bar{F}}=\frac{K_{\hat{R}\bar{F}}^{n}K_{\hat{L}\bar{F}}^{n}}{h_{\hat{L}}^{\bar{F}}K_{\hat{R}\bar{F}}^{n}+h_{\hat{R}}^{\bar{F}}K_{\hat{L}\bar{F}}^{n}} \quad (3.48)$$

and:

$$\mathfrak{D}_{\bar{F}}^{\beta\gamma}=\frac{\langle\vec{\tau}_{\bar{F}}^{\beta\gamma},\overrightarrow{\hat{L}\hat{R}}\rangle}{\left|\vec{N}_{\bar{F}}\right|^{2}}-\frac{1}{\left|\vec{N}_{\bar{F}}\right|}\left(h_{\hat{L}}^{\bar{F}}\frac{K_{\hat{L}\bar{F}}^{\beta\gamma}}{K_{\hat{L}\bar{F}}^{n}}+h_{\hat{R}}^{\bar{F}}\frac{K_{\hat{R}\bar{F}}^{\beta\gamma}}{K_{\hat{R}\bar{F}}^{n}}\right);\ \beta,\gamma=I,J,K \quad (3.49)$$

Analogously, $\vec{v}_{\alpha}^{g}=\lambda_{\alpha}\rho_{\alpha}g\mathbf{K}\nabla z$ can be discretized as:

$$\vec{v}_{\alpha}^{g}\cdot\vec{N}_{\bar{F}}=\lambda_{\alpha}^{\bar{F}}\rho_{\alpha}^{\bar{F}}g\mathfrak{K}_{\bar{F}}\left|\vec{N}_{\bar{F}}\right|\left[\left(z_{\hat{R}}-z_{\hat{L}}\right)-\frac{1}{2}\mathfrak{D}_{\bar{F}}^{JK}\left(z_{J}-z_{I}\right)+\frac{1}{2}\mathfrak{D}_{\bar{F}}^{JI}\left(z_{J}-z_{K}\right)\right] \quad (3.50)$$

3.2.4 Flux expression for a boundary face

Based on the Eq. (3.42), the flux expression for $\bar{F}$ if it is a boundary face with prescribed values for p is given by:

$$\vec{v}_{\alpha}^{p} \cdot \vec{N}_{\bar{F}} = \frac{\lambda_{\alpha}^{\bar{F}}}{6\Omega_{\hat{\mathcal{L}}}} \Big[\Big(\langle \vec{\tau}_{\bar{F}}^{JK}, \overrightarrow{\hat{L}J} \rangle K_{\hat{L}\bar{F}}^{n} - h_{\hat{L}}^{\bar{F}} \big| \vec{N}_{\bar{F}} \big| K_{\hat{L}\bar{F}}^{JK} \Big) \big(g_D^J - g_D^I \big) - 2 \big| \vec{N}_{\bar{F}} \big|^2 K_{\hat{L}\bar{F}}^{n} \big(g_D^J - p_{\hat{L}} \big) + \Big(\langle \vec{\tau}_{\bar{F}}^{JI}, \overrightarrow{\hat{L}J} \rangle K_{\hat{L}\bar{F}}^{n} - h_{\hat{L}}^{\bar{F}} \big| \vec{N}_{\bar{F}} \big| K_{\hat{L}\bar{F}}^{JI} \Big) \big(g_D^K - g_D^J \big) \Big] \tag{3.51}$$

where g_D^I, g_D^J and g_D^K are known. When we have prescribed flux on $\bar{F}$, considering that g_N is its value, we can simply write the flux equation as:

$$\vec{v}_{\alpha} \cdot \overrightarrow{N}_{\bar{F}} = g_N \left| \overrightarrow{N}_{\bar{F}} \right| \tag{3.52}$$

3.2.5 Interpolation of vertex unknowns

In order to obtain a completely cell-centered formulation, it is necessary to eliminate the vertex unknowns p_I, p_J and p_K in Eq. (3.47). This is done by interpolating a vertex pressure p_Q as a weighted average of the values of $p_{\hat{k}}$, considering all the cells surrounding node Q, as described by the following expression:

$$p_Q = \sum_{\hat{k} \in \widehat{\mathbb{Q}}} \omega_{\hat{k}} p_{\hat{k}} \tag{3.53}$$

in which $\widehat{\mathbb{Q}}$ is the set of cells sharing node Q.

In the present work, three types of weighting strategies were studied, namely, the linearity preserving explicit weights (LPEW) (GAO; WU, 2011; LIRA FILHO et al., 2021), the LPEW based in averaging harmonic points (LPEW-HAP) (YANG; GAO, 2020) and the global least square (GLS) weighting (DONG; KANG, 2021, 2022).

The LPEW strategies presented here were developed within the PADMEC (High Performance Computing on Computational Mechanics) researching group in UFPE, as natural extensions of the 3-D LPEW formulations presented for 2-D domains by Gao and Wu (2011). These schemes are based on the imposition of the divergence free conditions on a support region surrounding Q. This support region can be constructed by different ways, which will characterize different types of LPEW strategies (LPEW1, LPEW2 and LPEW3). The construction of the support region and the flux calculation for the

divergence free imposition, however, involve some auxiliary variables (T_i, with $i = 1 \dots 6$) as shown in Figure 4a (that presents the LPEW2 configuration), which need to be eliminated to achieve a full cell-centered weighting expression.

Figure 4 – LPEW2 weighting strategy. (a) Part of a support region constructed surrounding Q. (b) Sketch of the tetrahedra used in the flux continuity imposition on faces QT_1T_2 and QT_2T_3.

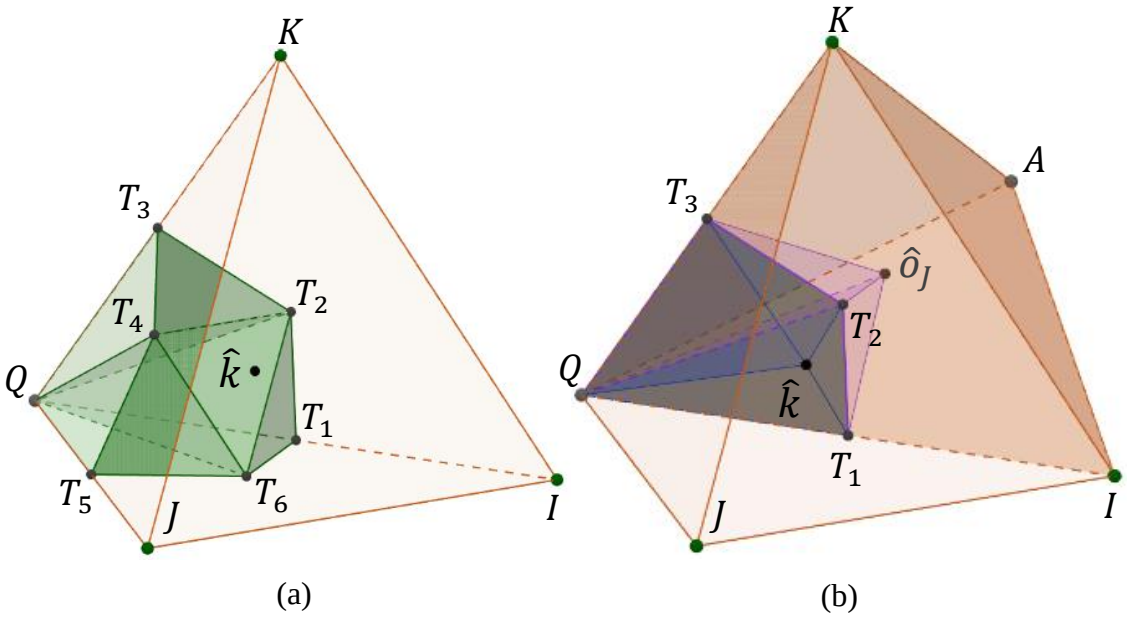

Source: The author (2023).

This elimination can be made by imposing the continuity condition on faces QT_iT_j (with $i, j = 1 \dots 6$) shared by two cells sharing Q. Figure 4b shows the faces QT_1T_2 and QT_2T_3 shared by the cells $\hat{k}$ and $\hat{o}_J$, on which the flux continuity can be imposed in order to eliminate T_1, T_2 and T_3 from the divergence free expression. All the mathematical development about LPEW strategies developed to obtain the final explicit weighting expressions, is presented in detail in Appendix A.

The LPEW-HAP strategy are based on the determination of harmonic averaging points on each face sharing Q. There is, for example, on face QIK, shown in Figure 4b, a harmonic averaging point on which the value of the pressure is a linear combination of the pressures $p_{\hat{k}}$ and $p_{\hat{o}_J}$. The same procedure can be performed for the faces QAK, QJK, QAI, QIJ and for all the other faces sharing Q. Then, we can use the pressures at these

harmonic averaging points, together with some linear basis functions, to determine a weighting expression for p_Q. All the mathematical development about LPEW-HAP, used to obtain the final explicit cell-centered expression is presented in detail in Appendix A.

The GLS strategy is based on minimizing the values of some functions. The first set of functions corresponds to the difference between linear approximations of the pressure in each cell surrounding Q and the actual pressures in them, which must be minimized. The second set of functions corresponds to the difference between the projections of pressure gradients in the neighboring cells sharing Q on each edge shared by them. In the situation shown by Figure 4b, for example, the projection of the vector $\nabla p_{\hat{k}} - \nabla p_{\hat{o}_J}$ on the edges QI and QK must be also minimized. The third set of functions corresponds to the flux continuity imposition on each face sharing Q. Writing these equations to each cell, edge and face surrounding Q gives rise to a system of equations from whose solution it is possible to get the GLS weighting for p_Q. All the mathematical development about GLS, until to obtain the interpolation weights, is presented in detail in Appendix A.

3.3 NON-LINEAR DEFECT CORRECTION FOR DMP VIOLATION

As commonly observed in applications of most of linear MPFA formulation, those studied strategies failed in satisfy DMP, what motivated the investigation and development of a non-linear alternative to correct this defect (CAVALCANTE et al., 2022), mainly based on the works of Pal and Edwards (2006, 2011), who proposed flux-splitting strategies to improve the monotonicity behavior and impose DMP for FVM, and of Kuzmin, Shashkov and Svyatskiy (2009), who presented a nonlinear constrained finite element scheme, in which they perform an algebraic matrix splitting followed by a slope limiting to impose DMP. Satisfying DMP is very important for diffusion terms in modelling two-phase flows in porous media (LE POTIER, 2009), in order to avoid spurious oscillations in pressure solution (PAL; EDWARDS, 2011) and non "physics-oriented" fluxes.

Considering the discretization of an elliptic boundary value problem, as described in Eq. (2.14) and with its adequate boundary conditions, on fluid pressure, disregarding gravity effects and in the absence of source terms, must be limited by the maximum and the minimum values found on the boundaries (VARGA, 1966; PAL; EDWARDS, 2011). In this context, the Eq. (3.47) would become:

$$\vec{v}_{\alpha}^{p} \cdot \vec{N}_{\bar{F}} = -\mathfrak{K}_{\bar{F}} \left|\vec{N}_{\bar{F}}\right| \left[(p_{\hat{R}} - p_{\hat{L}}) - \frac{1}{2} \mathfrak{D}_{\bar{F}}^{JK} (p_J - p_I) + \frac{1}{2} \mathfrak{D}_{\bar{F}}^{JI} (p_J - p_K) \right] \tag{3.54}$$

and it could be rewritten as:

$$\vec{v}_{\alpha}^{p} \cdot \vec{N}_{\bar{F}} = \left(\vec{v}_{\alpha}^{p} \cdot \vec{N}_{\bar{F}}\right)_{TPFA} + \left(\vec{v}_{\alpha}^{p} \cdot \vec{N}_{\bar{F}}\right)_{CDT} \tag{3.55}$$

with:

$$\left(\vec{v}_{\alpha}^{p} \cdot \vec{N}_{\bar{F}}\right)_{TPFA} = -\mathfrak{K}_{\bar{F}} \left|\vec{N}_{\bar{F}}\right| [(p_{\hat{R}} - p_{\hat{L}})] \tag{3.56}$$

and:

$$\left(\vec{v}_{\alpha}^{p} \cdot \vec{N}_{\bar{F}}\right)_{CDT} = -\mathfrak{K}_{\bar{F}} \left|\vec{N}_{\bar{F}}\right| \left[-\frac{1}{2} \mathfrak{D}_{\bar{F}}^{JK} (p_J - p_I) + \frac{1}{2} \mathfrak{D}_{\bar{F}}^{JI} (p_J - p_K) \right] \tag{3.57}$$

Thus, $\left(\vec{v}_{\alpha}^{p} \cdot \vec{N}_{\bar{F}}\right)_{TPFA}$ is the TPFA contribution for the flux and $\left(\vec{v}_{\alpha}^{p} \cdot \vec{N}_{\bar{F}}\right)_{CDT}$ is the flux contribution from the cross diffusion terms (CDT), provided by the interpolated nodal values. Based in Eq. (3.18) and Eq. (2.14), we can write:

$$\sum_{\bar{F} \in \hat{L}} \rho_{\alpha} \left(\vec{v}_{\alpha}^{p} \cdot \vec{N}_{\bar{F}}\right) = \rho_{\alpha} q_{\alpha} \tag{3.58}$$

Computing Eq. (3.58) for all the control-volumes in the domain, we obtain the global system of equations $\boldsymbol{Ap} = \boldsymbol{b}$. The solution of this system can be obtained iteratively by the Gauss-Seidel method:

$$\boldsymbol{p}^{\upsilon+1} = (\boldsymbol{D} + \boldsymbol{L})^{-1} \{\boldsymbol{b} - \boldsymbol{U}\boldsymbol{p}^{\upsilon}\} \tag{3.59}$$

where υ is the iteration step and $\boldsymbol{D}$ is the diagonal matrix of $\boldsymbol{A}$, $\boldsymbol{U}$ is the upper triangular part of $\boldsymbol{A}$, $\boldsymbol{L}$ is the lower triangular part of $\boldsymbol{A}$, so that $\boldsymbol{A} = \boldsymbol{L} + \boldsymbol{D} + \boldsymbol{U}$. Naturally, being n_{tetra} the amount of tetrahedra discretizing Ω_m, $\boldsymbol{A}$ is a $n_{tetra} \times n_{tetra}$ matrix, in which

the L-th line corresponds to $\sum_{\bar{k}\in\Gamma_{\hat{L}}}\left(\vec{v}_{\alpha}^{\,p}\cdot\vec{N}_{\bar{F}}\right)\big|_{\bar{k}}$. Splitting the fluxes according to Eq. (3.55), we can write the global system of equations as:

$$[\boldsymbol{A_{TPFA}}+\boldsymbol{A_{CDT}}]\boldsymbol{p}=[\boldsymbol{b_{TPFA}}+\boldsymbol{b_{CDT}}] \tag{3.60}$$

in which the L-th line of $\boldsymbol{A_{TPFA}}$ corresponds to $\sum_{\bar{k}\in\Gamma_{\hat{L}}}\left(\vec{v}_{\alpha}^{\,p}\cdot\vec{N}_{\bar{F}}\right)_{TPFA}\Big|_{\bar{k}}$ and the L-th line of $\boldsymbol{A_{CDT}}$ corresponds to $\sum_{\bar{k}\in\Gamma_{\hat{L}}}\left(\vec{v}_{\alpha}^{\,p}\cdot\vec{N}_{\bar{F}}\right)_{CDT}\Big|_{\bar{k}}$, according to Eq. (3.56) and Eq. (3.57), respectively. The expression shown in Eq. (3.60) is the regular MPFA-D global system under the described splitting. The solution of Eq. (3.60) can still be obtained iteratively by the Gauss-Seidel method, but in the following form:

$$\begin{aligned}\boldsymbol{p}^{\upsilon+1}=(\boldsymbol{D_{TPFA}}+\boldsymbol{D_{CDT}}+\boldsymbol{L_{TPFA}}+\boldsymbol{L_{CDT}})^{-1}\{&\boldsymbol{b_{TPFA}}+\boldsymbol{b_{CDT}}\\&-[\boldsymbol{U_{TPFA}}+\boldsymbol{U_{CDT}}]\boldsymbol{p}^{\upsilon}\}\end{aligned} \tag{3.61}$$

After each iteration in Eq. (3.61), aiming to guarantee monotonicity through a local DMP imposition, we need to verify the compliance of the following restriction (PAL; EDWARDS, 2011):

$$\boldsymbol{p}_{\boldsymbol{min}}^{\upsilon}-\delta\leq\boldsymbol{p}^{\upsilon+1}\leq\boldsymbol{p}_{\boldsymbol{max}}^{\upsilon}+\delta \tag{3.62}$$

with the above inequality being an entry-by-entry evaluation, where $\boldsymbol{p}_{\boldsymbol{max}}^{\upsilon}$ and $\boldsymbol{p}_{\boldsymbol{min}}^{\upsilon}$ are the vectors containing, respectively, the maximum and the minimum scalar values in the extended stencil of each cell after the υ-th iteration and δ is a pre-established tolerance. The extended stencil of a cell (i.e., control volume) includes the cell itself and all the neighboring cells sharing vertices with it. Two important exceptions to the application of Eq. (3.62) are when the evaluated cell has the maximum source term or the minimum sink term in the extended stencil or when it has Neumann boundary faces in which $g_N\neq 0$. In these cases, the restriction in Eq. (3.62) is simply skipped (PAL; EDWARDS, 2011). If the restriction shown in Eq. (3.62) is violated by the approximation, we need to modify the system shown in Eq. (3.61) in order to impose the DMP. As the potential source of spurious oscillations in the MPFA-D are the fluxes associated to the CDT (PAL; EDWARDS, 2011; CAVALCANTE et al., 2022), we modify it as follows:

$$\boldsymbol{p}^{\upsilon+1} = (\boldsymbol{D_{TPFA}} + \boldsymbol{\Upsilon D_{CDT}} + \boldsymbol{L_{TPFA}} + \boldsymbol{\Upsilon L_{CDT}})^{-1}\{\boldsymbol{b_{TPFA}} + \boldsymbol{\Upsilon b_{CDT}} - [\boldsymbol{U_{TPFA}} + \boldsymbol{\Upsilon U_{CDT}}]\boldsymbol{p}^{\upsilon}\} \tag{3.63}$$

where $\boldsymbol{\Upsilon}$ is a diagonal matrix, with entries $0 \leq \Upsilon_{ii} \leq 1$, used to weight the CDT contributions. Note that with $\boldsymbol{\Upsilon} = \boldsymbol{I}$ (the identity matrix), we get back to Eq. (3.61), i.e., the iterative version of the original MPFA-D, on the other hand, if $\boldsymbol{\Upsilon} = \boldsymbol{0}$, we get the iterative version of the TPFA formulation. Rearranging the expression in Eq. (3.63), we get:

$$\boldsymbol{p}^{\upsilon+1} = (\boldsymbol{D_{TPFA}} + \boldsymbol{L_{TPFA}} + \boldsymbol{\Upsilon D_{CDT}} + \boldsymbol{\Upsilon L_{CDT}})^{-1}[\boldsymbol{b_{TPFA}} - \boldsymbol{U_{TPFA}}\boldsymbol{p}^{\upsilon} + \boldsymbol{\Upsilon b_{CDT}} - \boldsymbol{\Upsilon U_{CDT}}\boldsymbol{p}^{\upsilon}] \tag{3.64}$$

Replacing Eq. (3.64) in Eq. (3.62) and disregarding the tolerance δ for now, we have the two following inequalities sets:

$$\begin{cases} (\boldsymbol{D_{TPFA}} + \boldsymbol{L_{TPFA}} + \boldsymbol{\Upsilon D_{CDT}} + \boldsymbol{\Upsilon L_{CDT}})^{-1}\begin{bmatrix} \boldsymbol{b_{TPFA}} - \boldsymbol{U_{TPFA}}\boldsymbol{p}^{\upsilon} \\ +\boldsymbol{\Upsilon b_{CDT}} - \boldsymbol{\Upsilon U_{CDT}}\boldsymbol{p}^{\upsilon} \end{bmatrix} \leq \boldsymbol{p}^{\upsilon}_{\boldsymbol{max}} \\ (\boldsymbol{D_{TPFA}} + \boldsymbol{L_{TPFA}} + \boldsymbol{\Upsilon D_{CDT}} + \boldsymbol{\Upsilon L_{CDT}})^{-1}\begin{bmatrix} \boldsymbol{b_{TPFA}} - \boldsymbol{U_{TPFA}}\boldsymbol{p}^{\upsilon} \\ +\boldsymbol{\Upsilon b_{CDT}} - \boldsymbol{\Upsilon U_{CDT}}\boldsymbol{p}^{\upsilon} \end{bmatrix} \geq \boldsymbol{p}^{\upsilon}_{\boldsymbol{min}} \end{cases} \tag{3.65}$$

Rearranging the system, we have:

$$\begin{cases} \boldsymbol{y_{max}} + \boldsymbol{\Upsilon x_{max}} \geq \boldsymbol{0} \\ \boldsymbol{y_{min}} + \boldsymbol{\Upsilon x_{min}} \leq \boldsymbol{0} \end{cases} \tag{3.66}$$

where:

$$\begin{aligned} \boldsymbol{x_{max}} &= \boldsymbol{U_{CDT}}\boldsymbol{p}^{\upsilon} + \boldsymbol{D_{CDT}}\boldsymbol{p}^{\upsilon}_{\boldsymbol{max}} + \boldsymbol{L_{CDT}}\boldsymbol{p}^{\upsilon}_{\boldsymbol{max}} - \boldsymbol{b_{CDT}} \\ \boldsymbol{y_{max}} &= \boldsymbol{U_{TPFA}}\boldsymbol{p}^{\upsilon} + \boldsymbol{D_{TPFA}}\boldsymbol{p}^{\upsilon}_{\boldsymbol{max}} + \boldsymbol{L_{TPFA}}\boldsymbol{p}^{\upsilon}_{\boldsymbol{max}} - \boldsymbol{b_{TPFA}} \\ \boldsymbol{x_{min}} &= \boldsymbol{U_{CDT}}\boldsymbol{p}^{\upsilon} + \boldsymbol{D_{CDT}}\boldsymbol{p}^{\upsilon}_{\boldsymbol{min}} + \boldsymbol{L_{CDT}}\boldsymbol{p}^{\upsilon}_{\boldsymbol{min}} - \boldsymbol{b_{CDT}} \\ \boldsymbol{y_{min}} &= \boldsymbol{U_{TPFA}}\boldsymbol{p}^{\upsilon} + \boldsymbol{D_{TPFA}}\boldsymbol{p}^{\upsilon}_{\boldsymbol{min}} + \boldsymbol{L_{TPFA}}\boldsymbol{p}^{\upsilon}_{\boldsymbol{min}} - \boldsymbol{b_{TPFA}} \end{aligned} \tag{3.67}$$

Therefore, we can determine valid intervals ($Y_{max}^{\hat{\imath}}$ and $Y_{min}^{\hat{\imath}}$) for the values of Υ_{ii}. Considering that $x_{max,i}$ is the i-th entry of $\boldsymbol{x_{max}}$ (analogously to the similar arrays), the possible solutions to inequalities in Eq. (3.66) are given by:

$$Y_{max}^{\hat{\imath}} = \begin{cases} if\ x_{max,i} > 0 \rightarrow \left[-\dfrac{y_{max,i}}{x_{max,i}}, \infty \right) \\ if\ x_{max,i} < 0 \rightarrow \left(-\infty, -\dfrac{y_{max,i}}{x_{max,i}} \right] \\ if\ x_{max,i} = 0 \rightarrow [0,1] \end{cases} \tag{3.68}$$

and:

$$Y_{min}^{\hat{\imath}} = \begin{cases} if\ x_{min,i} > 0 \rightarrow \left(-\infty, -\dfrac{y_{min,i}}{x_{min,i}} \right] \\ if\ x_{min,i} < 0 \rightarrow \left[-\dfrac{y_{min,i}}{x_{min,i}}, \infty \right) \\ if\ x_{min,i} = 0 \rightarrow [0,1] \end{cases} \tag{3.69}$$

Therefore, we can define $Y^{\hat{\imath}}$ as:

$$Y^{\hat{\imath}} = \begin{cases} if\ \ \boldsymbol{p}_i^{v+1} \leq \boldsymbol{p}_{\boldsymbol{min},i}^{v} \rightarrow Y_{min}^{\hat{\imath}} \cap [0,1] \\ if\ \ \boldsymbol{p}_i^{v+1} \geq \boldsymbol{p}_{\boldsymbol{max},i}^{v} \rightarrow Y_{max}^{\hat{\imath}} \cap [0,1] \\ else\ \rightarrow Y_{max}^{\hat{\imath}} \cap Y_{min}^{\hat{\imath}} \cap [0,1] \end{cases} \tag{3.70}$$

If $Y^{\hat{\imath}} = \emptyset$, we just adopt $Y^{\hat{\imath}} = [0,1]$, but not before taking an additional step. Consider that $\widehat{\mathbb{V}}$ is the set of cells violating DMP, if $\hat{\imath} \in \widehat{\mathbb{V}}$ and $Y^{\hat{\imath}} = \emptyset$, we include in $\widehat{\mathbb{V}}$ all the cells in the extended stencil of $\hat{\imath}$, so we can try to fix it through modifying its neighbors.

Note that, multiplying $\boldsymbol{\Upsilon A_{CDT}}$, which means to multiply the i-th line of $\boldsymbol{A_{CDT}}$ by Υ_{ii}, would be the same thing that multiply each face flux of the cell $\hat{\imath}$ by Υ_{ii}. This would violate the mass conservation. Considering a face $\bar{k}$ shared by two cells $\hat{R}$ and $\hat{L}$, as shown in Figure 3, then the CDT flux through $\bar{k}$ is present in both L-th and R-th lines of $\boldsymbol{A_{CDT}}$. This way, through $\boldsymbol{\Upsilon A_{CDT}}$, the CDT flux through $\bar{k}$ would be multiplied by Υ_{LL} in the flux balance of $\hat{L}$ and by Υ_{RR} in the flux balance of $\hat{R}$. This would obviously destroy the flux

continuity on $\bar{k}$. Therefore, it is necessary to determine a unique value ϖ as the weighting factor to the cross-diffusion flux on each cell face in the interval $F^{\bar{k}}$, such that:

$$\varpi_{\bar{k}} \in F^{\bar{k}} = Y^{\hat{L}} \cap Y^{\hat{R}} \tag{3.71}$$

On the other hand, if $F^{\bar{k}} = \emptyset$, we perform a different procedure, in which we need to verify if there is any DMP violation at $\hat{L}$ or $\hat{R}$. If the DMP violation occurs only at $\hat{L}$, then $F^{\bar{k}} = Y^{\hat{L}}$. Analogously, if there is a DMP violation only at $\hat{R}$, then $F^{\bar{k}} = Y^{\hat{R}}$. However, if there is a DMP violation at both $\hat{L}$ and $\hat{R}$, we simply use $F^{\bar{k}} = \left\{0.5\left[\min\left(Y^{\hat{L}}\right) + \min\left(Y^{\hat{R}}\right)\right], 0.5\left[\max\left(Y^{\hat{L}}\right) + \max\left(Y^{\hat{R}}\right)\right]\right\}$. For the case where there is no DMP violation, $F^{\bar{k}} = [0,1]$. Then the unique value of $\varpi_{\bar{k}}$ is defined as:

$$\varpi_{\bar{k}} = \begin{cases} if\ \ \max\left(F^{\bar{k}}\right) < 1 \rightarrow \max\left(F^{\bar{k}}\right) \\ if\ \ \max\left(F^{\bar{k}}\right) = 1 \rightarrow 0.5\left[\min\left(F^{\bar{k}}\right) + \max\left(F^{\bar{k}}\right)\right] \end{cases} \tag{3.72}$$

Thus, we can see that as we have defined $\widehat{\mathbb{V}}$ as a set of cells violating DMP, we need to define a set of faces $\overline{\mathbb{F}}$ whose CDT flux will be modified to avoid spurious solutions. This set will consist of all the faces comprising the cells in $\widehat{\mathbb{V}}$. Then, to formally guarantee flux continuity through a face $\bar{k} \in \overline{\mathbb{F}}$, $\boldsymbol{A_{CDT}}$ must be corrected as follows:

$$\begin{cases} \boldsymbol{A}_{\boldsymbol{CDT}}^{\hat{L}} = \boldsymbol{A}_{\boldsymbol{CDT}}^{\hat{L}} + (\varpi_{\bar{k}} - 1)\left[\left(\vec{v}_{\alpha}^{\,p} \cdot \vec{N}_{\bar{k}}\right)_{CDT}\Big|_{\bar{k} \in \overline{\mathbb{F}}}\right] \\ \boldsymbol{A}_{\boldsymbol{CDT}}^{\hat{R}} = \boldsymbol{A}_{\boldsymbol{CDT}}^{\hat{R}} - (\varpi_{\bar{k}} - 1)\left[\left(\vec{v}_{\alpha}^{\,p} \cdot \vec{N}_{\bar{k}}\right)_{CDT}\Big|_{\bar{k} \in \overline{\mathbb{F}}}\right] \end{cases} \tag{3.73}$$

Evidently, $\boldsymbol{D_{CDT}}$, $\boldsymbol{U_{CDT}}$, $\boldsymbol{L_{CDT}}$ and $\boldsymbol{b_{CDT}}$ will be modified accordingly, because of the modification of $\boldsymbol{A_{CDT}}$. Since we compute $\varpi_{\bar{k}}$ explicitly, face by face in $\overline{\mathbb{F}}$, these modifications may give rise to some undesirable side effects in other cells in terms of DMP violation. Therefore, the process described by Eq. (3.65) to Eq. (3.73) is repeated, as shown in the algorithm of Figure 5, until the condition given in Eq. (3.62) is fulfilled.

As it is well known that the classic linear TPFA method is a monotone formulation (MØYNER; LIE, 2014), we note that such a condition will be necessarily satisfied, at least in the extreme case in which $\boldsymbol{\Upsilon} = \boldsymbol{0}$ and the CDT terms vanish. Thus,

since we ensure the DMP in each iteration, the converged solution will undoubtedly satisfy the DMP.

Besides, this algorithm considers the solution to be converged when the iteration residue at the υ-th iteration ($\mathfrak{r}_\upsilon = \|\boldsymbol{p}^\upsilon - \boldsymbol{p}^{\upsilon-1}\|_2$) is $\mathfrak{r}_\upsilon < 10^{-3}\mathfrak{r}_1$, where $\mathfrak{r}_1$ is the first iteration residue, calculated from the initial guess $\boldsymbol{p}^0$.

Figure 5 - The MPFA-DNL algorithm.

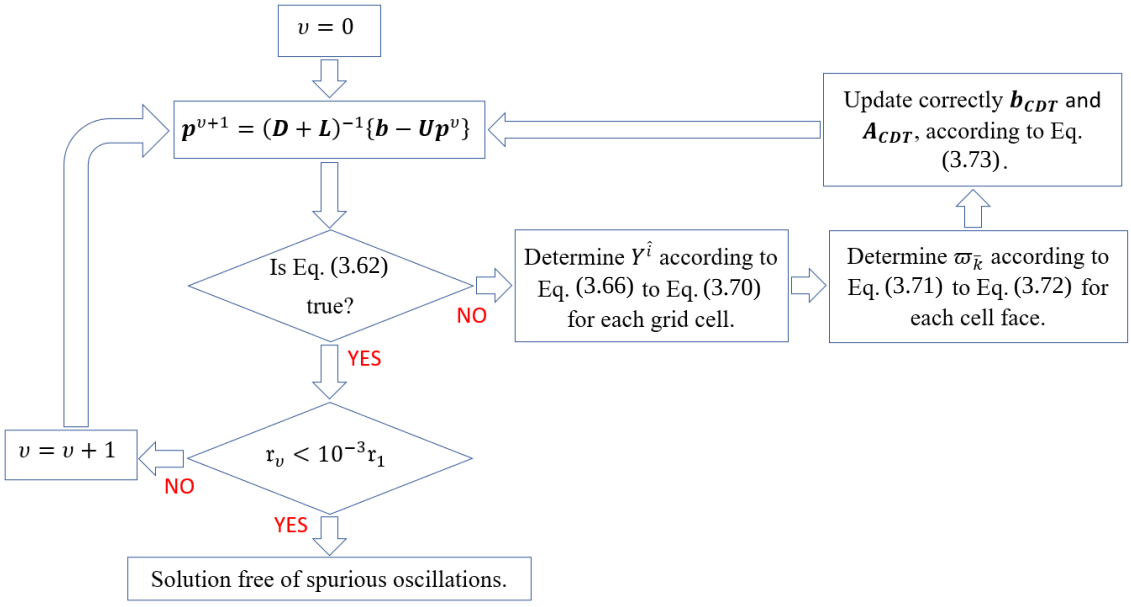

Source: The author (2023).

4 MODELING FRACTURES

This section presents some strategies developed over the years in order to add to the numerical models the contribution of large-scale fractures (LEE; LOUGH; JENSEN, 2001; LI; LEE, 2008). Starting by showing some classical schemes and finally highlighting those that are relevant for the present work, namely the Embedded Discrete Fracture Model (EDFM) and its projection-based version (pEDFM).

4.1 CLASSICAL FRACTURE MODELS

Historically, the most commonly used strategies to handle fractures in the context of flow simulation in porous media are the dual-continuum models. The theoretical foundation behind this type of scheme was initially developed by Barenblatt, Zheltov and Kochina (1960) and, based on it, Warren and Root (1963) introduced the two porosity systems in the context of reservoir engineering. The dual-porosity model considers the reservoir to be comprised by two continua, one representing the rock matrix and the other, the fractures network. Since the fractures are dominant in the flow driving, in this model, each block discretizing the matrix (each orange square in Figure 6a) is considered to be bounded by the fractures network (green media in Figure 6a), without direct connection between two matrix blocks, so that each one communicates only with the fractures network (see Figure 6a). The mathematical formulation is obtained by applying the mass conservation principles for each continuum and the fluid flow between fractures and the matrix blocks is accounted as source terms (KAZEMI et al., 1976). An evolution of this model is the dual-porosity-dual-permeability scheme (GILMAN; KAZEMI, 1983; THOMAS; DIXON; PIERSON, 1983; ULEBERG; KLEPPE, 1996) in which the interactions between matrix blocks are also considered (Figure 6b). In these methods it is necessary to consider a complex set of parameters, such as the shape of the matrix block, re-infiltration process and diffusivity (ULEBERG; KLEPPE, 1996), to guarantee a precise representation of the physical flow phenomena. These models are still not capable to deal with high fracture density and localized anisotropy due to the directions of the fractures (MOINFAR et al., 2011).

The method of transmissibility multipliers (MANZOCCHI et al., 1999; NILSEN; LIE; NATVIG, 2012), beyond being very dependent on the mesh (BERRE; DOSTER; KEILEGAVLEN, 2019), it does not represent high permeability fractures

adequately. Considering, for example, the configuration shown in Figure 7, in which, originally, the cells $\hat{L}$ and $\hat{R}$ were sharing a face $\bar{F}$, so that the transmissibility between them was $\mathfrak{T}_{\bar{F}}$ (see Figure 7a). However, if there is a fracture between $\hat{L}$ and $\hat{R}$ (see Figure 7b), due to the presence of the fracture, the referred transmissibility is modified as following (NILSEN; LIE; NATVIG, 2012):

Figure 6 - Sketch representing dual-continuum models. (a) Dual-porosity. (b) Dual-porosity-dual-permeability.

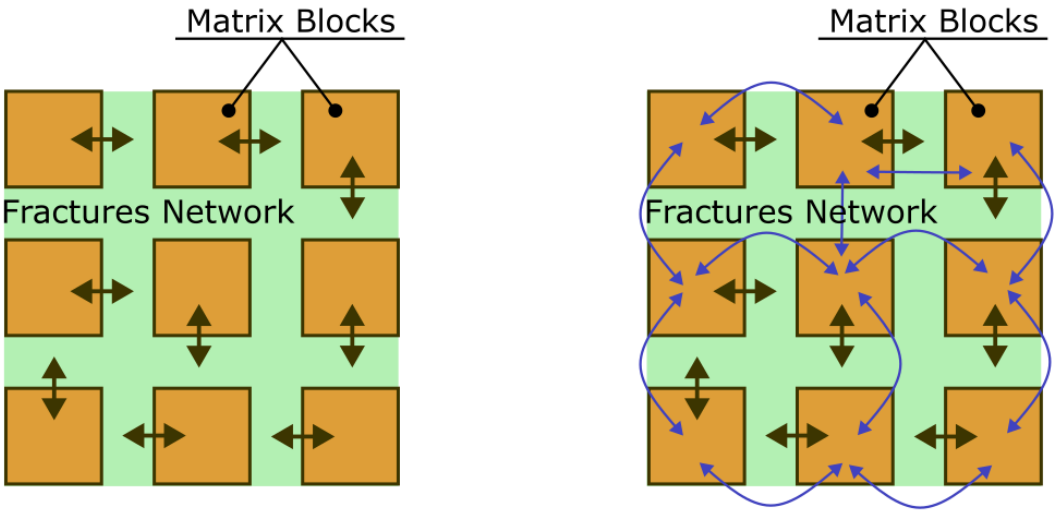

(a) (b)

Source: The author (2023).

$$\mathfrak{T}^f_{\hat{L}\hat{R}} = \mathfrak{m}^f_{\hat{L}\hat{R}}\mathfrak{T}_{\bar{F}} \quad \text{with} \quad \mathfrak{m}^f_{\hat{L}\hat{R}} = \frac{\mathfrak{T}_f}{\mathfrak{T}_f + \mathfrak{T}_{\bar{F}}} \tag{4.1}$$

in which the multiplying factor $\mathfrak{m}^f_{\hat{L}\hat{R}}$ is composed by the transmissibility of the fracture ($\mathfrak{T}_f$) and the transmissibility $\mathfrak{T}_{\bar{F}}$ of the face originally shared by $\hat{L}$ and $\hat{R}$ (disregarding the fracture). Note that the higher is $\mathfrak{T}_f$, the less influential the fracture is in the transmissibility between $\hat{L}$ and $\hat{R}$ ($\mathfrak{m}^f_{\hat{L}\hat{R}}$ approaches 1), which is the opposite of what is expected.

Looking at these important limitations of the classical methods that are used to model fractures, some more recent alternatives were investigated in order to reproduce, in a more physics-based way, the effects of the presence of the fractures in fluid flows in porous media. In the present work, we specifically concentrate on those that represent the

fractures explicitly, as additional degrees of freedom to the problem (HOTEIT; FIROOZABADI, 2008). Usually, these methods can be divided into two main groups, based on the relative positioning of the fractures and the meshes used in the spatial discretization: conforming mesh and non-conforming mesh schemes (JIANG; YOUNIS, 2017).

Figure 7 - Sketch representing the transmissibility multipliers method. (a) Original transmissibility between $\hat{L}$ and $\hat{R}$. (b) Modified transmissibility between $\hat{L}$ and $\hat{R}$, due to the presence of the fracture.

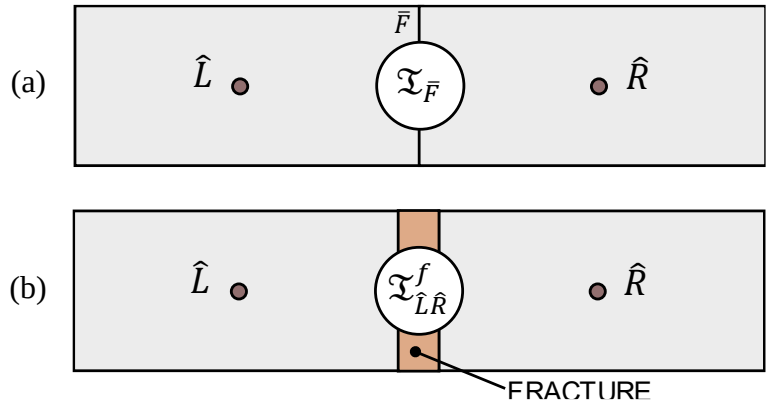

Source: The author (2023).

When applying conforming mesh methods (KARIMI-FARD; DURLOFSKY; AZIZ, 2004; SANDVE; BERRE; NORDBOTTEN, 2012; DEVLOO; TENG; ZHANG, 2019; CAVALCANTE et al., 2020; WANG et al., 2022), it is necessary to build the mesh discretizing the rock matrix in a way to accommodate the fracture positions, which need to be placed at the edges (in 2-D) or faces (in 3-D) of the grid cells. This condition is critical when it is necessary to discretize small angles and small distances between the fractures and can lead to localized and excessive mesh refinements, as shown in Figure 8, which represents part of a triangular conforming mesh (2-D) discretizing a fractured domain. Anyhow, it is still possible to improve the mesh quality performing some corrections as the coalescing of points (whether from the fracture grid or from the rock matrix one), whenever distances or angles are less than tolerable (LIMA; DEVLOO; VILLEGAS, 2020).

Non-conforming mesh methods are much more flexible from the mesh generation point of view as it is not necessary to fit the fractures positions when building the mesh and the fractures may cross the rock matrix grid cells. In this group, there are the most relevant fracture representation strategies for the present work and which will

be detailed in the next sections, namely: the embedded discrete fracture model (EDFM) (LI; LEE, 2008; MOINFAR et al., 2014; SHAKIBA; SEPEHRNOORI, 2015) and the projection-based embedded discrete fracture model (pEDFM) (JIANG; YOUNIS, 2017; ŢENE et al., 2017; RAO et al., 2020; HOSSEINIMEHR et al., 2022).

Figure 8 – Localized over refinement because of small distances between the fractures (marked in red).

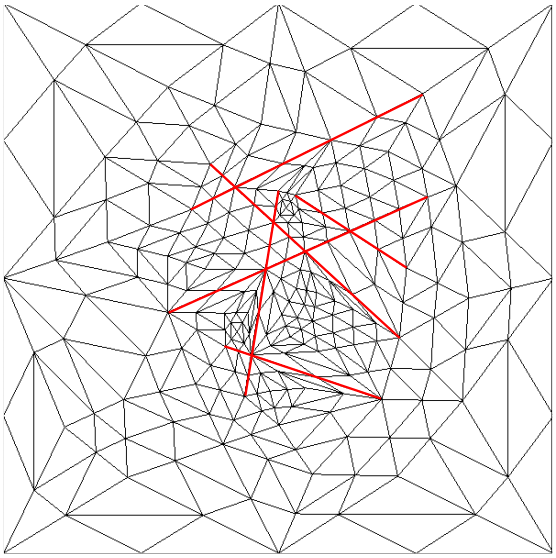

Source: The author (2023).

4.2 EMBEDDED DISCRETE FRACTURE MODEL

The embedded discrete fracture model (EDFM) (LI; LEE, 2008; MOINFAR et al., 2014; SHAKIBA; SEPEHRNOORI, 2015) is a non-conforming mesh method of representation of fractures in which the degrees of freedom of the rock matrix and fractures are discretized separately, but the structure of the coupling is similar to that of methods that represent fractures implicitly (as dual-continuum), with the difference that the coupling terms between the fracture cells and the rock matrix cells are modeled in terms of discrete variables directly (BERRE; DOSTER; KEILEGAVLEN, 2019), based on the permeabilities of the referred cells and on the geometric intersection between them.

4.2.1 Fracture-matrix and fracture-fracture intersections calculation

Let $\hat{t}$ be a generic tetrahedron defined by the intersections of the planes π_1, π_2, π_3 and π_4 (with normal vectors $\vec{n}_1$, $\vec{n}_2$, $\vec{n}_3$ and $\vec{n}_4$) and let Ω_{f_k} be the plane containing the

fracture cell $\check{k}_i$ (with normal vector $\vec{n}_{f_k}$). Considering that $\vec{P}_{f_k}$ is the position vector of a point on Ω_{f_k} and that $\vec{T}_1$, $\vec{T}_2$, $\vec{T}_3$ and $\vec{T}_4$ are the position vectors of the vertices of $\hat{t}$, we can verify if there exists any intersection between $\hat{t}$ and Ω_{f_k}, checking if there are vertices of $\hat{t}$ in different hemispaces defined by Ω_{f_k}. We verify this by the following inequality:

$$\left|\sum_{i=1}^{4} \frac{\langle \vec{n}_{f_k}, \vec{T}_i - \vec{P}_{f_k} \rangle}{\left|\langle \vec{n}_{f_k}, \vec{T}_i - \vec{P}_{f_k} \rangle\right|}\right| < 4 \tag{4.2}$$

where $\langle \vec{v}_1, \vec{v}_2 \rangle$ is the inner product between $\vec{v}_1$ and $\vec{v}_2$. If it is true, then there exists the intersection between $\hat{t}$ and Ω_{f_k}.

If $\Omega_{f_k} \cap \hat{t} \neq \emptyset$, we can calculate the area of the intersection between the plane that contains the fracture and the tetrahedron. First, using the inner product shown in Eq. (4.2), we verify how many points of the tetrahedron are on Ω_{f_k}. If three points of $\hat{t}$ are on Ω_{f_k}, one of the faces of $\hat{t}$ corresponds to $\Omega_{f_k} \cap \hat{t}$. If two points of $\hat{t}$ are on Ω_{f_k}, one of the edges of $\hat{t}$ corresponds to $\Omega_{f_k} \cap \hat{t}$. If one point of $\hat{t}$ is on Ω_{f_k}, this point corresponds to $\Omega_{f_k} \cap \hat{t}$. If there are not any points of $\hat{t}$ on Ω_{f_k}, the referred intersection can be calculated through the following algorithm: considering that $\vec{P}_i$ is the position vector of a point on π_i (as well as $\vec{P}_{f_k}$ on Ω_{f_k}), whose normal vector is $\vec{n}_i = [n_{ix} \quad n_{iy} \quad n_{iz}]^T$ (as well as $\vec{n}_{f_k}$ for Ω_{f_k}), the intersection between the edges of $\hat{t}$ and Ω_{f_k} will give rise to six linear systems, since a tetrahedron has six edges, each one established based on the equations defining the two planes whose intersection create the edge and the plane containing the fracture (STEIMBRUCH; WINTERLE, 1995). Therefore, we can write:

$$\begin{bmatrix} n_{ix} & n_{iy} & n_{iz} \\ n_{jx} & n_{jy} & n_{jz} \\ n_{f_kx} & n_{f_ky} & n_{f_kz} \end{bmatrix} \begin{bmatrix} x \\ y \\ z \end{bmatrix} = \begin{bmatrix} n_{ix}P_{ix} + n_{iy}P_{iy} + n_{iz}P_{iz} \\ n_{jx}P_{jx} + n_{jy}P_{jy} + n_{jz}P_{jz} \\ n_{f_kx}P_{f_kx} + n_{f_ky}P_{f_ky} + n_{f_kz}P_{f_kz} \end{bmatrix}; \begin{matrix} i,j = 1,2,3,4 \\ i \neq j \end{matrix} \tag{4.3}$$

whose solutions will define six points coordinates of which, however, only three (see Figure 9a) or four (see Figure 9b) will be on the faces of $\hat{t}$ (the others will be out of the tetrahedron). These three or four points will form the polygon $c = \Omega_{f_k} \cap \hat{t}$, as shown in Figure 9.

Thus, there are two polygons contained in Ω_{f_k} ($\check{k}_i$ and c) intersecting each other, so that we can define the polygon $d = \check{k}_i \cap c = \check{k}_i \cap \hat{t}$, as shown in Figure 10. Mathematically, the intersection operation is performed by finding the intersection points between each straight line containing the edges of $\check{k}_i$ and each straight line containing the edges c. Considering, for example, that $\vec{r} = (r_x, r_y, r_z)$ is the direction vector of a straight line $r = R + \mathrm{r}\vec{r}$ containing one edge of $\check{k}_i$ and that $\vec{s} = (s_x, s_y, s_z)$ is the direction vector of a straight line $s = S + \mathrm{s}\vec{s}$ containing one edge of c (STEIMBRUCH; WINTERLE, 1995), the intersection $r \cap s$ can be determined imposing:

$$R + \mathrm{r}\vec{r} = S + \mathrm{s}\vec{s} \tag{4.4}$$

Figure 9 – Intersection between Ω_{f_k} and $\hat{t}$. (a) Intersection defined by three points. (b) Intersection defined by four points.

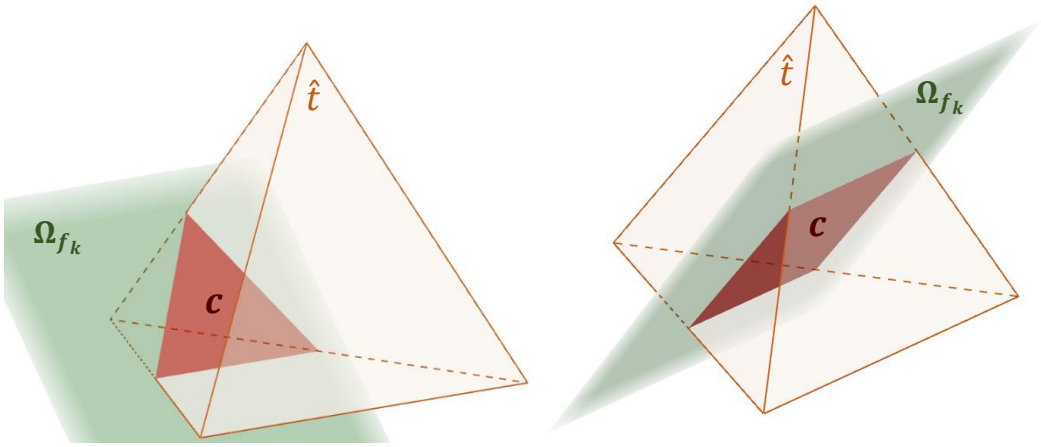

(a) (b)

Source: The author (2023).

then:

$$\mathrm{r}\vec{r} - \mathrm{s}\vec{s} = S - R \tag{4.5}$$

and:

$$\begin{bmatrix} r_x & -s_x \\ r_y & -s_y \\ r_z & -s_z \end{bmatrix} \begin{bmatrix} \mathcal{r} \\ \mathcal{s} \end{bmatrix} = \begin{bmatrix} S_x - R_x \\ S_y - R_y \\ S_z - R_z \end{bmatrix} \tag{4.6}$$

Thus, the values of the parameters $\mathcal{r}$ and $\mathcal{s}$ that will indicate the intersection coordinates are determined through the following equation:

$$\begin{bmatrix} \mathcal{r} \\ \mathcal{s} \end{bmatrix} = \left\{ \begin{bmatrix} r_x & -s_x \\ r_y & -s_y \\ r_z & -s_z \end{bmatrix}^T \begin{bmatrix} r_x & -s_x \\ r_y & -s_y \\ r_z & -s_z \end{bmatrix} \right\}^{-1} \begin{bmatrix} r_x & -s_x \\ r_y & -s_y \\ r_z & -s_z \end{bmatrix}^T \begin{bmatrix} S_x - R_x \\ S_y - R_y \\ S_z - R_z \end{bmatrix} \tag{4.7}$$

Figure 10 – Intersection between $\check{k}_i$ and c. (a) $\check{k}_i$, c and $\hat{t}$. (b) $d = \check{k}_i \cap c = \check{k}_i \cap \hat{t}$.

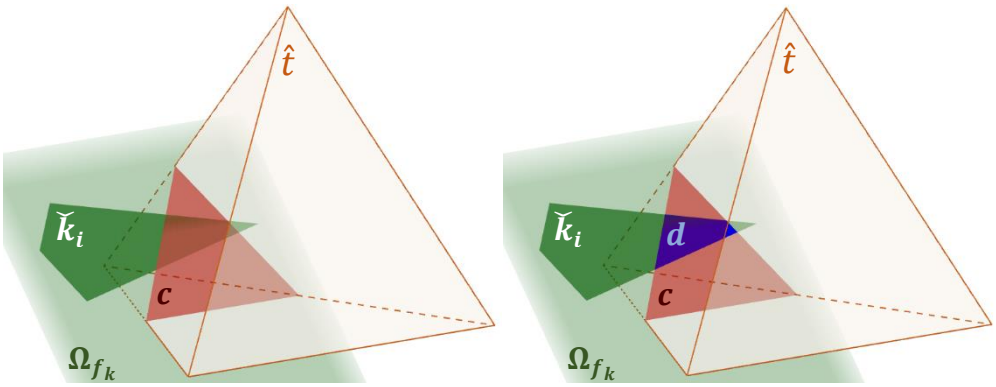

(a) (b)

Source: The author (2023).

Naturally, not all the intersection points will be part of $d = \check{k}_i \cap c$, but only those within the limits of the edges of the polygons $\check{k}_i$ and c, together with the vertices of $\check{k}_i$ inside c and the vertices of c inside $\check{k}_i$.

On the other hand, the intersection between two fracture cells, whenever they are not parallel, is calculated by the following algorithm: let Ω_{f_k} be the plane containing the fracture $\check{k}_i$ and let Ω_{f_h} be the plane containing the fracture $\check{h}_j$. Let $r = \Omega_{f_k} \cap \Omega_{f_h}$ be a straight line coplanar to $\check{k}_i$ and to $\check{h}_j$. We can determine the segments $s_1 = r \cap \check{k}_i$ and $s_2 = r \cap \check{h}_j$, calculated analogously to Eq. (4.7), so that $\check{k}_i \cap \check{h}_j = s_1 \cap s_2$, as shown in Figure 11.

Figure 11 – Intersection between $\check{k}_i$ and $\check{h}_j$. (a) $r = \Omega_{f_k} \cap \Omega_{f_h}$. (b) $s_1 = r \cap \check{k}_i$. (c) $s_2 = r \cap \check{h}_j$. (d) $s = s_1 \cap s_2 = \check{k}_i \cap \check{h}_j$.

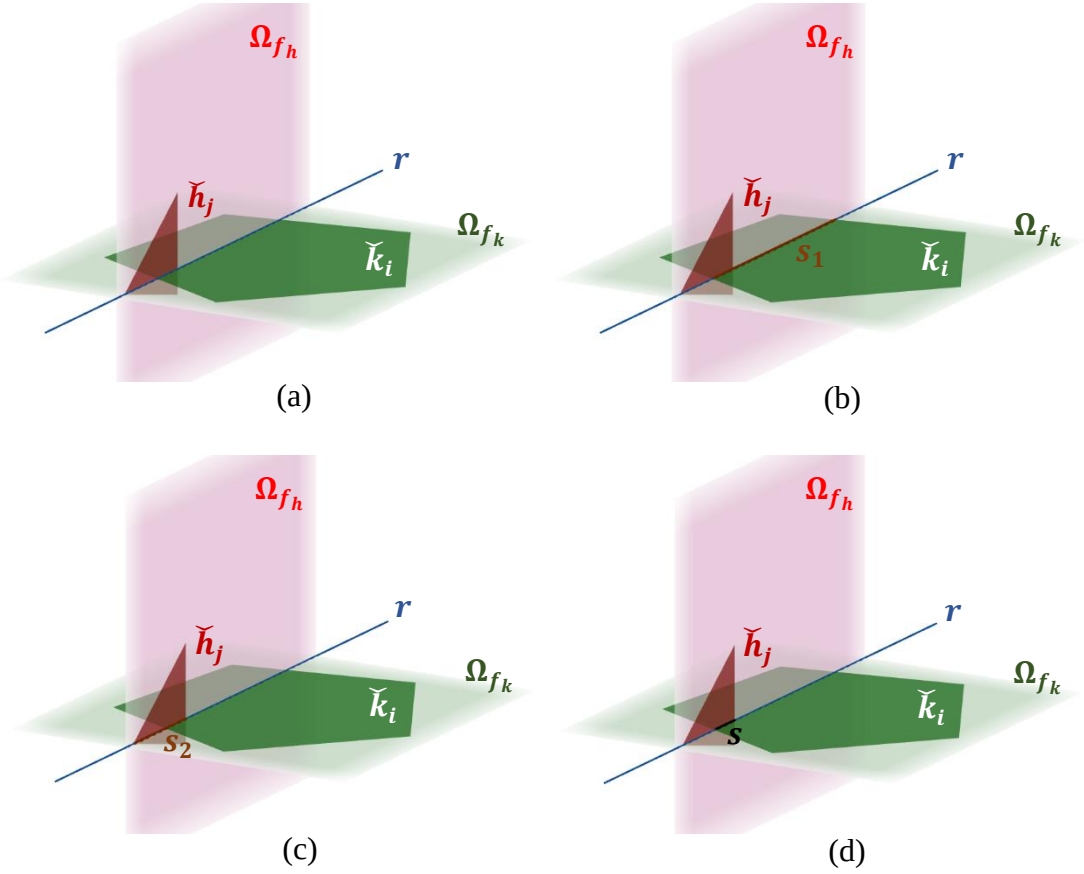

Source: The author (2023).

The area of the polygon $d = \hat{t} \cap \check{k}_i$ will be referred from now on as $A_{\hat{t},\check{k}_i}$ and will be used in the calculation of the transmissibility between $\hat{t}$ and $\check{k}_i$, while the length of $s = \check{k}_i \cap \check{h}_j$ will be referred from now as $L_{\check{k}_i,\check{h}_j}$ and will be used in the calculation of the transmissibility between $\check{h}_j$ and $\check{k}_i$.

4.2.2 The matrix-fracture flux calculation

As mentioned before, the terms in Eq. (3.11) and Eq. (3.12) corresponding to the phase flux between a tetrahedral cell $\hat{t}$ and a polygonal fracture cell $\check{k}_i$ are calculated

according to Eq. (3.6), in which ρ_α and λ_α are taken upwind and $\mathfrak{T}_{\hat{t},\check{k}_i}$ is calculated as (HOSSEINIMEHR et al., 2022):

$$\mathfrak{T}_{\hat{t},\check{k}_i} = \left[\frac{A_{\hat{t},\check{k}_i}}{\langle d_{\hat{t},\check{k}_i}\rangle}\right]\left[\frac{\left(\ell_{\hat{t}} + w_{f_k}\right)K^n_{\hat{t}\check{k}_i}K_{f_k}}{K^n_{\hat{t}\check{k}_i}w_{f_k} + K_{f_k}\ell_{\hat{t}}}\right] \tag{4.8}$$

where $\ell_{\hat{t}}$ is a characteristic size of the cell $\hat{t}$ (here, we adopted the cubic root of its volume), w_{f_k} is the aperture of the fracture Ω_{f_k}, K_{f_k} is so that the permeability tensor of Ω_{f_k} is $\mathbf{K}_{f_k} = K_{f_k}\boldsymbol{I}_{3\times3}$, with $\boldsymbol{I}$ being the identity matrix, and $K^n_{\hat{t}\check{k}_i}$ is defined analogously to Eq. (3.44), but considering a normal vector to the plane containing $\check{k}_i$. Moreover, $A_{\hat{t},\check{k}_i}$ is the area of $\hat{t}\cap\check{k}_i$ and $\langle d_{\hat{t},\check{k}_i}\rangle$ is calculated as:

$$\langle d_{\hat{t},\check{k}_i}\rangle = \int_{\Omega_{\hat{t}}} \left|\vec{r}_{\check{k}_i,\hat{t}}\cdot\vec{n}_{f_k}\right| d\Omega_{\hat{t}} \tag{4.9}$$

in which $\vec{r}_{\check{k}_i,\hat{t}}$ is a vector from the centroid of $\hat{t}\cap\check{k}_i$ to a point in $\Omega_{\hat{t}}$ and $\vec{n}_{\check{k}_i}$ is the unitary normal vector to $\check{k}_i$.

4.2.3 The fracture-fracture flux calculation

The term in Eq. (3.12) corresponding to the phase flux between two polygonal cells ($\check{k}_i$ and $\check{k}_j$) contained in the same fracture Ω_{f_k} and sharing an edge $\dot{E}$ (with $\vec{N}_{\dot{E}}$ outward to $\check{k}_i$) is calculated as (HOSSEINIMEHR et al., 2022):

$$\rho_\alpha\left(\vec{v}_\alpha\cdot\vec{N}_{\dot{E}}\right) = -\rho_\alpha\lambda_\alpha K_{f_k}\frac{L_{\check{k}_i,\check{k}_j}}{d_{\check{k}_i,\check{k}_j}}\left(p_{\check{k}_j} - p_{\check{k}_i}\right) \tag{4.10}$$

in which $L_{\check{k}_i,\check{k}_j}$ is the length of the edge shared by $\check{k}_i$ and $\check{k}_j$ and $d_{\check{k}_i,\check{k}_j}$ is the distance between their centroids. On the other hand, the phase transfer between two polygonal cells ($\check{k}_i$ and $\check{h}_j$) contained in different fractures Ω_{f_h} and Ω_{f_k} is calculated as (HOSSEINIMEHR et al., 2022):

$$(\rho_\alpha q_\alpha)_{\check{k}_i,\check{h}_j} = -(\rho_\alpha q_\alpha)_{\check{h}_j,\check{k}_i} = -\rho_\alpha \lambda_\alpha K^H_{\check{k}_i,\check{h}_j} \zeta_{\check{k}_i,\check{h}_j} \left(p_{\check{h}_j} - p_{\check{k}_i}\right) \tag{4.11}$$

in which $K^H_{\check{k}_i,\check{h}_j}$ is the harmonic mean between K_{f_k} and K_{f_h}, and:

$$\zeta_{\check{k}_i,\check{h}_j} = 2\frac{L_{\check{k}_i,\check{h}_j}}{\langle d_{\check{k}_i,\check{h}_j}\rangle + \langle d_{\check{h}_j,\check{k}_i}\rangle} \tag{4.12}$$

Again, in both cases, ρ_α and λ_α are taken upwind.

4.3 PROJECTION-BASED EMBEDDED DISCRETE FRACTURE MODEL

The EDFM is capable to produce excellent solutions for high permeability fractures, however, their application is limited whenever the fracture permeability is much lower than the rock matrix one (ŢENE et al., 2017), because the term $\mathfrak{T}_{\hat{t},\check{k}_i}$ in Eq. (4.8) tends to be smaller when the permeability of the fracture gets smaller, making $(\rho_\alpha q_\alpha)_{\hat{t},\check{k}_i}$, calculated according to Eq. (3.6), less influential in Eq. (3.11) and in the fluid displacement modeling. This is the opposite of the proper expected physical behavior since a low permeability fracture should work as a barrier to the fluid flow.

In order to overcome some of the limitations of EDFM, the projection-based embedded discrete fracture models (pEDFM) were developed (JIANG; YOUNIS, 2017; ŢENE et al., 2017; RAO et al., 2020; HOSSEINIMEHR et al., 2022). Based on the projections of the areas of fractures on some faces of the cells in which they are contained, this strategy computes the interaction between the fractures and neighboring cells sharing those faces that receive the projections, enriching the model. Besides, these projections also restrict the interactions between the two tetrahedrons sharing the faces that receive them, what makes pEDFM adequate to represent the barrier to the flow due to the presence of a low permeability fracture.

Initially, it was developed to be applied on Cartesian grids (JIANG; YOUNIS, 2017; ŢENE et al., 2017; RAO et al., 2020), later it was extended for corner-point grids (HOSSEINIMEHR et al., 2022) and, in the present work, for the first time in literature, we have adapted it for unstructured tetrahedral grids. When applying pEDFM on Cartesian or corner-point (structured) grids, we deal with a fracture that crosses a six-sided polyhedron, from which some of them are chosen to receive the projections that

will modify the formulation. Figure 12 shows a fracture cell $\check{k}_i$ intersecting a hexahedral cell $\hat{L}$, with the projections of the referred intersection on the faces $\bar{F}$ and $\bar{G}$ that are indicated by the red lines in the picture to the left. Through these projections, $\check{k}_i$ can interact with $\hat{R}$ and $\hat{S}$, and restricts their interaction with $\hat{L}$. Also, in Figure 12, to the right, we can see a light blue line, representing the set of projections of the fracture Ω_{f_k}, on various faces, along the domain.

In this case, as previously mentioned, there are additional transmissibility terms between $\check{k}_i$ and $\hat{R}$, and between $\check{k}_i$ and $\hat{S}$, whose calculation is not a fully resolved issue, as well as the choosing of the faces to receive the projections and the calculation of the remainder area of these faces to the interaction between $\hat{L}$ and $\hat{R}$ and between $\hat{L}$ and $\hat{S}$.

Ţene et al. (2017) proposed an expression for the transmissibility term between $\check{k}_i$ and $\hat{R}$ to be applied on k-orthogonal Cartesian grids, which is here adapted for the purposes of this work and that is applied on an expression similar to Eq. (3.6), as:

$$\mathfrak{T}_{\hat{R},\check{k}_i} = \left[\frac{A^{\bar{F}}_{\hat{L},\check{k}_i}}{\langle d_{\hat{R},\check{k}_i}\rangle}\right]\left[\frac{\left(w_{f_k} + \ell_{\hat{R}}\right)K^n_{\hat{R}\check{k}_i}K_{f_k}}{K^n_{\hat{R}\check{k}_i}w_{f_k} + K_{f_k}\ell_{\hat{R}}}\right] \tag{4.13}$$

in which $A^{\bar{F}}_{\hat{L},\check{k}_i}$ is the area of the projection $\mathrm{P}^{\bar{F}}_{\hat{L},\check{k}_i}$ of $\hat{L} \cap \check{k}_i$ on $\bar{F}$. Jiang and Younis (2017) realized, however, that, if $\hat{\mathrm{L}}$ (in Figure 12) is a ultra-low permeability cell, this would prevent communication between $\check{k}_i$ and $\hat{R}$, so that $\hat{L}$ should be used in the calculation of $\mathfrak{T}_{\hat{R},\check{k}_i}$. The expression proposed by them is here adapted as:

$$\mathfrak{T}_{\hat{R},\check{k}_i} = \left[\frac{A^{\bar{F}}_{\hat{L},\check{k}_i}}{\langle d_{\hat{R},\check{k}_i}\rangle}\right]\left[\frac{\left(w_{f_k} + \ell_{\hat{R}} + \ell_{\hat{L}}\right)K^n_{\hat{L}\check{k}_i}K^n_{\hat{R}\check{k}_i}K_{f_k}}{K^n_{\hat{L}\check{k}_i}K^n_{\hat{R}\check{k}_i}w_{f_k} + K^n_{\hat{L}\check{k}_i}K_{f_k}\ell_{\hat{R}} + K^n_{\hat{R}\check{k}_i}K_{f_k}\ell_{\hat{L}}}\right] \tag{4.14}$$

On the other hand, Rao et al. (2020) proposed that the influence of $\hat{L}$ should be the smaller, the smaller is the volume between $\check{k}_i$ and the face $\bar{F}$, in such a way that, if $\check{k}_i$ coincides with $\bar{F}$, the expression shown in Eq. (4.14) should become the one shown in Eq. (4.13). An alternative expression that meets the recommendations of Rao et al. (2020) can be:

Figure 12 - Fractures projections on mesh faces.

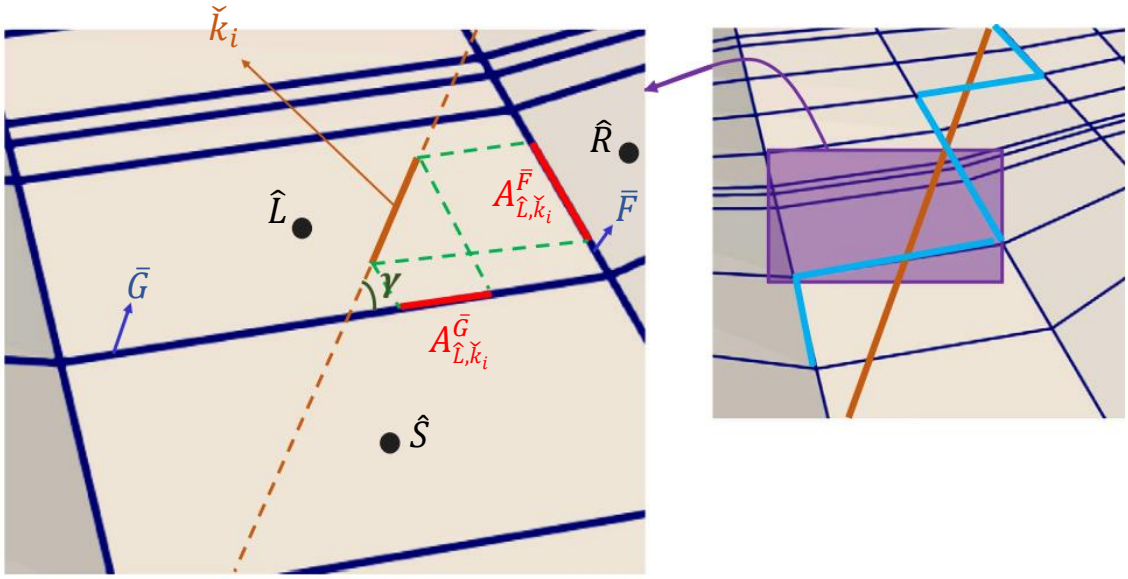

Source: Adapted from HosseiniMehr et al. (2022).

$$\mathfrak{T}_{\hat{R},\check{k}_i} = \left[\frac{A^{\bar{F}}_{\hat{L},\check{k}_i}}{\langle d_{\hat{R},\check{k}_i}\rangle}\right]\left[\frac{\left(w_{f_k} + \ell_{\hat{R}} + \frac{V^{\hat{L}}_{\check{k}_i\bar{F}}}{\Omega_{\hat{L}}}\ell_{\hat{L}}\right)K^n_{\hat{L}\check{k}_i}K^n_{\hat{R}\check{k}_i}K_{f_k}}{K^n_{\hat{L}\check{k}_i}K^n_{\hat{R}\check{k}_i}w_{f_k} + K^n_{\hat{L}\check{k}_i}K_{f_k}\ell_{\hat{R}} + \frac{V^{\hat{L}}_{\check{k}_i\bar{F}}}{\Omega_{\hat{L}}}K^n_{\hat{R}\check{k}_i}K_{f_k}\ell_{\hat{L}}}\right] \tag{4.15}$$

in which $V^{\hat{L}}_{\check{k}_i\bar{F}}$ is the volume of $\hat{L}$ between $\check{k}_i$ and the face $\bar{F}$. More than this, Rao et al. (2020) were also worried with the possibility of the interaction between $\check{k}_i$ and $\hat{R}$ being restricted by the presence of a fracture within $\hat{R}$. Figure 13 shows fracture cells ($\check{h}_j$ and $\check{h}_m$) intersecting $\hat{R}$, whose projections on $\bar{F}$ intersects the projection of $\check{k}_i$ on the same face. Rao et al. (2020) proposes that, in this condition, $\check{h}_j$ and $\check{h}_m$ should participate in the calculation of $\mathfrak{T}_{\hat{R},\check{k}_i}$. Thus, the Eq. (4.15) becomes:

$$\mathfrak{T}_{\hat{R},\check{k}_i} = \left[\frac{\tilde{A}^{\bar{F}}_{\hat{L},\check{k}_i}}{\langle d_{\hat{R},\check{k}_i}\rangle}\right]\left[\frac{\left(w_{f_k} + \ell_{\hat{R}} + \frac{V^{\hat{L}}_{\check{k}_i\bar{F}}}{\Omega_{\hat{L}}}\ell_{\hat{L}}\right)K^n_{\hat{L}\check{k}_i}K^n_{\hat{R}\check{k}_i}K_{f_k}}{K^n_{\hat{L}\check{k}_i}K^n_{\hat{R}\check{k}_i}w_{f_k} + K^n_{\hat{L}\check{k}_i}K_{f_k}\ell_{\hat{R}} + \frac{V^{\hat{L}}_{\check{k}_i\bar{F}}}{\Omega_{\hat{L}}}K^n_{\hat{R}\check{k}_i}K_{f_k}\ell_{\hat{L}}}\right] \tag{4.16}$$

with:

$$\tilde{A}^{\bar{F}}_{\hat{L},\check{k}_i} = A^{\bar{F}}_{\hat{L},\check{k}_i} - A\left(\mathrm{P}^{\bar{F}}_{\hat{L},\check{k}_i} \cap \mathrm{P}^{\bar{F}}_{\hat{R},\check{h}_m}\right) - A\left(\mathrm{P}^{\bar{F}}_{\hat{L},\check{k}_i} \cap \mathrm{P}^{\bar{F}}_{\hat{R},\check{h}_j}\right) \tag{4.17}$$

in which $A\left(\mathrm{P}^{\bar{F}}_{\hat{L},\check{k}_i} \cap \mathrm{P}^{\bar{F}}_{\hat{R},\check{h}_m}\right)$ is the area of $\mathrm{P}^{\bar{F}}_{\hat{L},\check{k}_i} \cap \mathrm{P}^{\bar{F}}_{\hat{R},\check{h}_m}$ (analogous to $\check{h}_j$).

Besides, Rao et al. (2020) proposed one more sophistication for pEDFM: the additional transmissibility between two fracture cells intersecting neighboring rock matrix cells. Since the projections of $\check{k}_i$ and $\check{h}_j$ on $\bar{F}$ intersect each other, in Figure 13, there should be an additional transmissibility term between $\check{k}_i$ and $\check{h}_j$. This term can be defined as:

$$\mathfrak{T}_{\check{k}_i,\check{h}_j} = \left[2\frac{A\left(\mathrm{P}^{\bar{F}}_{\hat{L},\check{k}_i} \cap \mathrm{P}^{\bar{F}}_{\hat{R},\check{h}_j}\right)}{\langle d_{\check{k}_i,\check{h}_j}\rangle + \langle d_{\check{h}_j,\check{k}_i}\rangle}\right]\left[\frac{\mathcal{W}_n K^n_{\hat{L}\check{k}_i} K^n_{\hat{R}\check{h}_j} K_{f_k} K_{f_h}}{\mathcal{W}_d}\right] \tag{4.18}$$

in which:

$$\mathcal{W}_n = w_{f_k} + w_{f_h} + \frac{V^{\hat{L}}_{\check{k}_i\bar{F}}}{\Omega_{\hat{L}}}\ell_{\hat{L}} + \frac{V^{\hat{R}}_{\check{h}_j\bar{F}}}{\Omega_{\hat{R}}}\ell_{\hat{R}} \tag{4.19}$$

and:

$$\begin{aligned}\mathcal{W}_d = {} & K^n_{\hat{L}\check{k}_i} K^n_{\hat{R}\check{h}_j} K_{f_h} w_{f_k} + K^n_{\hat{L}\check{k}_i} K^n_{\hat{R}\check{h}_j} K_{f_k} w_{f_h} + \frac{V^{\hat{L}}_{\check{k}_i\bar{F}}}{\Omega_{\hat{L}}} K^n_{\hat{R}\check{h}_j} K_{f_k} K_{f_h} \ell_{\hat{L}} \\ & + \frac{V^{\hat{R}}_{\check{h}_j\bar{F}}}{\Omega_{\hat{R}}} K^n_{\hat{L}\check{k}_i} K_{f_k} K_{f_h} \ell_{\hat{R}}\end{aligned} \tag{4.20}$$

The transmissibility expressions presented from Eq. (4.13) to Eq. (4.16) can be applied on TPFA equations similar to Eq. (3.6) in order to determine the additional pEDFM fluxes through the face $\bar{\mathrm{F}}$ that receive the projections. Besides, the pEDFM flux between $\check{k}_i$ and $\check{h}_j$, for the case shown in Figure 13, can be calculated similarly, using the transmissibility presented in Eq. (4.18), as:

Figure 13 – Intersections between fractures projections on the same face.

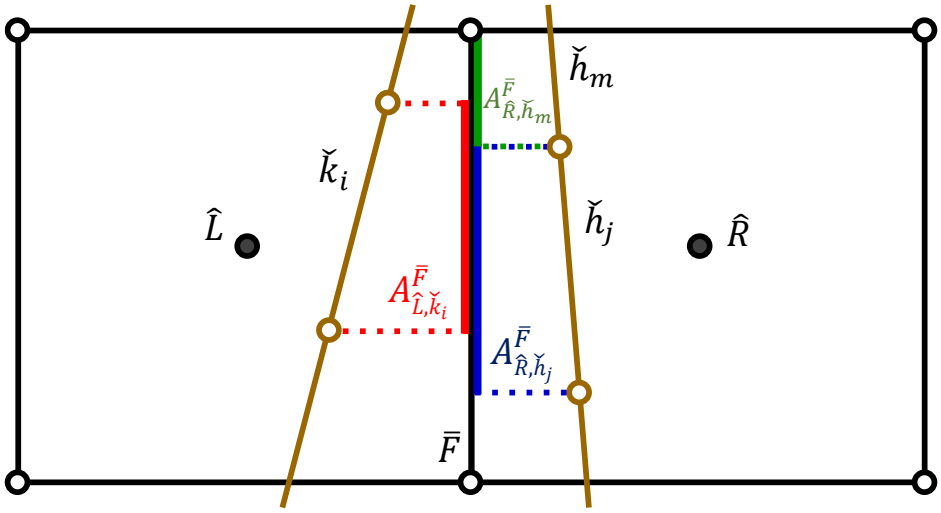

Source: The author (2023).

$$(\rho_\alpha q_\alpha)_{\check{k}_i,\check{h}_j} = -(\rho_\alpha q_\alpha)_{\check{h}_j,\check{k}_i} = -\rho_\alpha \lambda_\alpha \mathfrak{T}_{\check{k}_i,\check{h}_j} \left(p_{\check{h}_j} - p_{\check{k}_i}\right) \tag{4.21}$$

It is necessary, however, to determine if $\bar{F}$ receives or not the projections, from which the development presented in Eq. (4.13) to Eq. (4.20) stems. Ţene et al. (2017), Jiang and Younis (2017) and Rao et al. (2020) indicated different strategies with this objective, but all these selection methods were developed for Cartesian grids. In this work, the followed strategy is that presented by HosseiniMehr et al. (2022) to be applied on corner-point grids: given a face $\bar{F}$, shared by $\hat{L}$ and $\hat{R}$, it will receive the projection of $\check{k}_i \cap \hat{L}$, if Ω_{f_k} intersects the segment connecting the centroids of $\hat{L}$ and $\hat{R}$, as shown in Figure 14. This strategy makes sense for unstructured grids and is capable, as far as known by the tests realized during the development of this work, to lead to continuous sets of projections, what is very important to good performance of pEDFM.

Other important aspect of the pEDFM application is the determination of the remainder area of $\bar{F}$, available to the interaction between $\hat{L}$ and $\hat{R}$ ($A^{pEDFM}_{\hat{L}\hat{R}}$). Since this work focuses on unstructured grids, the approaches proposed, about this issue, by Ţene et al. (2017), Jiang and Younis (2017), Rao et al. (2020) or HosseiniMehr et al. (2022) are not applicable. All these authors considered that $A^{pEDFM}_{\hat{L}\hat{R}}$ can be determined as:

Figure 14 - Intersection between Ω_{f_k} and the segment connecting $\hat{L}$ and $\hat{R}$. The blue region represents the intersection $\check{k}_i \cap \hat{L}$.

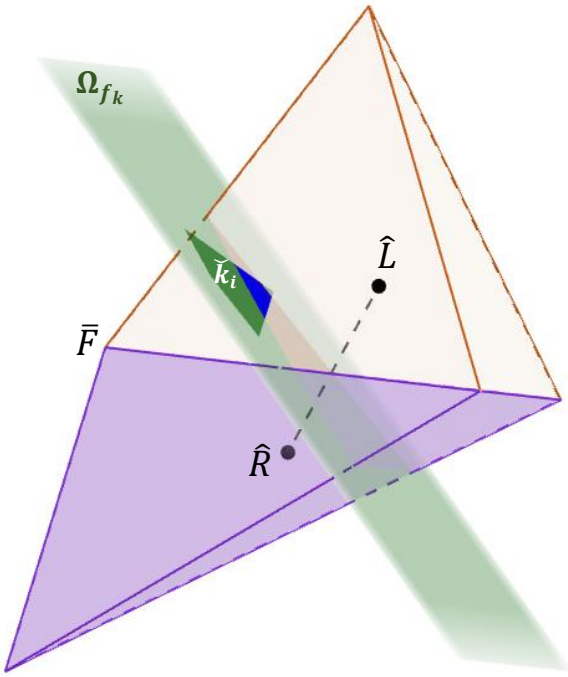

Source: The author (2023).

$$A_{\hat{L}\hat{R}}^{pEDFM} = A_{\bar{F}} - A\left(\bigcup_{k=1}^{n_{frac}}\bigcup_{i=1}^{n_{poly}^{k}} \mathrm{P}_{\hat{L},\check{k}_i}^{\bar{F}} \cup \bigcup_{k=1}^{n_{frac}}\bigcup_{i=1}^{n_{poly}^{k}} \mathrm{P}_{\hat{R},\check{k}_i}^{\bar{F}}\right) \tag{4.22}$$

in which $A_{\bar{F}}$ is the original area of the face $\bar{F}$. Figure 15 shows why this approach is not applicable and the alternative chosen for this work. This figure shows a set of triangle cells, in a 2-D unstructured grid (for didactic purposes), crossed by a fracture Ω_{f_k}. The referred approach creates a discontinuous set of projections, so that the face $\bar{F}$, shared by $\hat{L}$ and $\hat{R}$, is not completely covered by the projection of $\hat{L} \cap \Omega_{f_k}$ (see Figure 15a). This way, there would be an unexpected interaction between $\hat{L}$ and $\hat{R}$. Figure 15b shows how the set of projections ideally should be in this case, but it is extremely difficult to operationalize this construction when dealing with unstructured meshes in 3-D. By simplicity, in this work, it is considered that if Ω_{f_k} intersects the segment connecting the

centroids of two cells sharing a face, the interaction between these two grid elements ($\hat{L}$ and $\hat{R}$) through that face is completely cancelled, as shown in Figure 15c.

Figure 15 - Set of fractures projections on grid faces. (a) Faces projections, creating a discontinuous set. Circles highlighting discontinuities. (b) Ideal set of projections for this case. (c) Set of projections as done in this work. Circles highlighting the complete coverage of the faces by the projections.

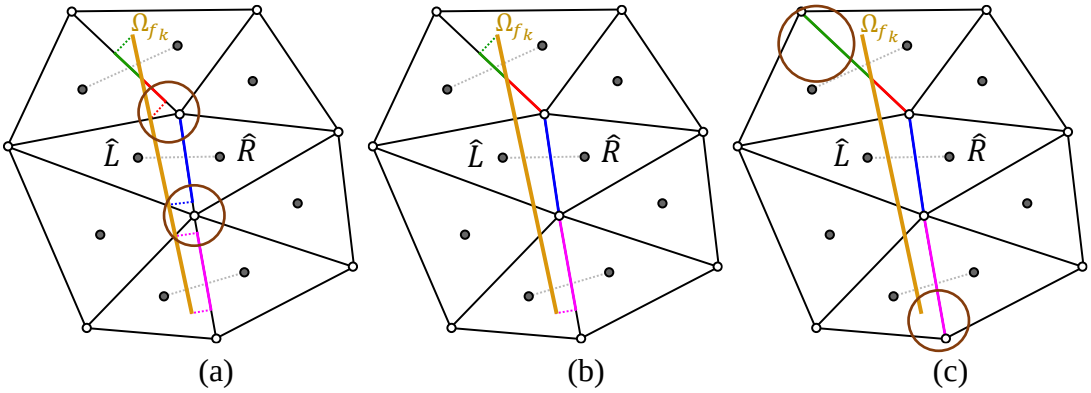

Source: The author (2023).

This strategy is notably over conservative and introduces errors (excessive interactions cancellation) in the regions coinciding with the limits of the fractures. On the other hand, it is a simple way to guarantee the absence of unexpected interactions between cells through all the area of the fracture.

There are other relevant simplifications in the pEDFM model applied in this work. First, the transmissibility expressions presented from Eq. (4.14) to Eq. (4.16) are not considered, so that the matrix-fracture pEDFM interactions are calculated here according to Eq. (4.13). The implementation and testing of those more sophisticated transmissibility terms remains as further works. Moreover, the additional transmissibility between two fracture cells intersecting neighboring rock matrix cells proposed by Rao et al. (2020), to be calculated according to Eq. (4.18) to Eq. (4.20), are also not considered in this work.

Similarly, if, for example, the fracture cell $\check{k}_i$ intersects the segment connecting the centroids of two fracture cells ($\check{h}_j$ and $\check{h}_m$), as shown in Figure 16, the communication

between $\check{h}_j$ and $\check{h}_m$ could also be blocked, while $\check{k}_i$ interacts with $\check{h}_j$ according to Eq. (4.11).

Figure 16 – Intersection between fractures in the context of pEDFM.

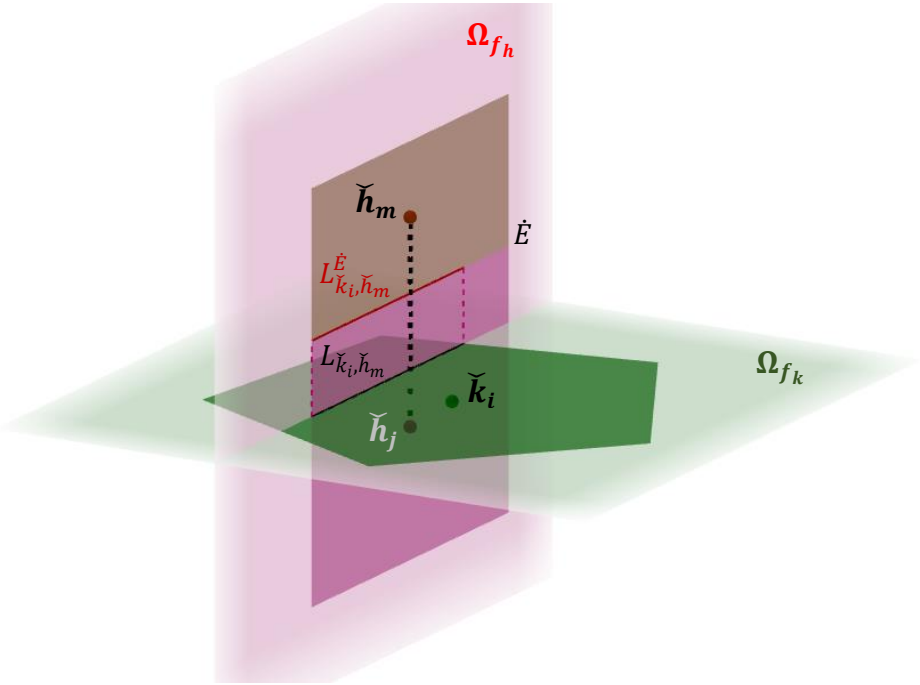

Source: The author (2023).

Besides, the projection of $\check{k}_i \cap \check{h}_j$ on the edge $\dot{E}$, shared by $\check{h}_j$ and $\check{h}_m$, would cause an additional interaction between $\check{k}_i$ and $\check{h}_m$. However, these fracture-fracture pEDFM interactions are also not considered in this work, in order to avoid the interruption of the flow through a high permeability fracture crossed by a barrier. In this work, the channels (i.e., high permeability fractures) always overcome the barriers (i.e., low permeability fractures) when they cross. Ideally, the user of the simulator could choose, at each intersection, which of the fractures would prevail, but, in the present work, we have chosen to avoid the fracture-fracture pEDFM interactions to ensure the prevalence of channels over barriers.

Figure 17 summarizes, in a 2-D unstructured grid (for didactic reasons, but it is analogous to 3-D), all the interactions between two rock matrix cells ($\hat{L}$ and $\hat{R}$) sharing a face ($\bar{F}$) and a fracture Ω_{f_h} intersecting them, while the communication between $\hat{L}$ and $\hat{R}$

themselves is cancelled. It is also useful, together with Figure 18, to review all the numerical formulation applied in this work in the context of EDFM and pEDFM.

Figure 17 - Summary of EDFM and pEDFM interactions in a 2-D unstructured grid.

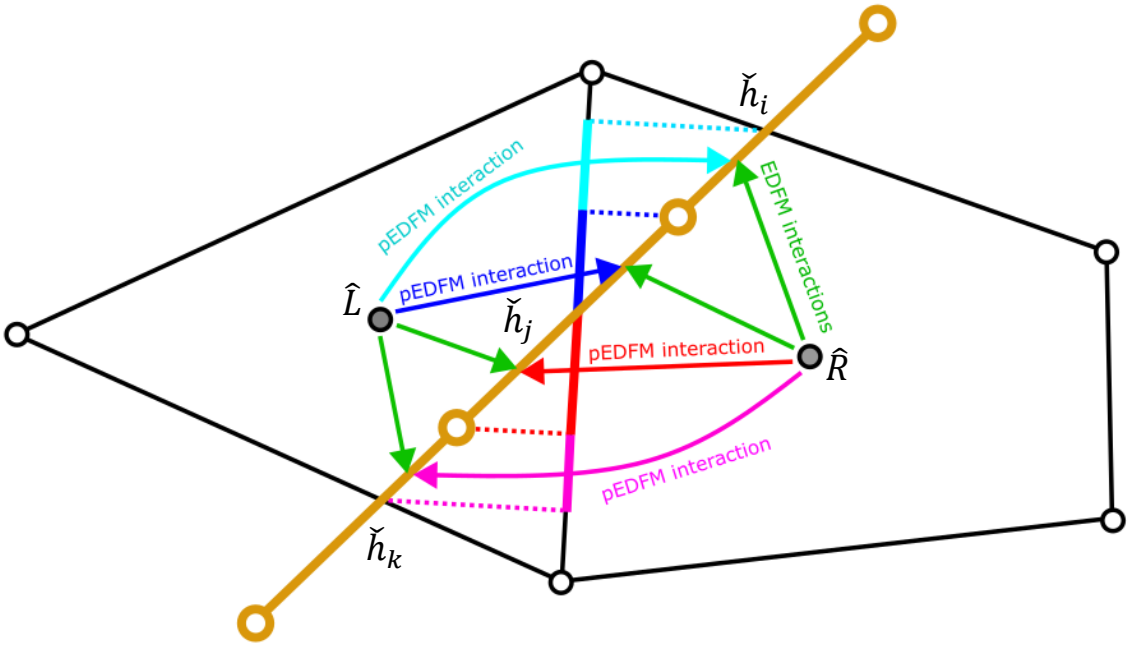

Source: The author (2023).

Figure 17 indicates the EDFM interactions between each rock matrix cell ($\hat{L}$ or $\hat{R}$) and the fractures cells intersecting it, according to the development shown in section 4.2. The interactions between fracture cells are also obtained according to section 4.2, considering only EDFM (see Figure 18). Moreover, the blue arrow, for example, shows that there is a pEDFM connection between $\hat{L}$ and the fracture cell $\check{h}_j$, in addition to the one that already existed due to EDFM (see Figure 18), through the projection on $\bar{F}$ of the part of $\check{h}_j$ within $\hat{R}$. This additional pEDFM interaction is computed using the transmissibility presented in Eq. (4.13).

In the same way, there are additional pEDFM interactions between $\hat{L}$ and $\check{h}_i$, between $\hat{R}$ and $\check{h}_j$, and between $\hat{R}$ and $\check{h}_k$, also to be calculated using the transmissibility of Eq. (4.13). Note that between $\hat{L}$ and $\check{h}_i$ and between $\hat{R}$ and $\check{h}_k$ there is not any EDFM connections, since there are not intersections between them.

All these mentioned interactions will give rise to flux calculations, as shown in Eq. (3.6), Eq. (4.10) and Eq. (4.11) (see Figure 18), that are used in Eqs. (3.11) and (3.12) and compose the global system of equations that will describe the fluid flow we pretend to simulate.

Figure 18 - Summary of transmissibility calculations used in this work, in the context of matrix-fracture and fracture-fracture interactions.

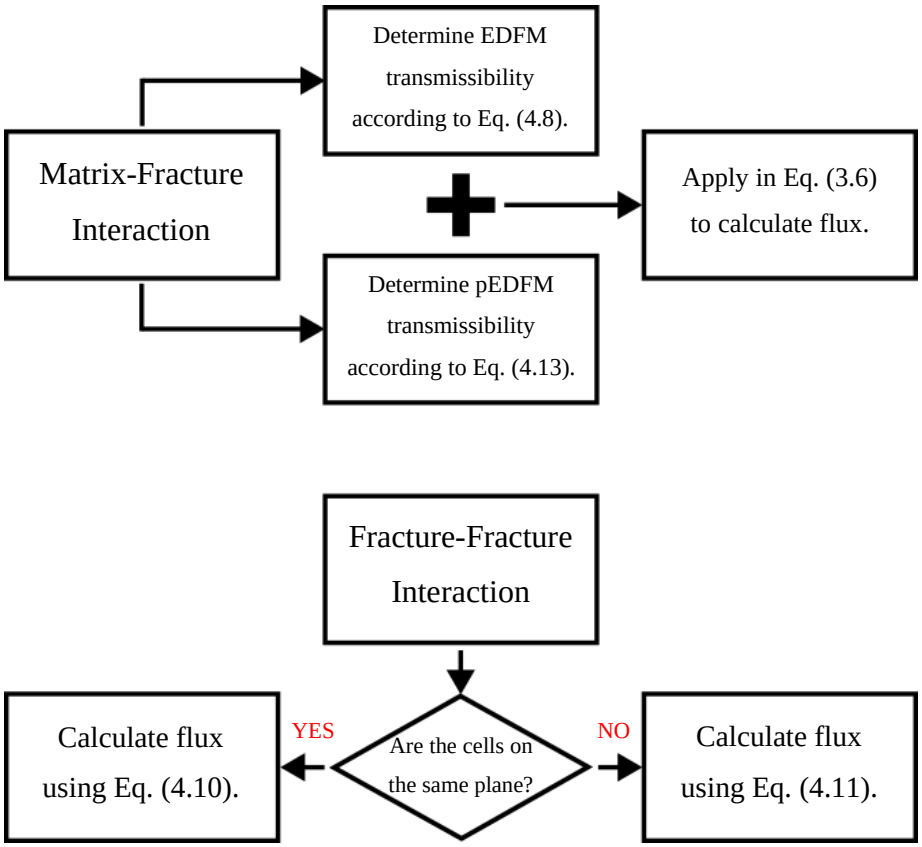

Source: The author (2023).

5 APPLICATIONS

This section presents some applications of the numerical schemes presented in this thesis, in order to demonstrate their robustness in dealing with some interesting problems. The first subsection presents some tests about MPFA-D, as well as the comparison of the different interpolation strategies studied here. The second subsection presents a demonstration of effectiveness of MPFA-DNL, the third subsection presents one benchmark test of single-phase flow in fractured media and, finally, the last subsection presents the tests about immiscible two-phase flow in anisotropic porous media, illustrating the application of pEDFM on tetrahedral unstructured grids.

MPFA-D, MPFA-DNL, as well as all their requirements in terms of preprocessing or postprocessing, were implemented by the author in MATLAB® (an environment that allows easy prototyping and have wide library of functions), in the PADMEC researching group of UFPE. The framework of DARSim software (HOSSEINIMEHR et al., 2022) was used to perform simulations of immiscible two-phase flow. It was originally developed, at TUDelft, for Cartesian and corner-point grids and was adapted to make it capable of applying pEDFM on tetrahedral meshes, according to what was presented in section 4. The mesh generation, for the discretization of the domain, was made by using the free software GMSH (GEUZAINE; REMACLE, 2009). The visualization of the resulting pressure and saturation fields was made by using VisIt® (CHILDS et al., 2012) and some graphs were made by using MATLAB®.

5.1 MPFA-D FOR TETRAHEDRAL UNSTRUCTURED GRIDS

This subsection is not in the context of fractured reservoirs, but it presents some application of the developed MPFA-D (LIRA FILHO et al., 2021) in solving some benchmark problems, in the context of unstructured tetrahedral grids, including the comparison of the interpolation strategies presented here: LPEW1, LPEW2, LPEW3, LPEW-WAP and GLS. The gravity effects are not considered.

It is convenient to define some parameters to be used in the following analysis. Considering that the exact solution is given by $\mathcal{p}$ and the approximate solution is represented by p, we can define the relative L-2 norm of error for the pressure (EYMARD et al., 2011; LIRA FILHO et al., 2021) as:

$$\ell_p^2 = \sqrt{\frac{\sum_{i=1}^{n_{tetra}} (\mathcal{p}_i - p_i)^2 \Omega_i}{\sum_{i=1}^{n_{tetra}} \mathcal{p}_i{}^2 \Omega_i}} \tag{5.1}$$

and for its gradient ∇p as:

$$\ell_{\nabla p}^2 = \sqrt{\frac{\sum_{i=1}^{n_{tetra}} |\nabla \mathcal{p}_i - \nabla p_i|^2 \Omega_i}{\sum_{i=1}^{n_{tetra}} |\nabla \mathcal{p}_i|^2 \Omega_i}} \tag{5.2}$$

for which the numerical convergence rate is given by (EYMARD et al., 2011):

$$\mathcal{R}_\mathfrak{z} = -3 \frac{log\left(\frac{\ell_{\mathfrak{z},m}^2}{\ell_{\mathfrak{z},m-1}^2}\right)}{log\left(\frac{n_{tetra}^m}{n_{tetra}^{m-1}}\right)} \tag{5.3}$$

for two successive meshes[1] ($m-1$ and m), with $m > 1$ and $\mathfrak{z} = p, \nabla p$.

5.1.1 Oblique Fracture

This example is based on the benchmark tests 6 and 7 from Herbin and Hubert (2008). Consider a domain $\Omega_m = [0,1]^3$ with a diagonal fracture Ω_f dimensionally represented, in this example, as a 3-D entity (this is not an EDFM or pEDFM application). Ω_m is divided in two parts (Ω_{m1} and Ω_{m2}) separated by Ω_f, so that the geometrical definition of the whole problem is:

$$\begin{cases} \Omega_{m1} = \{(x,y,z) \in \Omega_m; \phi_1(x,y,z) < 0\} \\ \Omega_f = \{(x,y,z); \phi_1(x,y,z) > 0, \phi_2(x,y,z) < 0\} \\ \Omega_{m2} = \{(x,y,z) \in \Omega_m; \phi_2(x,y,z) > 0\} \end{cases} \tag{5.4}$$

with $\phi_1(x,y,z) = y - \delta(x - 0.5) - 0.475$ and $\phi_2(x,y,z) = \phi_1(x,y,z) - 0.05$, with the slope of the fracture being $\delta = 0.2$. The Neumann boundary conditions (Γ_m^N and Γ_f^N) are defined at $y = 0$ and $y = 1$ with the prescribed value $g_N = 0$. The rest of the

[1] The meshes used in this work can be found at the following address: https://github.com/tuliocavalcante/mesh

boundary is considered as Dirichlet boundaries (Γ_m^D and Γ_f^D). Beyond this, two cases are defined.

5.1.1.1 Drain Case

In this case, there is a plane solution (implying in the Dirichlet boundary conditions) given by:

$$\wp_1(x, y, z) = -x - \delta y \tag{5.5}$$

with an anisotropic diffusion tensor defined as:

$$\mathbf{K}_1 = R_\theta \begin{bmatrix} \alpha & 0 & 0 \\ 0 & \beta & 0 \\ 0 & 0 & 1 \end{bmatrix} R_\theta^T \tag{5.6}$$

with $\theta = \operatorname{atan} \delta$ and R_θ being the rotation matrix in the z axis, defined as:

$$R_\theta = \begin{bmatrix} \cos\theta & -\sin\theta & 0 \\ \sin\theta & \cos\theta & 0 \\ 0 & 0 & 1 \end{bmatrix} \tag{5.7}$$

and with α and β, to be applied in Eq. (5.6), being defined as:

$$\begin{pmatrix} \alpha \\ \beta \end{pmatrix} = \begin{pmatrix} 10^2 \\ 10 \end{pmatrix} \text{ in } \Omega_f \text{ and } \begin{pmatrix} \alpha \\ \beta \end{pmatrix} = \begin{pmatrix} 1 \\ 10^{-1} \end{pmatrix} \text{ in } \Omega_{m1} \cup \Omega_{m2} \tag{5.8}$$

5.1.1.2 Barrier Case

In this case, there is a piecewise plane solution (implying in the Dirichlet boundary conditions) given by:

$$\wp_2(x, y, z) = \begin{cases} -\phi_1(x, y, z) \text{ on } \Omega_{m1} \\ -\phi_1(x, y, z)/10^{-2} \text{ on } \Omega_f \\ -\phi_3(x, y, z) \text{ on } \Omega_{m2} \end{cases} \tag{5.9}$$

with $\phi_3(x,y,z) = y - \delta(x - 0.5) + 0.02$ and with a diffusion tensor defined as:

$$\mathbf{K}_2 = \begin{bmatrix} \alpha & 0 & 0 \\ 0 & \alpha & 0 \\ 0 & 0 & 1 \end{bmatrix} \tag{5.10}$$

in which $\alpha = 10^{-2}$ in Ω_f and $\alpha = 1$ in $\Omega_{m1} \cup \Omega_{m2}$.

5.1.1.3 Results

This test was used to prove the linearity-preserving characteristic (that should be called "planicity preserving", in 3-D) of the interpolation strategies studied here, namely: LPEW1, LPEW2, LPEW3 (LIRA FILHO et al., 2021), LPEW-HAP (YANG; GAO, 2020) and GLS (DONG; KANG, 2021, 2022). The L-2 norm of error of the pressure (ℓ_p^2) of these two cases (high permeability fracture and low permeability fracture) are presented in Table 1, which shows that all the evaluated methods are capable to recover the exact piecewise plane continuous solutions, as those in cases 5.1.1.1 and 5.1.1.2.

Table 1 - The L-2 norm of error of the pressure for the test 5.1.1 - Oblique Fracture.

		ℓ_p^2				
Case	n_{tetra}	LPEW1	LPEW2	LPEW3	LPEW-HAP	GLS
5.1.1.1	30	5.75e-11	5.91e-12	5.75e-12	2.21e-14	5.04e-14
5.1.1.2	30	6.48e-13	1.44e-12	2.29e-12	3.62e-16	2.44e-16

Source: The author (2023).

5.1.2 Homogeneous and Mild Anisotropic Media

This is the test 6 of the work of c with a regular solution over the domain $\Omega_m = [0,1]^3$, that implies in a non-homogeneous Dirichlet boundary condition, defined as:

$$p(x,y,z) = 1 + \sin(\pi x)\sin\left[\pi\left(y + \frac{1}{2}\right)\right]\sin\left[\pi\left(z + \frac{1}{3}\right)\right] \tag{5.11}$$

with an anisotropic diffusion tensor defined as:

$$\mathbf{K} = \begin{bmatrix} 1.5 & 0.5 & 0 \\ 0.5 & 1.5 & 0.5 \\ 0 & 0.5 & 1 \end{bmatrix} \tag{5.12}$$

and with a source term computed according to:

$$q(x, y, z) = -\mathbf{K}\nabla p(x, y, z) \tag{5.13}$$

This test was used to compare the convergence behavior of the interpolation strategies studied here. The results presented in Table 2 shows that LPEW1 achieve second order of accuracy for pressure (Figure 19a) and first order of accuracy for fluxes (Figure 19b), as expected. Note that the LPEW1 convergence rate for the flux is bigger than 1, in this example, for all the tested meshes.

Table 2 - Results for the test 5.1.2 - Homogeneous and Mild Anisotropic Media. The "unexpected" results, in terms of convergence rates, are highlighted in red.

	LPEW1				LPEW-HAP			
n_{tetra}	ℓ_p^2	$\mathcal{R}_p$	$\ell_{\nabla p}^2$	$\mathcal{R}_{\nabla p}$	ℓ_p^2	$\mathcal{R}_p$	$\ell_{\nabla p}^2$	$\mathcal{R}_{\nabla p}$
215	0.052	-	0.587	-	0.056	-	0.719	-
2,003	0.013	1.838	0.267	1.059	0.043	0.363	1.380	-0.877
3,898	0.008	2.055	0.206	1.173	0.065	-1.909	2.585	-2.826
7,711	0.005	2.037	0.163	1.028	0.008	9.133	0.375	8.486
15,266	0.004	1.682	0.129	1.043	0.027	-5.305	1.956	-7.251
30,480	0.002	2.174	0.101	1.050	0.016	2.378	1.378	1.520
61,052	0.001	1.749	0.079	1.073	0.052	-5.094	5.721	-6.149

Source: The author (2023).

The results obtained by LPEW2, LPEW3 and GLS are almost coincident with those from LPEW1, as shown in Figure 19. The results from LPEW-HAP (shown in Table 2 and Figure 19), however, indicate that its convergence depends on the mesh. It

converges if applied to “regular” meshes, as those used by Yang and Gao (2020), but not necessarily when applied to “truly unstructured” meshes, as those here used, got from the benchmark work of Eymard et al. (2011). Because of this, LPEW-HAP has been discarded, in this work, as interpolation strategy, when simulating two-phase flow in fractured porous media, using tetrahedral unstructured grids.

Figure 19 – Convergence graphs for the test 5.1.2 - Homogeneous and Mild Anisotropic Media.

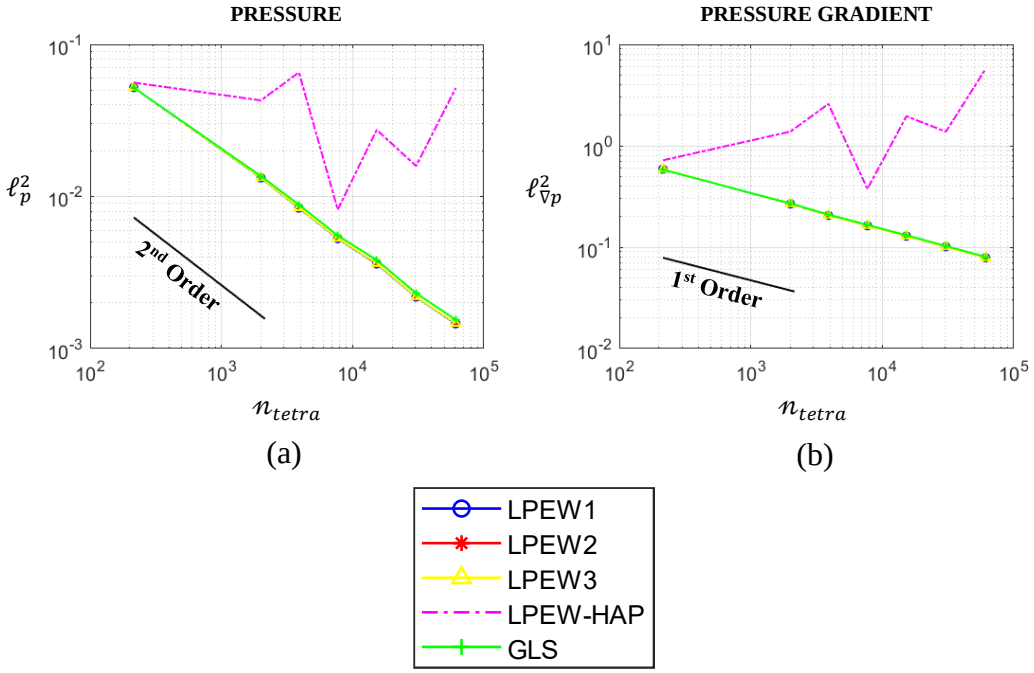

Source: The author (2023).

5.1.3 Heterogeneous and Anisotropic Media

This is the benchmark test case 2 from Eymard et al. (2011) with a regular solution, over the domain $\Omega_m = [0,1]^3$, that implies in a non-homogeneous Dirichlet boundary condition, defined as:

$$p(x, y, z) = x^3 y^2 z + x \sin(2\pi xz) \sin(2\pi xy) \sin(2\pi z) \tag{5.14}$$

with an anisotropic and heterogeneous diffusion tensor defined as:

$$\mathbf{K}(x,y,z) = \begin{bmatrix} y^2+z^2+1 & -xy & -xz \\ -xy & x^2+z^2+1 & -yz \\ -xz & -yz & x^2+y^2+1 \end{bmatrix} \tag{5.15}$$

The source term is calculated similarly to Eq. (5.13). Table 3 presents the comparison between the results of LPEW3 and GLS, which are almost coincident, in the same way that those from LPEW1 and LPEW2, achieving second order of accuracy for pressure (Figure 20a) and first order of accuracy for fluxes (Figure 20b). Again, the LPEW-HAP was not capable to ensure the convergence, reinforcing the decision, affirmed in the previous example, not to use it in the simulations using unstructured grids.

Table 3 - Results for the test 5.1.3 - Heterogeneous and Anisotropic Media.

	LPEW3				GLS			
n_{tetra}	ℓ_p^2	$\mathcal{R}_p$	$\ell_{\nabla p}^2$	$\mathcal{R}_{\nabla p}$	ℓ_p^2	$\mathcal{R}_p$	$\ell_{\nabla p}^2$	$\mathcal{R}_{\nabla p}$
215	0.506	-	0.980	-	0.509	-	0.985	-
2,003	0.128	1.848	0.535	0.813	0.132	1.817	0.548	0.789
3,898	0.083	1.945	0.448	0.802	0.086	1.910	0.458	0.808
7,711	0.061	1.367	0.358	0.986	0.064	1.307	0.370	0.938
15,266	0.038	2.104	0.283	1.027	0.040	2.038	0.293	1.017
30,480	0.024	1.915	0.228	0.951	0.026	1.852	0.235	0.960
61,052	0.017	1.654	0.180	1.004	0.018	1.681	0.186	1.001

Source: The author (2023).

5.1.4 Homogeneous and Highly Anisotropic Media

This is the benchmark test case 3 from Eymard et al. (2011) with an analytic solution, over the domain $\Omega_m = [0,1]^3$, that implies in a non-homogeneous Dirichlet boundary condition, defined as:

$$p(x,y,z) = \sin(2\pi x)\sin(2\pi y)\sin(2\pi z) \tag{5.16}$$

Figure 20 – Convergence graphs for the test 5.1.3 - Heterogeneous and Anisotropic Media.

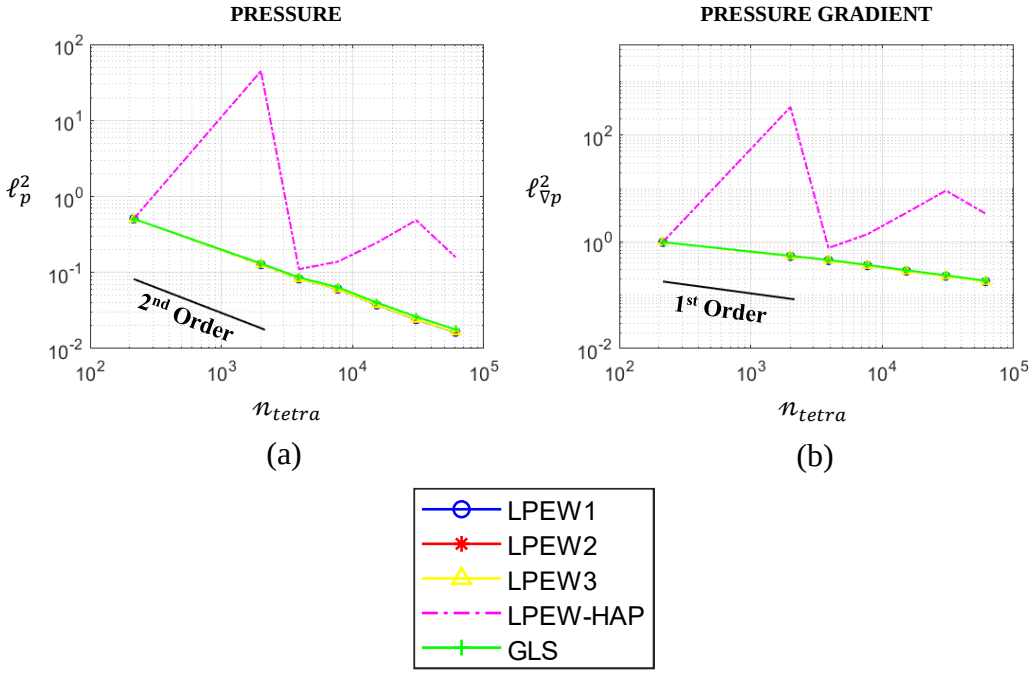

Source: The author (2023).

with a highly anisotropic diffusion tensor defined as:

$$\mathbf{K} = \begin{bmatrix} 1 & 0 & 0 \\ 0 & 1 & 0 \\ 0 & 0 & 1{,}000 \end{bmatrix} \tag{5.17}$$

and with a source term computed according to Eq. (5.13).

This test was also used to compare the convergence behavior of the interpolation strategies studied here. The results presented in Table 4 shows that GLS achieve second order accuracy for pressure and first order accuracy for fluxes, as expected. In this case, however, LPEW1, LPEW2 and LPEW3 were unsuccessful in guarantee the convergence, as presented in Figure 21. Table 4 also shows the results of LPEW2, demonstrating the inability of the authorial interpolation methods to handle strongly anisotropic tensors. Because of this, LPEW1, LPEW2 and LPEW3 have been discarded, in this work, as interpolation strategy, when simulating two-phase flow in fractured porous media.

Table 4 - Results for the test 5.1.4 - Homogeneous and Highly Anisotropic Media. The "unexpected" results, in terms of convergence rates, are highlighted in red.

	GLS				LPEW2			
n_{tetra}	ℓ_p^2	$\mathcal{R}_p$	$\ell_{\nabla p}^2$	$\mathcal{R}_{\nabla p}$	ℓ_p^2	$\mathcal{R}_p$	$\ell_{\nabla p}^2$	$\mathcal{R}_{\nabla p}$
215	1.066	-	1.060	-	1.090	-	1.139	-
2,003	0.244	1.983	0.502	1.005	11.244	-3.137	20.725	-3.900
3,898	0.160	1.897	0.423	0.776	0.979	11.000	2.108	10.299
7,711	0.106	1.821	0.334	1.035	1.227	-0.995	3.362	-2.054
15,266	0.066	2.095	0.271	0.911	1.183	0.159	3.793	-0.530
30,480	0.042	1.930	0.216	1.001	1.853	-1.947	7.316	-2.850
61,052	0.027	1.979	0.171	0.991	2.773	-1.740	12.646	-2.364

Source: The author (2023).

Figure 21 – Convergence graphs for the test 5.1.4 - Homogeneous and Highly Anisotropic Media.

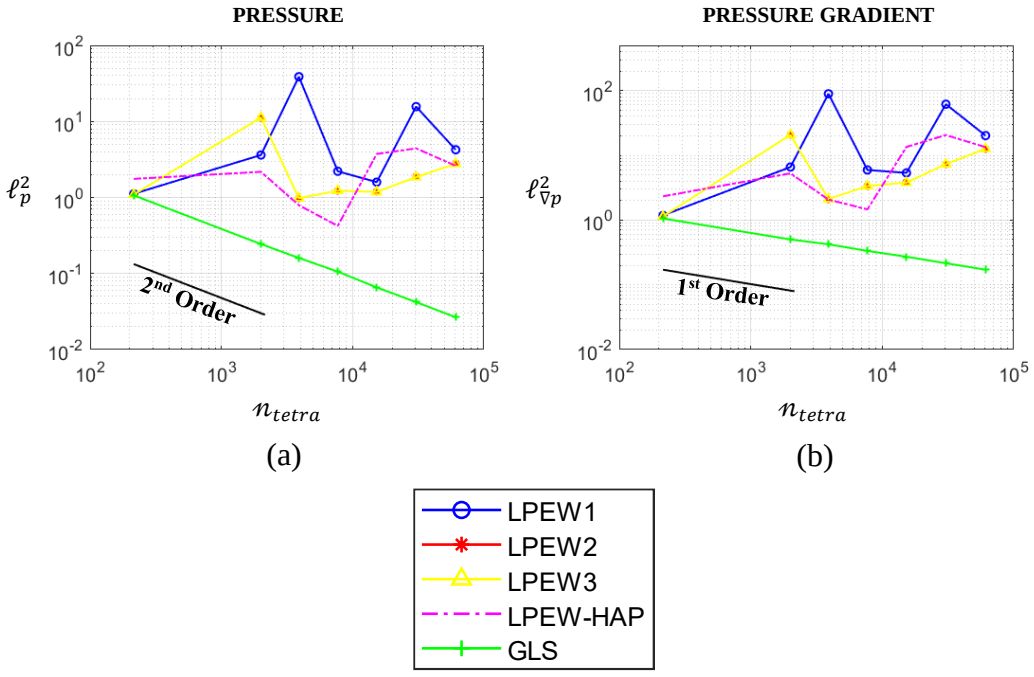

Source: The author (2023).

5.1.5 Four Anisotropic Regions

This is the benchmark test case 5 from Eymard et al. (2011) with a domain $\Omega_m = [0,1]^3$ divided into four subdomains $\Omega_m = \cup_{i=1}^{4} \Omega_i$:

$$\begin{cases} \Omega_1 = \{(x,y,z) \in [0,1]^3 \; such \; that \; y \leq 0.5, z \leq 0.5\} \\ \Omega_2 = \{(x,y,z) \in [0,1]^3 \; such \; that \; y > 0.5, z \leq 0.5\} \\ \Omega_3 = \{(x,y,z) \in [0,1]^3 \; such \; that \; y > 0.5, z > 0.5\} \\ \Omega_4 = \{(x,y,z) \in [0,1]^3 \; such \; that \; y \leq 0.5, z > 0.5\} \end{cases} \tag{5.18}$$

and with an analytic solution, that implies in a non-homogeneous Dirichlet boundary condition, defined as:

$$\wp(x,y,z) = \alpha_i sin(2\pi x) \; sin(2\pi y) \; sin(2\pi z) \tag{5.19}$$

with a diagonal-anisotropic diffusion tensor defined as:

$$\mathbf{K}_i = \begin{bmatrix} \beta_x^i & 0 & 0 \\ 0 & \beta_y^i & 0 \\ 0 & 0 & \beta_z^i \end{bmatrix} \tag{5.20}$$

with the parameters α_i, β_x^i, β_y^i and β_z^i being defined according to Table 5, in which i is the region index.

Table 5 – Parameters for configuration of test 5.1.5 - Four Anisotropic Regions.

i	1	2	3	4
β_x^i	1	1	1	1
β_y^i	10	0.1	0.01	100
β_z^i	0.01	100	10	0.1
α_i	0.1	10	100	0.01

Source: The author (2023).

and with a source term computed according to Eq. (5.13).

In this example, GLS showed again to be the most robust tested interpolation, ensuring convergence even solving this hard problem, including achieving higher convergence rates, as presented in the Table 6.

Table 6 - Results for the test 5.1.5 - Four Anisotropic Regions. The “unexpected” results, in terms of convergence rates, are highlighted in red.

	LPEW2				GLS			
n_{tetra}	ℓ_p^2	$\mathcal{R}_p$	$\ell_{\nabla p}^2$	$\mathcal{R}_{\nabla p}$	ℓ_p^2	$\mathcal{R}_p$	$\ell_{\nabla p}^2$	$\mathcal{R}_{\nabla p}$
1,615	1.902	-	2.581	-	0.575	-	0.836	-
2,896	0.628	5.694	1.591	2.487	0.237	4.555	0.521	2.430
6,044	1.115	-2.343	2.848	-2.375	0.105	3.336	0.342	1.713
11,868	4.930	-6.608	14.710	-7.300	0.077	1.333	0.293	0.694
33,768	0.448	6.881	1.873	5.913	0.029	2.845	0.190	1.242
72,461	2.359	-6.527	11.491	-7.128	0.020	1.449	0.150	0.935

Source: The author (2023).

Figure 22 – Convergence graphs for the test 5.1.5 - Four Anisotropic Regions.

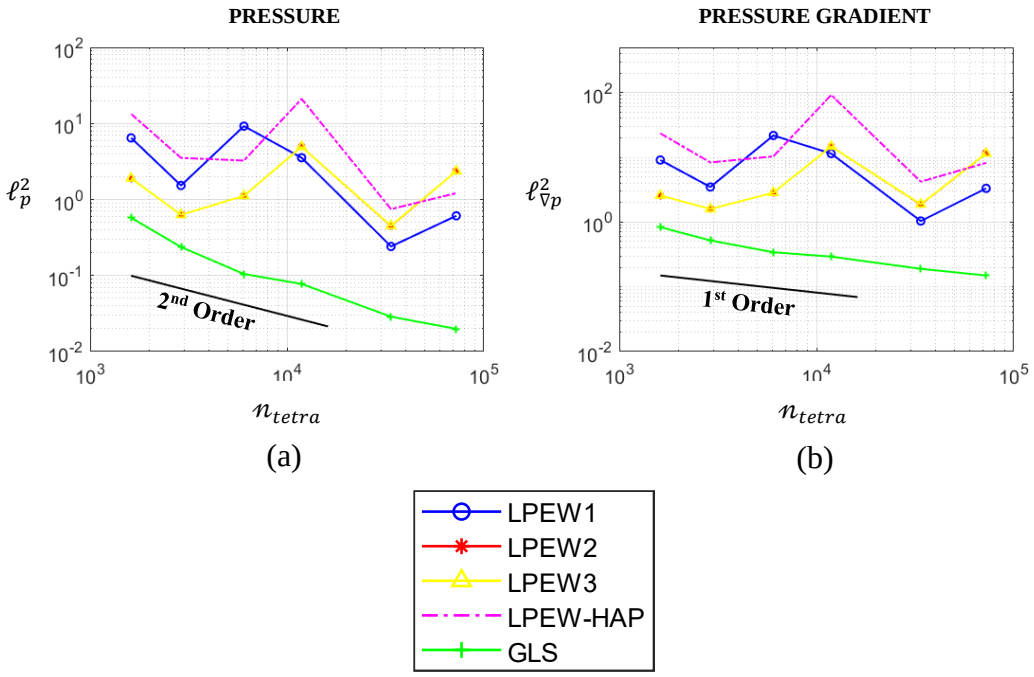

(a) (b)

Source: The author (2023).

LPEW1, LPEW2, LPEW3 and LPEW-HAP could not guarantee convergence in this case, as shown in Figure 22. Table 6 also shows the unsuccessful results of LPEW2. These results confirm the decision to use the GLS interpolation strategy in the context of simulation of two-phase flow in fractured porous media, using tetrahedral unstructured grids, that is the final objective of this work.

5.2 MPFA-DNL

This subsection analysis is still not in the context of fractured reservoirs, but it demonstrates the effectiveness of MPFA-DNL (CAVALCANTE et al., 2022) in context of avoiding the DMP violation commonly observed in applications of any linear formulation, including the linear MPFA family of methods. Beyond the parameters defined by Eq. (5.1) to Eq. (5.11), is also necessary for the following analysis to define the undershoot and overshoot norm of the error as (QUEIROZ et al., 2014):

$$\varepsilon_m = \sqrt{\sum_{i=1}^{n_{tetra}} [\max{}^2(0, p_i - \wp_{\max}) + \max{}^2(0, \wp_{\min} - p_i)]\, \Omega_i} \tag{5.21}$$

where $\wp_{\max}$ and $\wp_{\min}$ are, respectively, the maximum and the minimum values for the solution defined by the boundary conditions. The gravity effects are not considered.

All the tested interpolations may lead to DMP violation, depending on the problem configuration, but, since GLS interpolation was the most successful in the previous tests, it was the applied strategy in this subsection.

5.2.1 Heterogeneous Diagonal-Anisotropic Media

This example was proposed by Cavalcante et al. (2022) to show that the MPFA-DNL corrects the DMP violation without degrading the numerical convergence rate of the MPFA-D. It is a one-phase flow problem which has an analytic solution, on pressure, over the domain $\Omega_m = [0,1]^3$, that implies in a non-homogeneous Dirichlet boundary condition, defined as:

$$\wp(x, y, z) = x(1-x)y(1-y)z(1-z) \tag{5.22}$$

with an anisotropic diffusion tensor given by:

$$\mathbf{K}(x,y,z) = \begin{bmatrix} x+1 & 0 & 0 \\ 0 & y+1 & 0 \\ 0 & 0 & 10(z+1) \end{bmatrix} \tag{5.23}$$

and with a source term computed similarly to Eq. (5.13). Thus, in this case, the expected minimum pressure is $p_{min} = 0$.

In Tables Table 7 and Table 8, we can see the comparison between some results obtained with the MPFA-DNL and with the MPFA-D in its original (non-iterative) version. Table 7 shows how the MPFA-DNL succeeds in avoiding the undershoots observed when using the MPFA-D, what is reinforced by the norm ε_m.

Table 7 - Results for the test 5.2.1 - Heterogeneous Diagonal-Anisotropic Media. The "unexpected" results are highlighted in red.

	MPFA-D		MPFA-DNL	
n_{tetra}	p_{min}	ε_m	p_{min}	ε_m
215	3.76e-4	0	3.76e-4	0
2,003	2.29e-5	0	2.29e-5	0
3,898	-6.84e-5	1.52e-6	3.03e-6	0
7,711	-3.45e-5	5.68e-7	7.95e-7	0
15,266	-4.98e-5	4.86e-7	1.00e-6	0
30,480	-5.02e-5	4.01e-7	0	0

Source: The author (2023).

Table 8 and Figure 23, show that, despite the modifications performed by the non-linear defect correction approach on the original MPFA-D matrix, aiming to avoid the DMP violation, the convergence rates on pressure (Figure 23a) and on pressure gradient (Figure 23b) of our the MPFA-DNL method are not degraded. In fact, for certain meshes, the errors on pressure were slightly smaller for the MPFA-DNL when compared to the original linear MPFA-D method.

Table 8 - Results for the test 5.2.1 - Heterogeneous Diagonal-Anisotropic Media.

	MPFA-D				MPFA-DNL			
n_{tetra}	ℓ_p^2	$\mathcal{R}_p$	$\ell_{\nabla p}^2$	$\mathcal{R}_{\nabla p}$	ℓ_p^2	$\mathcal{R}_p$	$\ell_{\nabla p}^2$	$\mathcal{R}_{\nabla p}$
215	0.207	-	0.568	-	0.206	-	0.568	-
2,003	0.039	2.246	0.271	0.997	0.037	2.291	0.271	0.997
3,898	0.024	2.161	0.223	0.877	0.022	2.335	0.223	0.877
7,711	0.015	2.172	0.168	1.248	0.013	2.486	0.168	1.246
15,266	0.010	1.911	0.136	0.933	0.008	2.264	0.136	0.932
30,480	0.006	2.173	0.108	1.007	0.005	1.698	0.108	1.003

Source: The author (2023).

Figure 23 - The mesh convergence graphs for the test 5.2.1 - Heterogeneous Diagonal-Anisotropic Media.

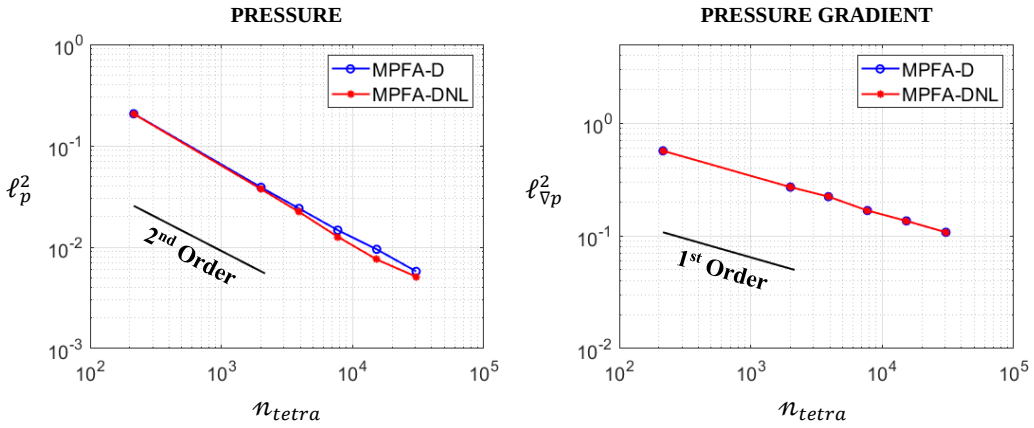

(a) (b)

Source: The author (2023).

In terms of computational cost, for the mesh with 3,898 tetrahedra (the coarsest tested mesh with DMP violation by MPFA-D), MPFA-DNL needed 315 iteration steps to find the solution without spurious oscillations, while, for the mesh with 30,480 tetrahedra (the most refined tested mesh), 836 iterations were necessary.

5.2.2 Anisotropic Hollow Domain

This example was proposed by Danilov and Vassilevski (2009). In this problem, there is a cubic domain $\Omega_c = [0,1]^3$ with a central cubic hole $\Omega_h = [0.4,0.6]^3$, so that the domain of interest is $\Omega_m = \Omega_c - \Omega_h$. At the external boundary $\partial\Omega_c$, the scalar variable is set as $p_e = 0$ and, at the internal face $\partial\Omega_h$, the scalar variable is set as $p_i = 2$. The anisotropic diffusion tensor is defined as:

$$\mathbf{K} = R_z^T R_y^T R_x^T \begin{bmatrix} 100 & 0 & 0 \\ 0 & 10 & 0 \\ 0 & 0 & 1 \end{bmatrix} R_x R_y R_z \tag{5.24}$$

where:

$$R_x = \begin{bmatrix} 1 & 0 & 0 \\ 0 & \cos\theta & -\sin\theta \\ 0 & \sin\theta & \cos\theta \end{bmatrix}; \; R_y = \begin{bmatrix} \cos\beta & 0 & \sin\beta \\ 0 & 1 & 0 \\ -\sin\beta & 0 & \cos\beta \end{bmatrix}; \; R_z = \begin{bmatrix} \cos\delta & -\sin\delta & 0 \\ \sin\delta & \cos\delta & 0 \\ 0 & 0 & 1 \end{bmatrix}; \tag{5.25}$$

with $\theta = \pi/3$, $\beta = \pi/4$ and $\delta = \pi/6$. Results for both, the linear MPFA-D and the MPFA-DNL are shown in Table 9.

Table 9 - Results for the test 5.2.2 - Anisotropic Hollow Domain. The “unexpected” results are highlighted in red.

	MPFA-D			MPFA-DNL		
n_{tetra}	p_{min}	p_{max}	ε_m	p_{min}	p_{max}	ε_m
760	-0.530	1.678	6.19e-2	2.43e-5	1.609	0
1,660	-0.251	1.930	2.46e-2	0	1.902	0
2,193	-0.165	1.856	1.31e-2	1.76e-6	1.842	0
4,471	-0.323	1.888	2.41e-2	0	1.890	0
10,552	-0.146	1.933	8.01e-3	0	1.927	0
17,544	-0.040	1.983	3.55e-3	0	1.975	0

Source: The author (2023).

In Table 9, we can see that the MPFA-D violates the minimum expected pressure for all the tested meshes. On the other hand, the MPFA-DNL keeps the solution within the limits defined by the boundary conditions. Figure 24 shows the pressure fields got from MPFA-D and MPFA-DNL on the most refined tested mesh. As it can be seen, the MPFA-DNL clearly produces a smooth solution without spurious oscillations even for this test case in which we have a highly anisotropic diffusion tensor while the linear MPFA-D produces solutions with undershoots (pressure under the expected minimum).

In terms of computational cost, for the most refined tested mesh, MPFA-DNL needed 251 iteration steps to find the solution without spurious oscillations.

Figure 24 - Pressure field on the mesh with 17,544 tetrahedra for test 5.2.2 - Anisotropic Hollow Domain. The domain was clipped in order to highlight the inner hole. The white regions indicate undershoots. (a) Solution with the linear MPFA-D method. (b) Solution with MPFA-DNL.

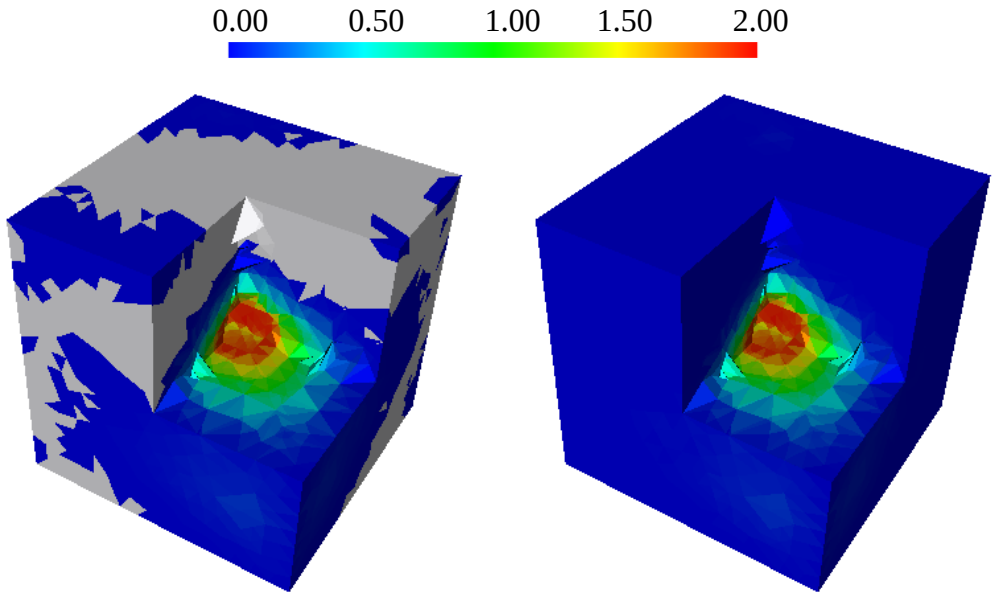

(a) (b)

Source: The author (2023).

5.2.3 Two-Halves Anisotropic Hollow Domain

This test case presents a 3-D example based on the 2-D one of Queiroz et al. (2014). Consider a cubic domain $\Omega_c = [0,1]^3$ with a central cubic hole $\Omega_h = [0.4,0.6]^3$, so that the domain of interest is $\Omega_m = \Omega_c - \Omega_h$. At the external boundary, $\partial\Omega_c$, the scalar variable is set as $p_e = 0$ and at the internal edge, $\partial\Omega_h$, the scalar variable is set as $p_i = 2$. It is a heterogeneous, discontinuous and anisotropic media, with two diffusion tensors that are defined as:

$$\mathbf{K}_1 = R_z^T R_y^T R_x^T \begin{bmatrix} 100 & 0 & 0 \\ 0 & 10 & 0 \\ 0 & 0 & 1 \end{bmatrix} R_x R_y R_z \quad \forall\, x \leq 0.5 \tag{5.26}$$

where:

$$R_x = \begin{bmatrix} 1 & 0 & 0 \\ 0 & \cos\theta & -\sin\theta \\ 0 & \sin\theta & \cos\theta \end{bmatrix};\ R_y = \begin{bmatrix} \cos\beta & 0 & \sin\beta \\ 0 & 1 & 0 \\ -\sin\beta & 0 & \cos\beta \end{bmatrix};$$
$$R_z = \begin{bmatrix} \cos\delta & -\sin\delta & 0 \\ \sin\delta & \cos\delta & 0 \\ 0 & 0 & 1 \end{bmatrix} \tag{5.27}$$

with $\theta = \pi/3$, $\beta = \pi/4$ and $\delta = \pi/6$ and:

$$\mathbf{K}_2 = \begin{bmatrix} \xi\mathbb{x}^2 + \mathbb{y}^2 + \mathbb{z}^2 & -(1-\xi)\mathbb{x}\mathbb{y} & -(1-\xi)\mathbb{x}\mathbb{z} \\ -(1-\xi)\mathbb{x}\mathbb{y} & \mathbb{x}^2 + \xi\mathbb{y}^2 + \mathbb{z}^2 & -(1-\xi)\mathbb{y}\mathbb{z} \\ -(1-\xi)\mathbb{x}\mathbb{z} & -(1-\xi)\mathbb{y}\mathbb{z} & \mathbb{x}^2 + \mathbb{y}^2 + \xi\mathbb{z}^2 \end{bmatrix} \quad \forall\, x > 0.5 \tag{5.28}$$

where $\xi = 1{,}000$, $\mathbb{x} = x + \xi^{-1}$, $\mathbb{y} = y + \xi^{-1}$, $\mathbb{z} = z + \xi^{-1}$.

Table 10 presents the pressure under and overshoot and the norms of error for the linear MPFA-D and for the MPFA-DNL and Figure 25 presents the pressure fields, from both strategies, for the mesh with 15,376 control volumes. In Table 10, we can see that, again, the linear version of MPFA-D violates the DMP, returning non-physical solutions with spurious oscillations for all tested meshes. On the other hand, the MPFA-DNL, even for this highly anisotropic and discontinuous diffusion tensor, keeps the solution between the maximum and the minimum physical bounds for all tested meshes.

Table 10 - Results for the test 5.2.3 - Two-Halves Anisotropic Hollow Domain. The "unexpected" results are highlighted in red.

	MPFA-D			MPFA-DNL		
n_{tetra}	p_{min}	p_{max}	ε_m	p_{min}	p_{max}	ε_m
604	-0.974	1.960	1.05e-1	8.85e-6	1.716	0
4,949	-0.363	2.057	2.59e-2	0	1.994	0
15,376	-0.304	2.118	8.98e-3	0	1.983	0

Source: The author (2023).

Figure 25 - Pressure field on the mesh with 15,376 tetrahedra for test 5.2.3 - Two-Halves Anisotropic Hollow Domain. The domain was clipped in order to highlight the inner hole. The black regions within the domain indicate overshoots and the white regions indicate undershoots. (a) Solution with the linear MPFA-D method. (b) Solution with the MPFA-DNL.

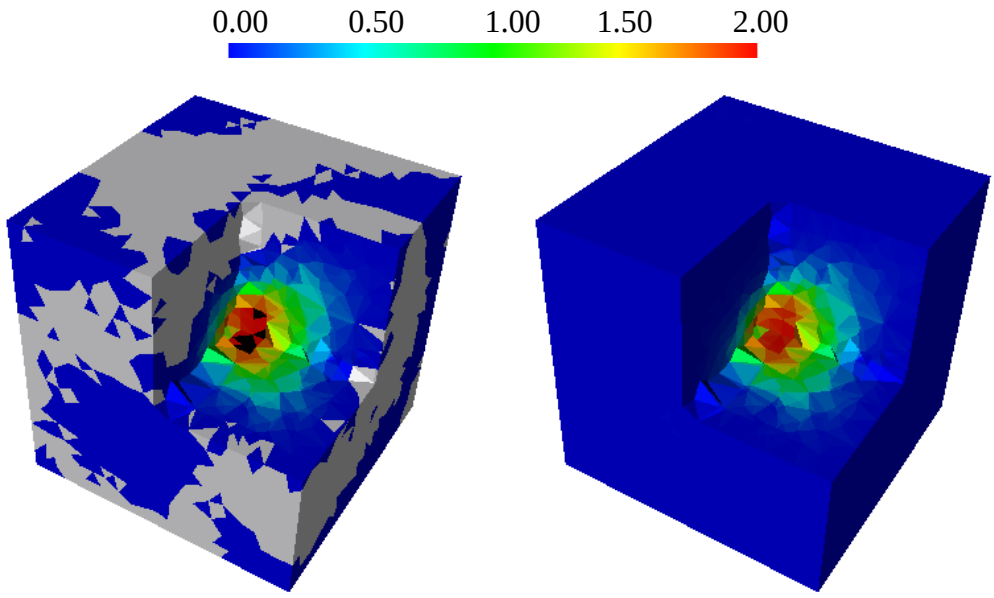

(a) (b)

Source: The author (2023).

In Figure 25, we can see that MPFA-DNL produces a smooth solution without spurious oscillations even for this hard test case, while the linear MPFA-D produces solutions with both, under and overshoots.

In terms of computational cost, for the most refined mesh, MPFA-DNL needed 157 iteration steps to find the solution without spurious oscillations.

5.3 SINGLE-PHASE FLOW SIMULATION

This example was included to demonstrate the capability of the methodology proposed here (MPFA-D – GLS interpolation – pEDFM – unstructured tetrahedral grids) to accurately reproduce the pressure field in context of a fractured reservoir. This example is based on the benchmark test case 1 of Berre et al. (2021) with a domain $\Omega_m = [0,100]^3$ m divided into four subdomains $\Omega_m = \cup_{i=1}^{4} \Omega_i$ according to Figure 26.

Figure 26 - Domain for test 5.3 - Single-Phase Flow Simulation.

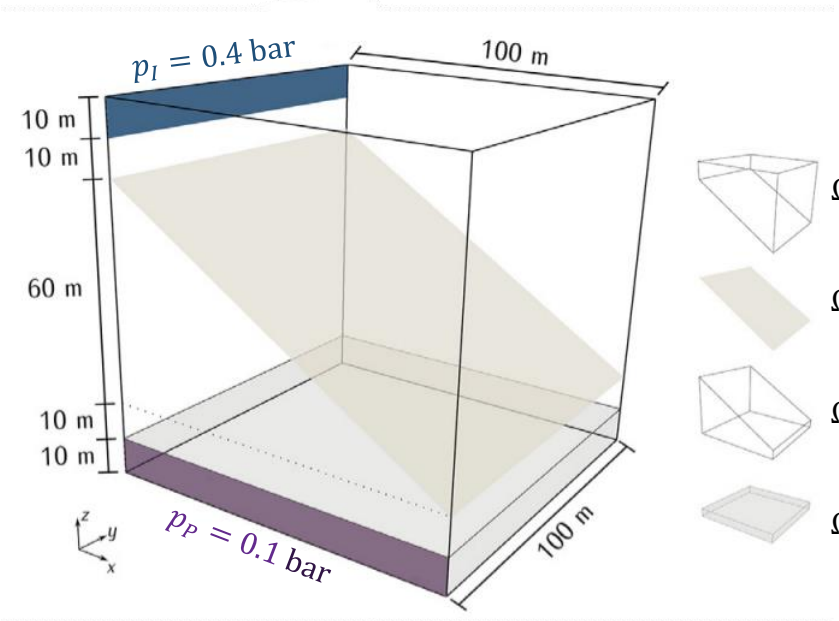

Source: Adapted from Berre et al. (2021).

In Figure 26, Ω_2 is a planar fracture with an aperture of 0.01 m. The rock matrix domains Ω_1 and Ω_3 are, respectively, the subdomains above and below to Ω_2. The subdomain Ω_4 represents a heterogeneity within the rock matrix. There are two parts of the cube faces that are assigned as Dirichlet boundaries. One has prescribed pressure of $p_I = 0.4$ bar and is marked in blue in Figure 26, while the other has prescribed pressure of $p_P = 0.1$ bar and is marked in purple in Figure 26. All remaining parts of the boundary are assigned no flow conditions. Moreover, the permeability tensors are defined as:

$$\mathbf{K}_i = \kappa_i \boldsymbol{I}_{3\times3} \text{ in } \Omega_i \text{ with (i} = 1 \ldots 4) \tag{5.29}$$

with $\kappa_1 = \kappa_3 = 10^{-6}$ D (darcy), $\kappa_2 = 10^{-3}$ D and $\kappa_4 = 10^{-5}$ D. Beyond this, $\boldsymbol{I}_{3\times3}$ is the identity matrix. Finally, the porosities are defined as $\phi_1 = \phi_3 = 0.2$, $\phi_3 = 0.25$ and $\phi_4 = 0.4$.

The pressure field obtained in the referred conditions is so that its outline on the segment from $(0,100,100)$ to $(100,0,0)$ is as shown in Figure 27. Three unstructured tetrahedral meshes were used in this example, respectively with 9,919, 21,648 and 66,495 cells. Figure 27 shows that, even for the coarsest mesh, the methodology proposed here achieve good adherence to the reference solution. As expected, the response obtained from the finest grid is the closest one to the reference solution, obtained based on the benchmark work of Berre et al. (2021).

Figure 27 – Outline of the solution of test 5.3 - Single-Phase Flow Simulation.

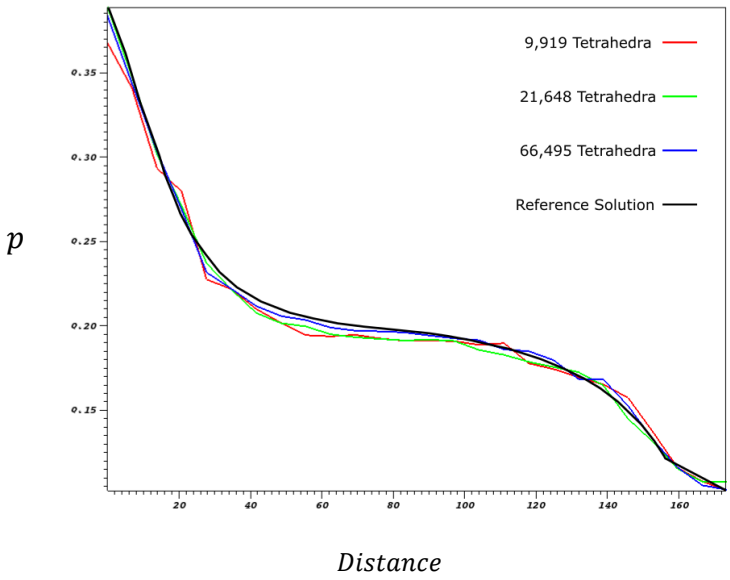

Source: The author (2023).

5.4 TWO-PHASE FLOW SIMULATION

This subsection finally presents the simulation of immiscible two-phase flow in fractured porous media. All the domains modelling the reservoir rocks (Ω_m) are

discretized by using truly unstructured tetrahedral meshes, while the fractures (Ω_{f_i}) are considered to be 2-D rectangles discretized using Cartesian grids. There is not any operational impediment to using general polygonal meshes in this context, it was just chosen to simplify the comparison with pEDFM using Cartesian grids. In the tests in which they are relevant, these comparisons are made changing the mesh discretizing Ω_m (tetrahedral vs. Cartesian), but keeping the meshes discretizing the fractures. Whenever necessary, the well model of Peaceman (1977) is used to obtain the well source terms of each phase for a rock matrix cell $\hat{k}$ as:

$$(\rho_\alpha q_\alpha)_{\hat{k},w} = \rho_\alpha \lambda_\alpha \mathrm{K}_{\hat{k}} (p_w - p_{\hat{k}}) \tag{5.30}$$

in which p_w (with $w = I, P$; for injector or producer, respectively) is the well prescribed pressure.

Beyond this, unless explicitly stated otherwise, consider, in all the tested examples, that $\mathrm{K}_{\hat{k}} = 10^{-14}\ \mathrm{m}^2$ to be applied in Eq. (5.30) and $S_{wi} = S_{or} = 0$ to be applied in Eq. (2.8). Moreover, the other necessary rock and fluid parameters are defined, unless explicitly stated otherwise, as: $\phi = 0.2$ (rock porosity), $\rho_w = 1{,}000\ \mathrm{kg/m^3}$ (water density), $\rho_o = 800\ \mathrm{kg/m^3}$ (oil density), $\mu_w = 0.001\ \mathrm{Pa \cdot s}$ (water viscosity), $\mu_o = 0.001\ \mathrm{Pa \cdot s}$ (oil viscosity), $c_{fw} = 0.4 \cdot 10^{-9}\ \mathrm{Pa^{-1}}$ (water compressibility), $c_{fo} = 0.6 \cdot 10^{-9}\ \mathrm{Pa^{-1}}$ (oil compressibility), $S_w^0 = 0$ (initial water saturation), $S_o^0 = 1$ (initial oil saturation), $p_w^0 = p_o^0 = 0.2$ GPa (initial phase pressure), while $\boldsymbol{I}_{3\times3}$ is the identity matrix.

For comparison purposes, beyond solving the problems using the methodology proposed here (MPFA-D for matrix-matrix interactions – GLS interpolation – pEDFM – backward Euler time discretization – upwind – unstructured tetrahedral grids), some problems were also solved using Cartesian grids and TPFA for matrix-matrix interactions, which is a common strategy in context of pEDFM (this scheme was already programed in DARSim). In all the examples, applying tetrahedral grids means the application of the complete methodology proposed in this work, while applying Cartesian grids means the application of TPFA and of the classical pEDFM (ŢENE et al., 2017; HOSSEINIMEHR et al., 2022) together with them. Note that MPFA-DNL was not applied on the two-flow simulation, not that it is something impractical, it just was not carried out in the period of development of this thesis.

5.4.1 Phases Segregation

In order to evaluate if the part of the numerical formulation related to gravity effects is correctly implemented, the following test was performed: consider a cubic domain $\Omega_m = [0,100]^3$ m with null flux at all its boundaries (closed box), with the rock matrix permeability ($\mathbf{K_m}$) is defined as:

$$\mathbf{K_m} = \boldsymbol{I}_{3\times3} \cdot 10^{-14}\ \mathrm{m}^2 \tag{5.31}$$

There are two phases within the domain, oil and water, so that, initially, $S_w^0 = S_o^0 = 0.5$ all over the domain and there is not any injection or extraction of fluid through wells. As time goes by, it is expected that the phases will segregate and that the water phase, being denser, will accumulate in the lower part of the cube. The test was performed using an unstructured tetrahedral grid with 31,475 cells, shown in Figure 28a, and a Cartesian grid ($40 \times 40 \times 40$), shown in Figure 28b.

Figure 28 - Results of example 5.4.1 - Phases Segregation. Water saturation after 500 days: (a) Tetrahedral grid. (b) Cartesian grid.

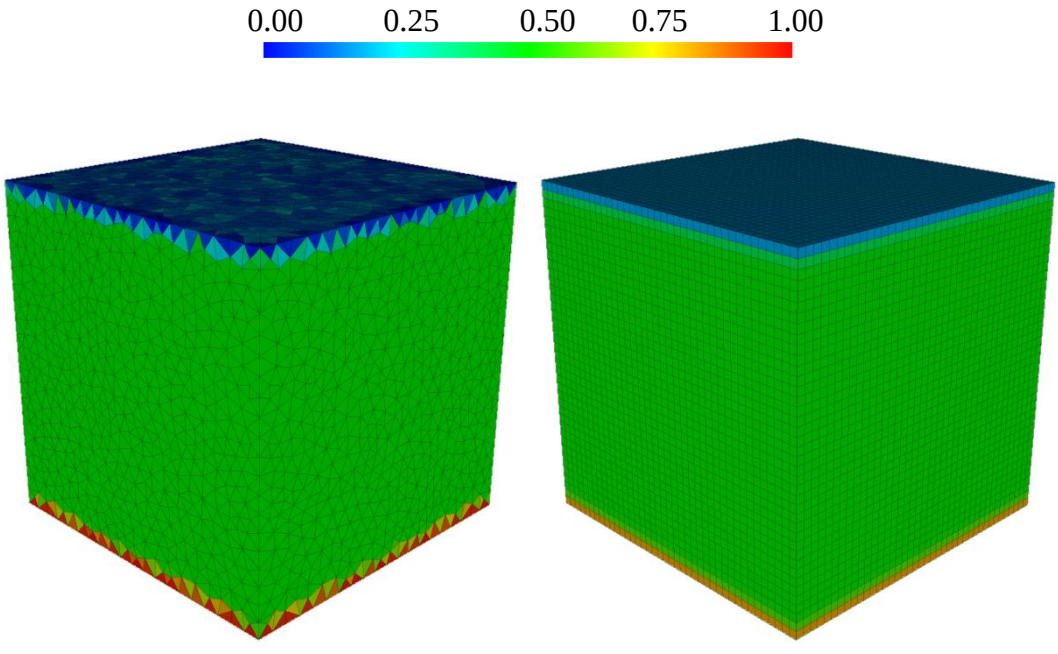

(a) (b)

Source: The author (2023).

Figure 28 shows the water saturation after 500 days. As expected, the tops of the cubes have lower water saturation than the bottom. Waiting long enough, we would see all the water phase in the bottom half of the domain and all the oil in the top half. However, the long time needed to reach such a state, under the given conditions, discouraged waiting for this result. Despite this, the reproduction of the phenomenon occurs in the right (physical) direction, demonstrating the correct implementation of the numerical formulation for gravity effects, which was the intention of this test.

5.4.2 Isotropic Tensor in a Cuboid Domain with One Fracture

Consider a cubic domain $\Omega_m = [0,100]^3$ m with null flux at all its boundaries (closed box). There are two wells: the injector one at $\vec{x}_I = (10,\ 90,\ 100)$ m have a prescribed pressure $p_I = 0.03$ GPa, while the producer one at $\vec{x}_P = (90,\ 10,\ 100)$ m has a prescribed pressure $p_P = 0.01$ GPa. The rock matrix permeability ($\mathbf{K_m}$) is defined as:

$$\mathbf{K_m} = \boldsymbol{I}_{3\times3} \cdot 10^{-14}\ \mathrm{m}^2 \tag{5.32}$$

Moreover, within this domain, there is one fracture and two wells, placed according to Figure 29. A tetrahedral mesh with 60,963 cells was used to obtain the results to be compared with those from a Cartesian grid ($47 \times 47 \times 47$) with 103,823 cells (used as reference). The fracture was discretized as a 2-D 38×38 Cartesian grid and its permeability was considered as in two cases:

$$\mathbf{K_{f_1}} = \boldsymbol{I}_{3\times3} \cdot 10^{-6}\ \mathrm{m}^2 \ \text{ and } \ \mathbf{K_{f_2}} = \boldsymbol{I}_{3\times3} \cdot 10^{-22}\ \mathrm{m}^2 \tag{5.33}$$

5.4.2.1 Case 1 – Conductive Fracture

Considering that the fracture permeability is $\mathbf{K_{f_1}} = \boldsymbol{I}_{3\times3} \cdot 10^{-6}\ \mathrm{m}^2$, the results obtained are those shown in Figure 30 and Figure 31. Figure 30 shows the water saturation field after 750 days in tetrahedral mesh (Figure 30a) and in Cartesian mesh (Figure 30b). These figures are slices on the whole solution made by a parallel plane to axis z and crossing both wells.

Figure 29 – Domain configuration for test 5.4.2 - Isotropic Tensor in a Cuboid Domain with One Fracture.

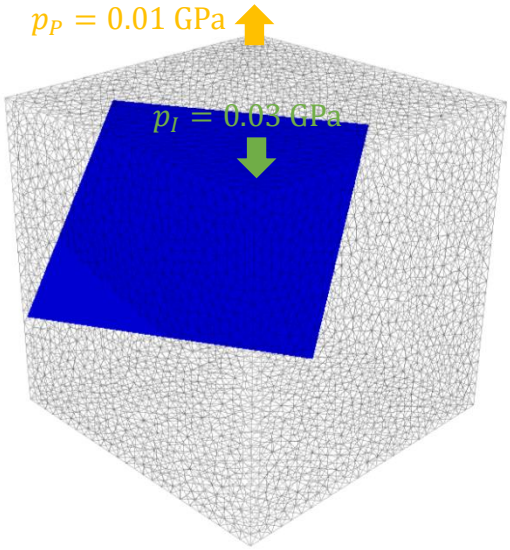

Source: The author (2023).

Figure 30 - Water saturation, after 750 days, field in test 5.4.2.1 - Case 1 – Conductive Fracture. It is a slice by a parallel plane to axis z and crossing both wells. (a) Tetrahedral grid. (b) Cartesian grid.

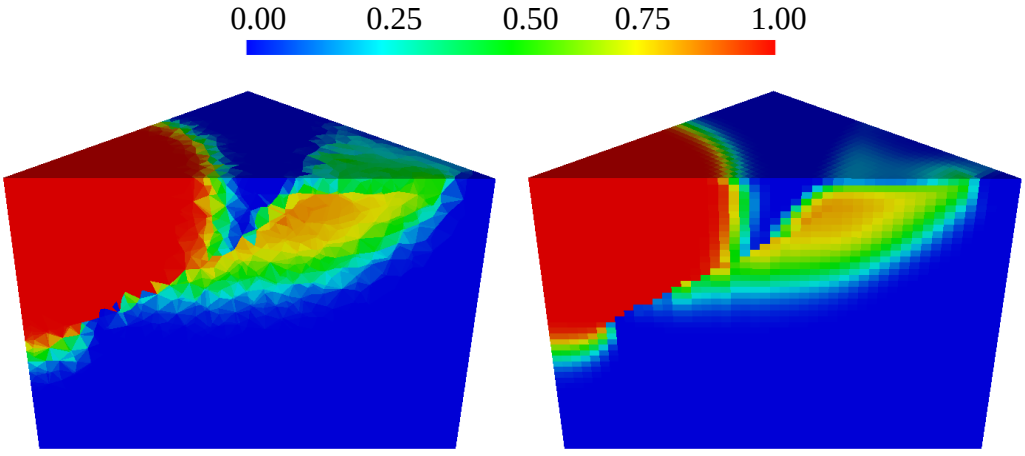

(a) (b)

Source: The author (2023).

The solutions obtained in the two meshes are similar, in terms of water saturation field, except for the region around the production well, where water saturation is greater when using the tetrahedral mesh. This is in line with the water production shown graph in Figure 31b, which indicates an anticipation of about 60 days of the water breakthrough

in the production well, when using the tetrahedral mesh, compared to the Cartesian mesh solution. The cumulative oil productions using both grids are around 30,000 m³ after 750 days of water injection (see Figure 31a).

Figure 31 – Cumulative oil and water production of test 5.4.2.1 - Case 1 – Conductive Fracture. (a) Cumulative oil production. (b) Cumulative water production.

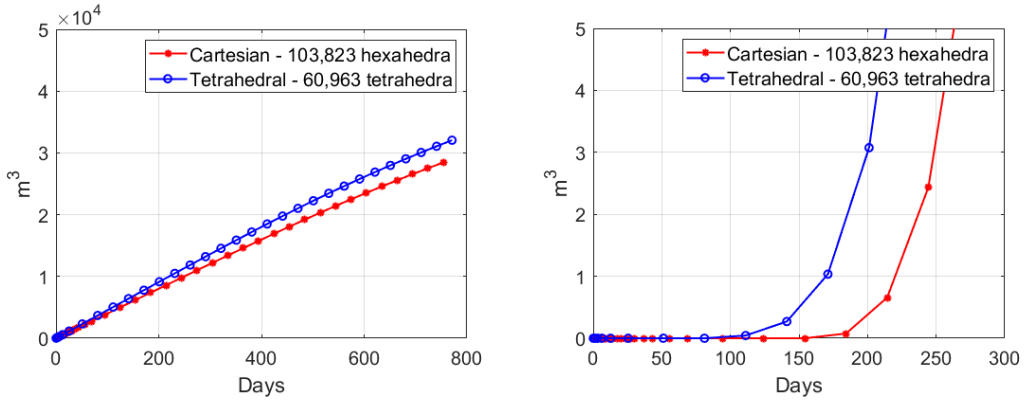

Source: The author (2023).

5.4.2.2 Case 2 – Flow Barrier

Considering that the fracture permeability is $\mathbf{K}_{f_1} = \boldsymbol{I}_{3\times3} \cdot 10^{-22}$ m^2, the results obtained are those shown in Figure 32 and Figure 33.

Figure 32 shows the water saturation field after 750 days in tetrahedral mesh (Figure 32a) and in Cartesian mesh (Figure 32b). These figures are slices on the whole solution made by a parallel plane to axis z and crossing both wells. The solutions obtained in the two meshes are similar, in terms of water saturation field, despite the difference of about 60 days in time of water breakthrough observed in Figure 33b, with the solution using the tetrahedral mesh presenting an anticipated starting of water production, compared to the Cartesian mesh solution. The cumulative oil productions using both grids are higher than 30,000 m³ after 750 days of water injection (see Figure 33a).

It is expected that all these differences between solutions from tetrahedral and Cartesian grids decrease as the meshes are refined, until the converged solution is reached. For this, of course, it would be necessary a large processing capacity or a great improvement in the efficiency of the used software.

Figure 32 - Water saturation, after 750 days, field in test 5.4.2.2 - Case 2 – Flow Barrier. It is a slice by a parallel plane to axis z and crossing both wells. (a) Tetrahedral grid. (b) Cartesian grid.

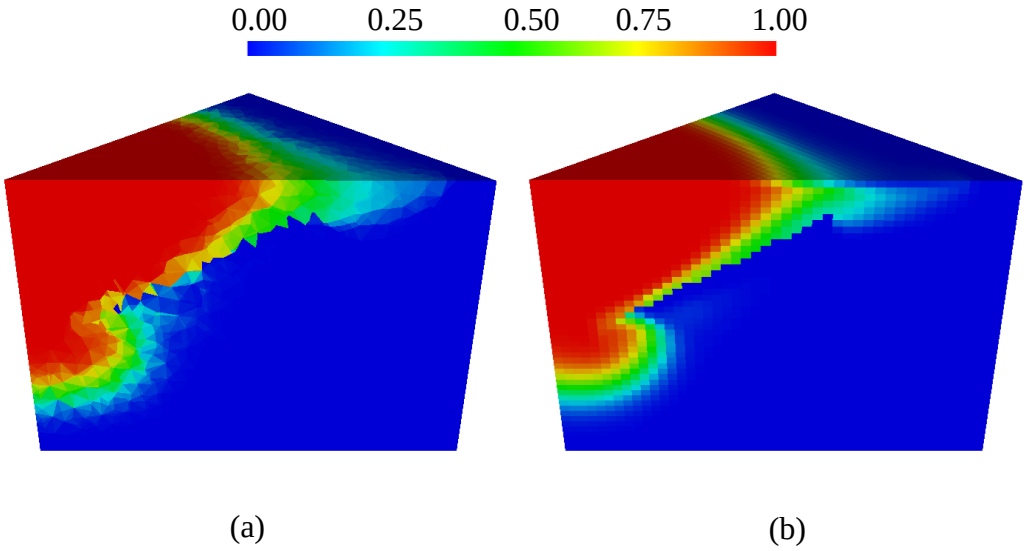

(a) (b)

Source: The author (2023).

Figure 33 – Cumulative oil and water production of test 5.4.2.2 - Case 2 – Flow Barrier. (a) Cumulative oil production. (b) Cumulative water production.

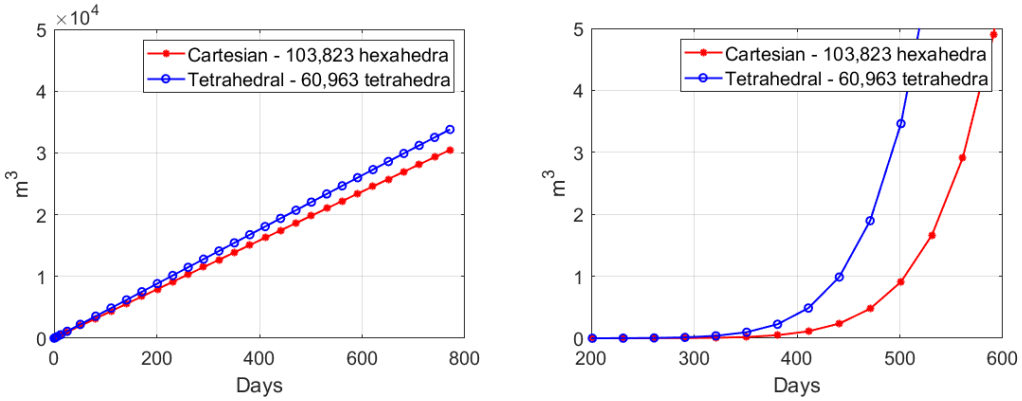

(a) (b)

Source: The author (2023).

The search for the converged solution can be left for further works, while this example was enough to show that the results obtained with the methodology proposed here are in line with those obtained by a more established strategy.

Comparing the two cases (high and low permeability fracture), the high permeability fracture, as expected, conducts the water saturation front to closer to the production well, anticipating the water breakthrough (which occurs before 200 days), when compared with the low permeability fracture (see Figure 31b and Figure 33b), which enforces the water saturation front to walk around it, as shown in Figure 32a, so that the water breakthrough occurs after more than 300 days.

5.4.3 Isotropic Tensor in a Flat Cuboid Domain with Multiple Fractures

This test is based on the work of HosseiniMehr et al. (2022). Consider a flat cuboid domain ($\Omega_m = [100 \times 100 \times 1]$ m) with two wells: the injector one at $\vec{x}_I = (0,\ 0,\ 1)$ m have a prescribed pressure $p_I = 0.03$ GPa, while the producer one at $\vec{x}_P = (100,\ 100,\ 1)$ m have a prescribed pressure $p_P = 0.01$ GPa. Beyond this, there are 30 fractures distributed as shown in Figure 34 (blue lines are conductive fractures and red lines are barriers). The fluids are incompressible and can not cross through the boundaries of the domain (closed box). The rock matrix permeability ($\mathbf{K_m}$) and the fractures permeabilities ($\mathbf{K_{f1}}$ and $\mathbf{K_{f2}}$) are defined as:

$$\mathbf{K_m} = \boldsymbol{I}_{3\times3} \cdot 10^{-14}\ \text{m}^2;\ \mathbf{K_{f1}} = \boldsymbol{I}_{3\times3} \cdot 10^{-6}\ \text{m}^2;\ \mathbf{K_{f2}} = \boldsymbol{I}_{3\times3} \cdot 10^{-22}\ \text{m}^2 \qquad (5.34)$$

Moreover, in this case $n_{tetra} = 81{,}455$ and each fracture is discretized as a 2-D Cartesian grid (40×1), so that $n_{polyg}^{k} = 40$ with $k = 1 \ldots 30$. Figure 35 presents the water saturation field obtained using the referred tetrahedral mesh after 51 and 291 days of injection of water. It is possible to observe that the barriers (low permeability fractures, marked as black lines) really prevent the advance of the water saturation front through them, forcing it to walk around them, in the same way, the channels (high permeability fractures, marked as white lines) really conduct the fluid forward in the reservoir, as expected.

Figure 36 presents the comparison between the water saturation fields obtained by using tetrahedral and Cartesian grids (classically used in context of pEDFM). The used Cartesian grid has the following discretization: $206 \times 206 \times 2$ (leading to 84,872 hexahedral control volumes, that is close to the number of degrees of freedom of the tetrahedral mesh). We can observe that all the effects of the presence of fractures that are captured using Cartesian meshes are also captured when using tetrahedral ones.

Figure 34 - 2D top visualization of the fractures distribution for the test 5.4.3 - Isotropic Tensor in a Flat Cuboid Domain.

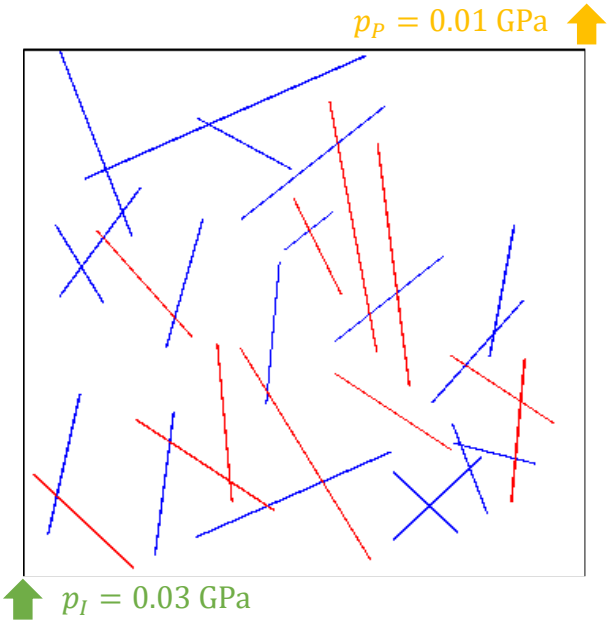

Source: The author (2023).

Figure 35 - Results (on tetrahedral mesh) of the test 5.4.3 - Isotropic Tensor in a Flat Cuboid Domain. Conductive fractures as white lines and barriers as black lines. Water saturation field after: (a) 51 days. (b) 291 days.

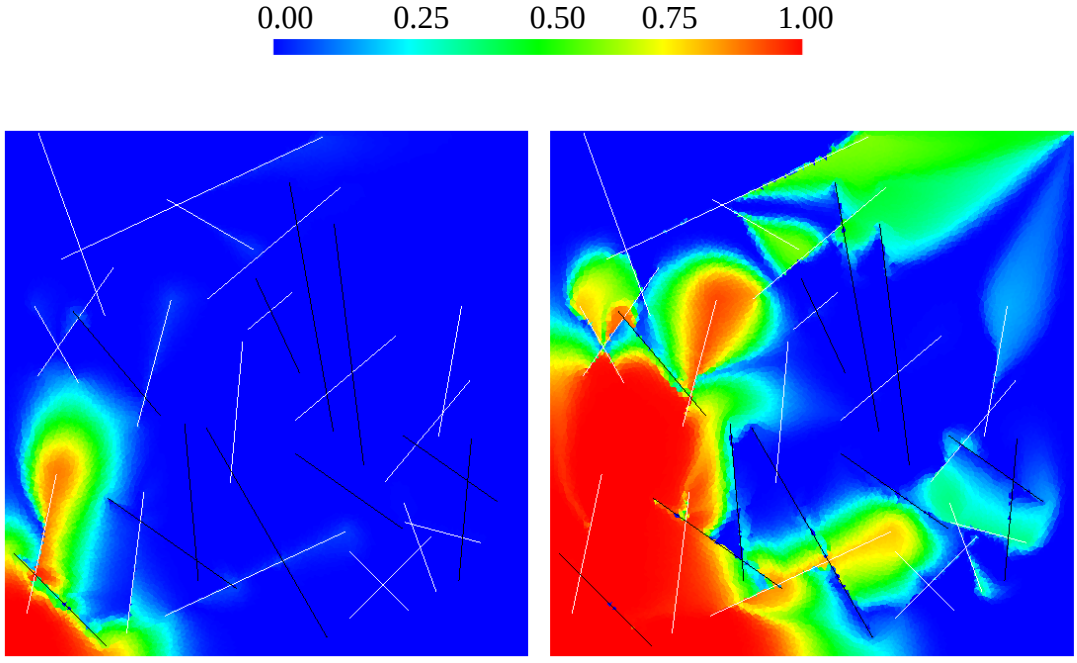

(a) (b)

Source: The author (2023).

Figure 37 presents the comparison between the solutions obtained with tetrahedral and Cartesian grids, in terms of cumulative oil and water production. The curves relative to oil extraction are very close to each other, achieving about 800 m^3 of cumulative production after 500 days (see Figure 37a).

Figure 36 - Results of the test 5.4.3 - Isotropic Tensor in a Flat Cuboid Domain. Conductive fractures as white lines and barriers as black lines. Water saturation field after 291 days using: (a) Tetrahedral Grid. (b) Cartesian Grid.

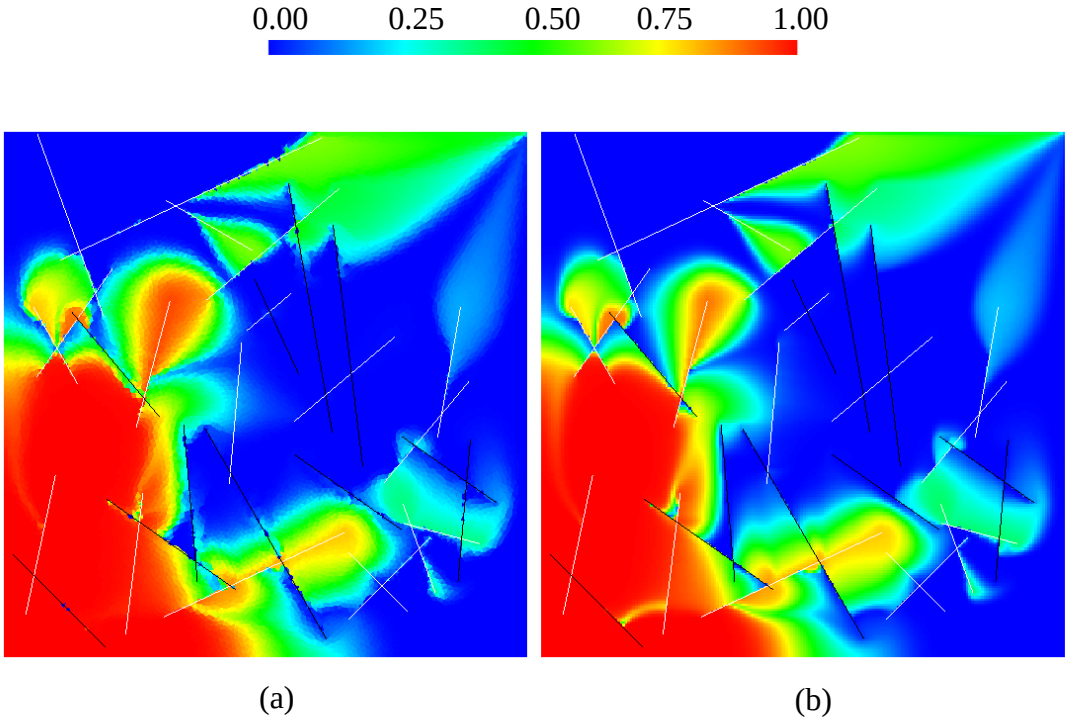

(a) (b)

Source: The author (2023).

Beyond this, the solutions obtained with both meshes indicate an almost simultaneous water breakthrough (see Figure 37b). This is one more example showing that the results obtained with the methodology proposed here are in line with those obtained by a more established strategy. Moreover, the proximity of the results in this case seems to indicate the expected tendency, announced in previous examples, that the results obtained in the two types of mesh should approach, as refinement degree of the meshes increases and the number of degrees of freedom of the tetrahedral grid approaches that of the Cartesian one. Evidently, this hypothesis should be adequately tested in the future.

Figure 37 – Cumulative oil and water production of test 5.4.3 - Isotropic Tensor in a Flat Cuboid Domain with Multiple Fractures. (a) Cumulative oil production. (b) Cumulative water production.

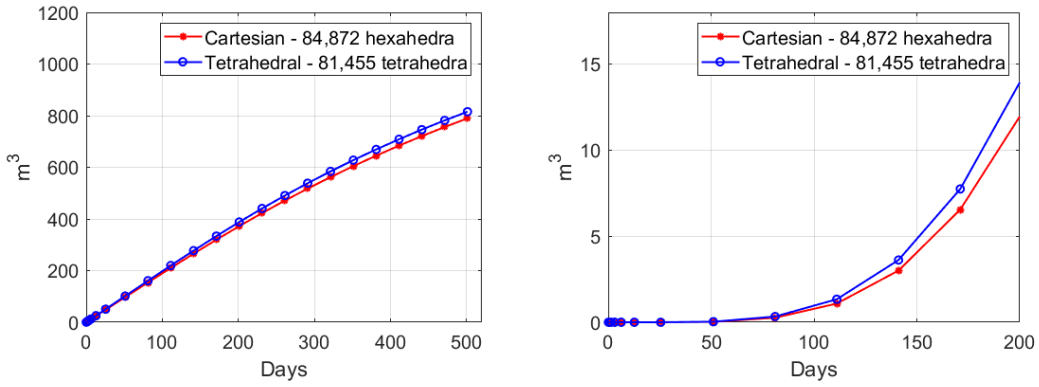

(a) (b)

Source: The author (2023).

5.4.4 Full Tensor in a Non-Cuboid Domain

Consider a domain geometry shown in Figure 38 with a full tensor for the rock matrix permeability ($\mathbf{K}_{\boldsymbol{m}}$) defined in Eq. (5.35). There are three wells, one injector well at $\vec{x}_I = (10,\ 10,\ 100)$ m with a prescribed pressure $p_I = 0.03$ GPa and two producer wells at $\vec{x}_{P_1} = (40,\ 40,\ 40)$ m and at $\vec{x}_{P_2} = (0,\ 0,\ 0)$ m with prescribed pressures $p_{P1} = p_{P2} = 0.01$ GPa. Beyond this, there are 6 fractures distributed as shown in Figure 38.

$$\mathbf{K}_{\boldsymbol{m}} = \begin{bmatrix} 0.3889 & 0.2823 & -0.3112 \\ 0.2823 & 0.3759 & -0.3041 \\ -0.3112 & -0.3041 & 0.4352 \end{bmatrix} \cdot 10^{-13}\ \mathrm{m}^2 \tag{5.35}$$

The fractures are placed as shown in Figure 38, in which the blue ones are the conductive fractures and the red ones are the flow barriers, whose permeabilities are defined as:

$$\mathbf{K}_{\boldsymbol{f_1}} = \boldsymbol{I}_{3\times3} \cdot 10^{-6}\ \mathrm{m}^2 \ \text{ and } \ \mathbf{K}_{\boldsymbol{f_2}} = \boldsymbol{I}_{3\times3} \cdot 10^{-22}\ \mathrm{m}^2 \tag{5.36}$$

Besides, the fluids are incompressible and can not cross through the boundaries of the domain. Finally, the tetrahedral grid here used have the following number of cells: $n_{tetra} = 26{,}913$. Figure 39 shows the water saturation fields in two situations: considering and not considering the presence of the fractures. Figure 39a and Figure 39c show the water saturation field in the case of fractures "turned off", respectively after 51 and 500 days, so that we can see the expected behavior of the referred fluid due to the anisotropic permeability tensor presented in Eq. (5.35). Note (in Figure 39a) that, in this condition, the water saturation front clearly achieve the well P1 during the first 51 days of injection, while, when considering the presence of the fractures, it seems to do not achieve, according to Figure 39b.

Figure 38 – Main domain and fractures and wells positions for the test 5.4.4 - Full Tensor in a Non-Cuboid Domain. The red rectangles represent low permeabilities fractures, while the blue ones represent high permeabilities fractures.

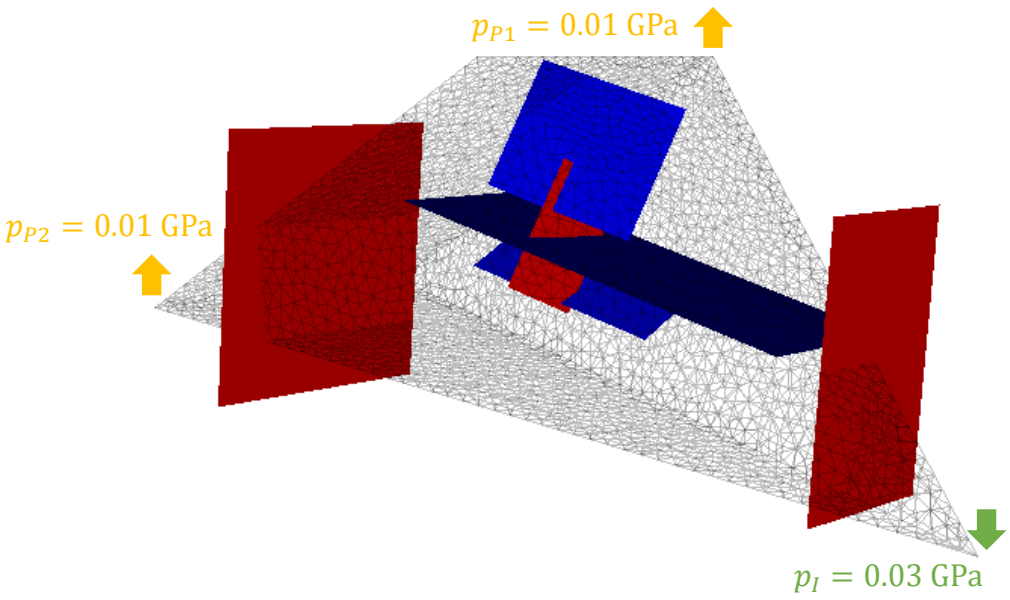

Source: The author (2023).

However, Figure 40b indicates that there was already water production in P1 at that time, even considering the presence of the fractures. Nevertheless, the water production is lower in the second than in the first situation. On the other hand, the highlighted barrier in Figure 39b prevents that the water saturation front walks directly to P1, enforcing it to walk around the barrier and sweep parts of the reservoir that would not

be reached by it, increasing the cumulative oil production, as shown in Figure 40a. Disregarding fractures, oil production at P1 would be underestimated.

Also note (in Figure 40c) that, when fractures are "turned off", the water breakthrough does not occur in well P2 during the first 500 days of injection, what is confirmed by the graph of cumulative water production in P2 (Figure 40d). The conductive fractures carry the water saturation front to the vicinity of P2, as shown in Figure 39d. The presence of a highlighted barrier, however (in Figure 40d), enforces the water saturation front to walk around it, in order to access P2.

Figure 39 – Water saturation field in test 5.4.4 - Full Tensor in a Non-Cuboid Domain. (a) Fractures “turned off” condition at 51 days. (b) Fractures “turned on” condition at 51 days. (c) Fractures “turned off” condition at 500 days. (d) Fractures “turned on” condition at 500 days.

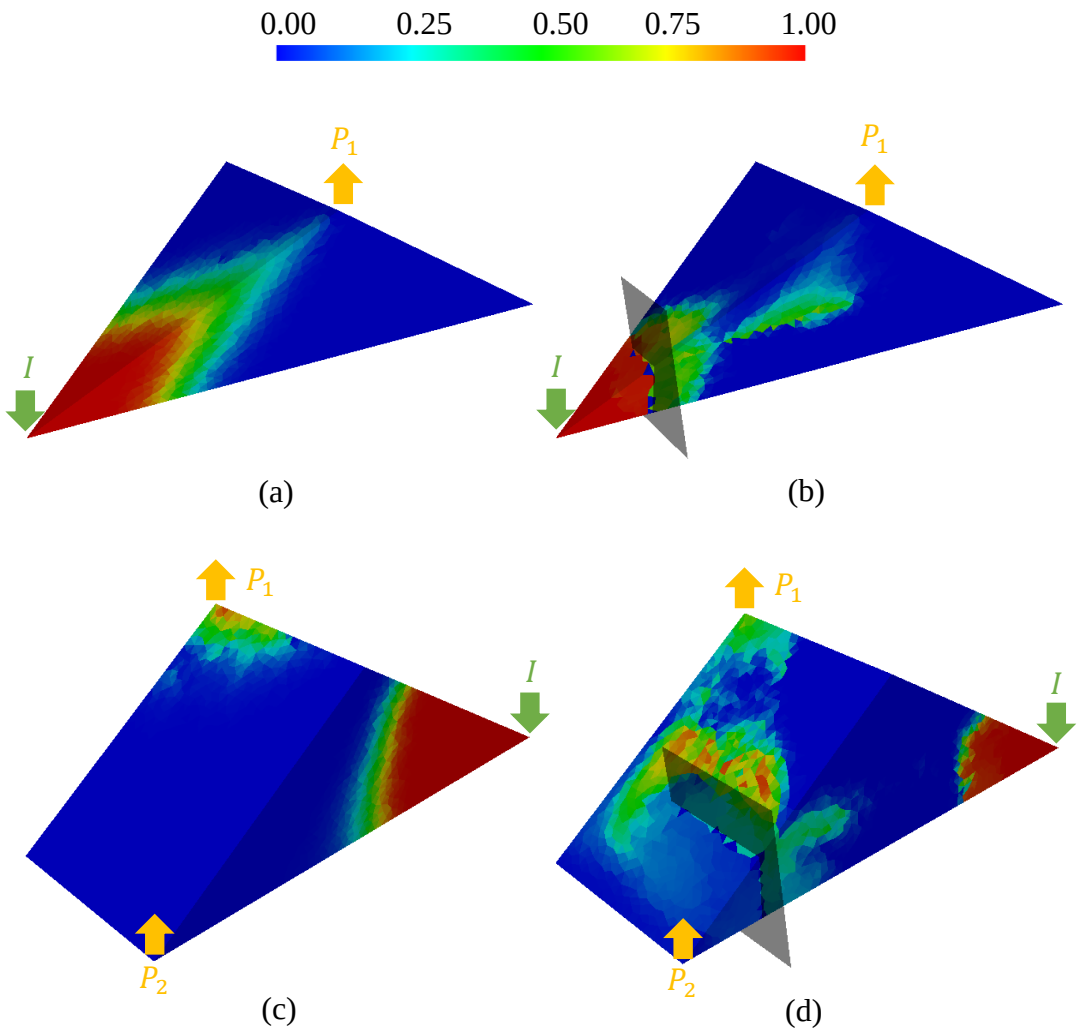

Source: The author (2023).

The water production in this last situation is confirmed in Figure 40d. The arrival of water in P2 harms its cumulative oil production, as shown in Figure 40c. Disregarding fractures, oil production at P2 would be overestimated.

Figure 40 – Cumulative oil and water production of test 5.4.4 - Full Tensor in a Non-Cuboid Domain. (a) Cumulative oil production in P1. (b) Cumulative water production in P1. (c) Cumulative oil production in P2. (d) Cumulative water production in P2.

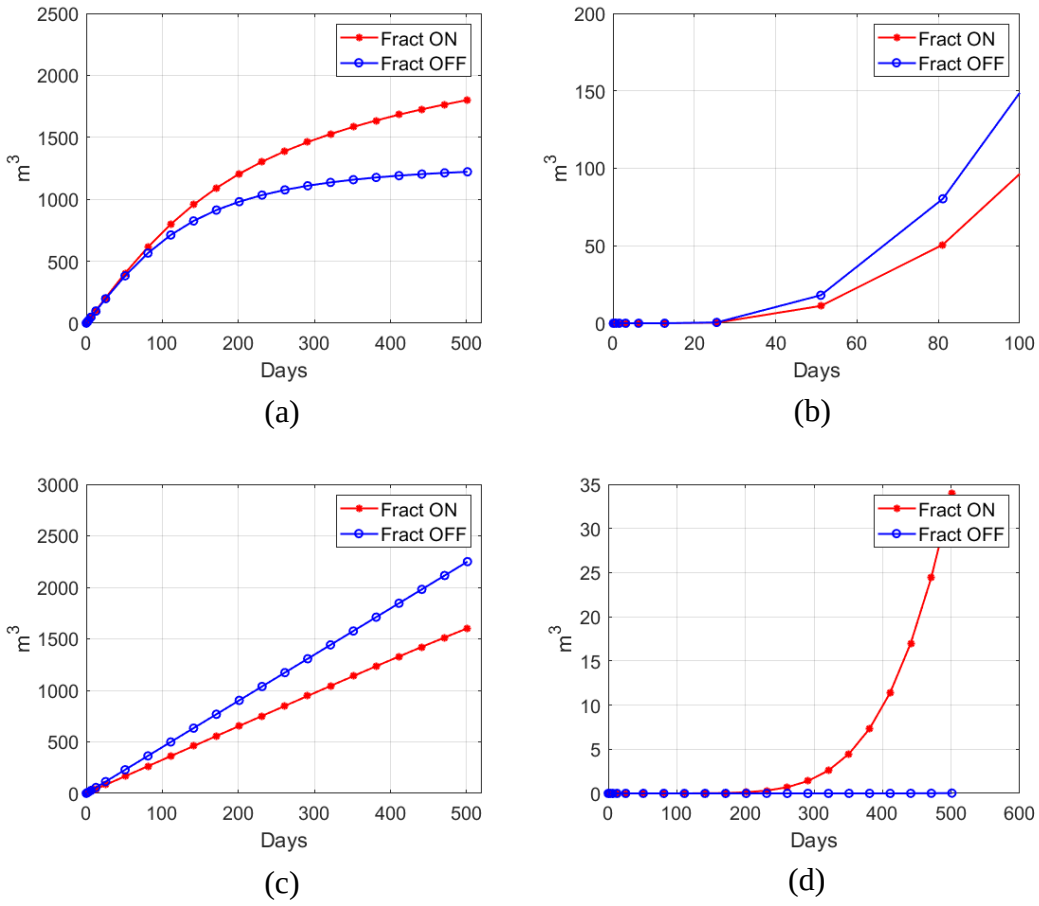

Source: The author (2023).

6 CONCLUSIONS

This thesis presents the development of a numerical tool for the simulation of two-phase flow in naturally fractured reservoirs using unstructured tetrahedral meshes. Some stages had to be overcome until reaching the major objective of this work. First, it was necessary to develop a finite volume formulation, suitable for tetrahedral control volumes, to discretize the so-called "pressure terms" of the mathematical model that, under some simplifications, describes the aforementioned physical phenomenon (see chapter 2). It was developed a multipoint flux approximation scheme that uses a "diamond stencil" (MPFA-D) to be applied on tetrahedral meshes (LIRA FILHO et al., 2021). The formulation presented here includes the possibility to add the gravity effects to the flux calculation. Since MPFA-D involves nodal interpolations, it was also necessary to develop interpolation strategies that met the desired requirements, such as the preservation of linearity. Other interpolation strategies found in the literature were also tested, in order to select the most robust one. Among the tested interpolation strategies, namely, LPEW1, LPEW2, LPEW3 (LIRA FILHO et al., 2021), LPEW-HAP (YANG; GAO, 2020) and GLS (DONG; KANG, 2021, 2022), the last one presented the best results. All these strategies showed to be linearity preserving, but not all of them reach the second order convergence rate for pressure on any tetrahedral meshes or permeability tensors. LPEW-HAP has its convergence condition strictly dependent on the mesh, even for mild anisotropic tensors. LPEW1, LPEW2 and LPEW3 are capable to handle highly heterogeneous and mild anisotropic tensors, achieving second order accuracy for pressure and first order accuracy for fluxes, but are not adequate to applications with strongly anisotropic tensors. Thus, GLS was the chosen interpolation to compute the vertex unknowns in context of MPFA-D, because ensures convergence in all the tested situations with satisfactory convergence rates. Despite the remarkably good results presented by it, the linear MPFA-D scheme using GLS does not ensure the respect to DMP and may give rise to undershoots and overshoots depending on the conditions in which it is applied.

In this context, the MPFA-DNL (CAVALCANTE et al., 2022) method was developed, which is a modified nonlinear version of the original linear MPFA-D method of Lira Filho et al. (2021). It was designed to avoid the violation of the DMP that may occur in MPFA-D solutions, since it is not guaranteed to be a monotone scheme, particularly for highly heterogeneous and anisotropic diffusion tensors or distorted meshes. The original linear MPFA-D was modified through of a flux splitting strategy (PAL; EDWARDS, 2006, 2011) that splits the flux in a Two-Point Flux Approximation (TPFA) flux contribution and the Cross Diffusion Terms (CDT). Since the latter part is

the potential source of spurious oscillations in the scalar field, a flux limiting (KUZMIN; SHASHKOV; SVYATSKIY, 2009) was performed on the CDT part. These modifications gave rise to a method which is capable to satisfy the Discrete Maximum Principle eliminating spurious oscillations for the scalar field, even for highly heterogeneous and arbitrary anisotropic diffusion tensors, without harming the convergence rates of the original MPFA-D. Thus, MPFA-DNL method is still capable to achieve second order of accuracy for pressure and first order for fluxes.

Since the objective of this thesis is to study fluid flow in fractured reservoirs, it was necessary to develop strategies to handle this type of entities in context of the computational simulation intended. After investigating several alternatives developed over the years for this purpose, it was decided to use the pEDFM (JIANG; YOUNIS, 2017; ŢENE et al., 2017; RAO et al., 2020; HOSSEINIMEHR et al., 2022) as fracture model. When using this model, it is not necessary to build the mesh fitting the fracture positions, which makes this task simpler and less susceptible to local over refinements. This model is also capable of reproducing the effects of the presence of both high and low permeability fractures. Thus, a pEDFM adapted to unstructured tetrahedral meshes was developed and is presented here.

This way, in context of a fully implicit scheme, it was possible to satisfactorily simulate immiscible two-phase flow in fractured reservoirs using unstructured tetrahedral meshes, MPFA-D and pEDFM. It should be noted that the MPFA-DNL was not applied in context of two-phase flow simulation, not that it is something impractical, it just was not carried out in the period of development of this thesis.

The simulation tool we developed proved to be able to handle general tetrahedral meshes and full (mild anisotropic) permeability tensors, besides presenting results that are in line with those obtained using TPFA and Cartesian grids (classically used in pEDFM context), reproducing adequately the effects of the presence of both high and low permeability fractures and resulting in similar water saturation fields and production curves.

As further works, the fractures discretization could be modified, in order to build 2-D unstructured grids and apply 2-D MPFA on it. The MPFA-DNL could be also adapted to be coupled to the main simulation tool and make it capable to deal with highly anisotropic tensors. The implementation and testing of those more sophisticated transmissibility terms, according to Eq. (4.14) to Eq. (4.16). It would be also interesting and useful to extend the presented MPFA-D to other polyhedral elements, such as

hexahedral meshes. Beyond this, the developed formulations could be applied in context of multiscale modelling, making it suitable for real field applications. Moreover, it is important to perform a convergence study on the presented simulation tool, using highly refined meshes, and, in this context, work on efficiency increasing of it. It could also be investigated some non-Darcy models for flow inside fractures, as well as more adequate relative permeability and mobility models for these media, since they are quite different from the porous rock matrix.

REFERENCES

AAVATSMARK, I. An introduction to multipoint flux approximations for quadrilateral grids. **Computational Geosciences**, *[S. l.]*, v. 6, n. 3–4, p. 405–432, 2002. DOI: 10.1023/A:1021291114475.

AAVATSMARK, I.; BARKVE, T.; BØE; MANNSETH, T. Discretization on unstructured grids for inhomogeneous, anisotropic media. Part I: Derivation of the methods. **SIAM Journal of Scientific Computing**, *[S. l.]*, v. 19, n. 5, p. 1700–1716, 1998. a. DOI: 10.1137/S1064827595293582.

AAVATSMARK, I.; BARKVE, T.; BØE; MANNSETH, T. **Discretization on unstructured grids for inhomogeneous, anisotropic media. Part II: Discussion and numerical results**. **SIAM Journal of Scientific Computing**, 1998. b. DOI: 10.1137/S1064827595293594.

AAVATSMARK, I.; BARKVE, T.; MANNSETH, T. Control-Volume Discretization Methods for 3D Quadrilateral Grids in Inhomogeneous, Anisotropic Reservoirs. **SPE Journal**, *[S. l.]*, v. 3, n. 2, p. 146–149, 1998. DOI: 10.2118/38000-pa.

AAVATSMARK, I.; EIGESTAD, G. T.; KLAUSEN, R. A. Numerical Convergence of the MPFA O-Method for General Quadrilateral Grids in Two and Three Dimensions. *In*: **Compatible Spatial Discretizations**. New York, NY, NY: Springer New York, 2007. p. 1–21. DOI: 10.1007/0-387-38034-5_1.

AAVATSMARK, I.; EIGESTAD, G. T.; MALLISON, B. T.; NORDBOTTEN, J. M. A compact multipoint flux approximation method with improved robustness. **Numerical Methods for Partial Differential Equations**, *[S. l.]*, v. 24, n. 5, p. 1329–1360, 2008. DOI: 10.1002/num.20320.

AAVATSMARK, I.; REISO, E.; REME, H.; TEIGLAND, R. MPFA for Faults and Local Refinements in 3D Quadrilateral Grids With Application to Field Simulations. *In*: ALL DAYS 2001, **Anais** [...]. : SPE, 2001. DOI: 10.2118/66356-MS.

ANDREIANOV, B.; BOYER, F.; HUBERT, F. Discrete duality finite volume schemes for Leray−Lions−type elliptic problems on general 2D meshes. **Numerical Methods for Partial Differential Equations**, *[S. l.]*, v. 23, n. 1, p. 145–195, 2007. DOI: 10.1002/num.20170.

ARFKEN, G. B.; WEBER, H. J.; HARRIS, F. E. **Mathematical Methods for Physicists**. [s.l.] : Elsevier, 2013. DOI: 10.1016/C2009-0-30629-7.

AZIZ, K.; SETTARE, A. **Petroleum Reservoir Simulation**. New York:

Applied Science Publishers, 1979.

BALIGA, B. R.; PATANKAR, S. V. A new finite-element formulation for convection-diffusion problems. **Numerical Heat Transfer**, *[S. l.]*, v. 3, n. 4, p. 393–409, 1980. DOI: 10.1080/01495728008961767.

BALIGA, B. R.; PATANKAR, S. V. Elliptic systems: Finite-element method II. *In*: MINKOWYCZ, W. J. (org.). **Handbook of Numerical Heat Transfer**. [s.l.] : John Wilew & Sons, 1988. p. 421–455.

BARENBLATT, G. I.; ZHELTOV, I. P.; KOCHINA, I. N. Basic concepts in the theory of seepage of homogeneous liquids in fissured rocks [strata]. **Journal of Applied Mathematics and Mechanics**, *[S. l.]*, v. 24, n. 5, p. 1286–1303, 1960. DOI: 10.1016/0021-8928(60)90107-6.

BEAR, J. Dynamics of Fluids in Porous Media. *[S. l.]*, 1972.

BERRE, I. et al. Verification benchmarks for single-phase flow in three-dimensional fractured porous media. **Advances in Water Resources**, *[S. l.]*, v. 147, p. 103759, 2021. DOI: 10.1016/j.advwatres.2020.103759.

BERRE, I.; DOSTER, F.; KEILEGAVLEN, E. Flow in Fractured Porous Media: A Review of Conceptual Models and Discretization Approaches. **Transport in Porous Media**, *[S. l.]*, v. 130, n. 1, p. 215–236, 2019. DOI: 10.1007/s11242-018-1171-6.

BEYDOUN, Z. R. Arabian plate oil and gas: Why so rich and so prolific? **Episodes**, *[S. l.]*, v. 21, n. 2, p. 74–81, 1998. DOI: 10.18814/epiiugs/1998/v21i2/001.

BURMAN, E.; ERN, A. Principe du maximum discret pour des approximations de Galerkin du Laplacien sur des maillages quelconques. **Comptes Rendus Mathematique**, *[S. l.]*, v. 338, n. 8, p. 641–646, 2004. DOI: 10.1016/j.crma.2004.02.010.

CANCÈS, C.; CATHALA, M.; LE POTIER, C. Monotone corrections for generic cell-centered finite volume approximations of anisotropic diffusion equations. **Numerische Mathematik**, *[S. l.]*, v. 125, n. 3, p. 387–417, 2013. DOI: 10.1007/s00211-013-0545-5.

CARVALHO, D. K. E.; WILLMERSDORF, R. B.; LYRA, P. R. M. Some results on the accuracy of an edge-based finite volume formulation for the solution of elliptic problems in non-homogeneous and non-isotropic media. **International Journal for Numerical Methods in Fluids**, *[S. l.]*, v. 61, n. 3, p. 237–254, 2009. DOI: 10.1002/fld.1948.

CAVALCANTE, T. M.; CONTRERAS, F. R. L.; LYRA, P. R. M.; CARVALHO, D. K. E. A multipoint flux approximation with diamond stencil finite

volume scheme for the two-dimensional simulation of fluid flows in naturally fractured reservoirs using a hybrid-grid method. **International Journal for Numerical Methods in Fluids**, *[S. l.]*, v. 92, n. 10, p. 1322–1351, 2020. DOI: 10.1002/fld.4829.

CAVALCANTE, T. M.; LIRA FILHO, R. J. M.; SOUZA, A. C. R.; CARVALHO, D. K. E.; LYRA, P. R. M. A Multipoint Flux Approximation with a Diamond Stencil and a Non-Linear Defect Correction Strategy for the Numerical Solution of Steady State Diffusion Problems in Heterogeneous and Anisotropic Media Satisfying the Discrete Maximum Principle. **Journal of Scientific Computing**, *[S. l.]*, v. 93, n. 2, p. 42, 2022. DOI: 10.1007/s10915-022-01978-6.

CHEN, Q. Y.; WAN, J.; YANG, Y.; MIFFLIN, R. T. Enriched multi-point flux approximation for general grids. **Journal of Computational Physics**, *[S. l.]*, v. 227, n. 3, p. 1701–1721, 2008. DOI: 10.1016/j.jcp.2007.09.021.

CHEN, Z.; HUAN, G.; MA, Y. **Computational Methods for Multiphase Flows in Porous Media**. [s.l.] : Society for Industrial and Applied Mathematics, 2006. DOI: 10.1137/1.9780898718942.

CHILDS, H. et al. VisIt: An End-User Tool for Visualizing and Analyzing Very. *In*: **High Performance Visualization**. [s.l.] : Chapman and Hall/CRC, 2012. p. 395–410. DOI: 10.1201/b12985-29.

CIARLET, P. ..; RAVIART, P. A. Maximum principle and uniform convergence for the finite element method. **Computer Methods in Applied Mechanics and Engineering**, *[S. l.]*, v. 2, n. 1, p. 17–31, 1973. DOI: 10.1016/0045-7825(73)90019-4.

CIARLET, P. G. **The Finite Element Method for Elliptic Problems**. [s.l.] : Society for Industrial and Applied Mathematics, 2002. v. 40 DOI: 10.1137/1.9780898719208.

CONTRERAS, F. R. L.; LYRA, P. R. M.; SOUZA, M. R. A.; CARVALHO, D. K. E. A cell-centered multipoint flux approximation method with a diamond stencil coupled with a higher order finite volume method for the simulation of oil-water displacements in heterogeneous and anisotropic petroleum reservoirs. **Computers and Fluids**, *[S. l.]*, v. 127, p. 1–16, 2016. DOI: 10.1016/j.compfluid.2015.11.013.

COREY, A. T. The interrelation between gas and oil relative permeabilities. **Prod. Month.**, *[S. l.]*, v. 19, p. 38–41, 1954.

CROSS, M. Computational Galerkin methods. **Applied Mathematical Modelling**, Berlin, Heidelberg, v. 9, n. 3, p. 226, 1985. DOI: 10.1016/0307-904X(85)90012-5.

CRUMPTON, P. I.; SHAW, G. J.; WARE, A. F. Discretisation and multigrid solution of elliptic equations with mixed derivative terms and strongly discontinuous coefficients. **Journal of Computational Physics**, *[S. l.]*, v. 116, n. 2, p. 343–358, 1995. DOI: 10.1006/jcph.1995.1032.

DANILOV, A. A.; VASSILEVSKI, Y. V. A monotone nonlinear finite volume method for diffusion equations on conformal polyhedral meshes. **Russian Journal of Numerical Analysis and Mathematical Modelling**, *[S. l.]*, v. 24, n. 3, p. 207–227, 2009. DOI: 10.1515/RJNAMM.2009.014.

DARCY, H. **Les fontaines publiques de la ville de Dijon**. Paris.

DEVLOO, P.; TENG, W.; ZHANG, C. S. Multiscale Hybrid-Mixed Finite Element Method for Flow Simulation in Fractured Porous Media. **Computer Modeling in Engineering & Sciences**, *[S. l.]*, v. 119, n. 1, p. 145–163, 2019. DOI: 10.32604/cmes.2019.04812.

DONG, C.; KANG, T. A least squares based diamond scheme for anisotropic diffusion problems on polygonal meshes. **International Journal for Numerical Methods in Fluids**, *[S. l.]*, v. 93, n. 11, p. 3231–3253, 2021. DOI: 10.1002/fld.5031.

DONG, C.; KANG, T. A least squares based diamond scheme for 3D heterogeneous and anisotropic diffusion problems on polyhedral meshes. **Applied Mathematics and Computation**, *[S. l.]*, v. 418, p. 126847, 2022. DOI: 10.1016/j.amc.2021.126847.

DUISTERMAAT, J. J.; KOLK, J. A. C. Taylor Expansion in Several Variables. *In*: **Distributions**. Boston: Birkhäuser Boston, 2010. p. 59–63. DOI: 10.1007/978-0-8176-4675-2_6.

DURÁN, R. G. Mixed Finite Element Methods. *In*: **Lecture Notes in Mathematics**. [s.l.] : Springer, Berlin, Heidelberg, 2008. v. 1939p. 1–44. DOI: 10.1007/978-3-540-78319-0_1.

EDWARDS, M. G. M-Matrix Flux Splitting for General Full Tensor Discretization Operators on Structured and Unstructured Grids. **Journal of Computational Physics**, *[S. l.]*, v. 160, n. 1, p. 1–28, 2000. DOI: 10.1006/jcph.2000.6418.

EDWARDS, M. G.; ROGERS, C. F. Finite volume discretization with imposed flux continuity for the general tensor pressure equation. **Computational Geosciences**, *[S. l.]*, v. 2, n. 4, p. 259–290, 1998. DOI: 10.1023/A:1011510505406.

ERTEKIN, T.; ABOU-KASSEM, J. H.; KING, G. R. **Basic Applied Reservoir**

Simulation. Richardson: Society of Petroleum Engineers, 2001. DOI: 10.2118/9781555630898.

EWING, R. E. **The Mathematics of Reservoir Simulation**. [s.l.] : Society for Industrial and Applied Mathematics, 1983. DOI: 10.1137/1.9781611971071.

EYMARD, R.; HENRY, G.; HERBIN, R.; HUBERT, F.; KLÖFKORN, R.; MANZINI, G. 3D Benchmark on Discretization Schemes for Anisotropic Diffusion Problems on General Grids. **Springer Proceedings in Mathematics**, *[S. l.]*, v. 4, p. 895–930, 2011. DOI: 10.1007/978-3-642-20671-9_89.

FANCHI, J. R. **Principles of Applied Reservoir Simulation**. [s.l.] : Gulf Professional Publishing, 2006. DOI: 10.1016/B978-0-7506-7933-6.X5000-4.

FOX, R. W.; PRITCHARD, P. J.; MCDONALD, A. T. **Introdução à Mecânica dos Fluidos**. 7. ed. Rio de Janeiro: LTC, 2010.

GAO, Z.; WU, J. A linearity-preserving cell-centered scheme for the heterogeneous and anisotropic diffusion equations on general meshes. **International Journal for Numerical Methods in Fluids**, *[S. l.]*, v. 67, n. 12, p. 2157–2183, 2011. DOI: 10.1002/fld.2496.

GAO, Z.; WU, J. A second-order positivity-preserving finite volume scheme for diffusion equations on general meshes. **SIAM Journal on Scientific Computing**, *[S. l.]*, v. 37, n. 1, p. A420–A438, 2015. DOI: 10.1137/140972470.

GEUZAINE, C.; REMACLE, J. F. Gmsh: A 3-D finite element mesh generator with built-in pre- and post-processing facilities. **International Journal for Numerical Methods in Engineering**, *[S. l.]*, v. 79, n. 11, p. 1309–1331, 2009. DOI: 10.1002/nme.2579.

GILMAN, J. R.; KAZEMI, H. Improvements in Simulation of Naturally Fractured Reservoirs. **Society of Petroleum Engineers Journal**, *[S. l.]*, v. 23, n. 04, p. 695–707, 1983. DOI: 10.2118/10511-PA.

HAJIBEYGI, Hadi; KARVOUNIS, Dimitris; JENNY, Patrick. A hierarchical fracture model for the iterative multiscale finite volume method. **Journal of Computational Physics**, *[S. l.]*, v. 230, n. 24, p. 8729–8743, 2011. DOI: 10.1016/j.jcp.2011.08.021.

HERBIN, R.; HUBERT, F. Benchmark on Discretization Schemes for Anisotropic Diffusion Problems on General Grids. *In*: **Finite volumes for complex applications V**. [s.l: s.n.]. p. 659–692.

HERMELINE, F. Approximation of 2-D and 3-D diffusion operators with

variable full tensor coefficients on arbitrary meshes. **Computer Methods in Applied Mechanics and Engineering**, *[S. l.]*, v. 196, n. 21–24, p. 2497–2526, 2007. DOI: 10.1016/j.cma.2007.01.005.

HERMELINE, F. A finite volume method for approximating 3D diffusion operators on general meshes. **Journal of Computational Physics**, *[S. l.]*, v. 228, n. 16, p. 5763–5786, 2009. DOI: 10.1016/j.jcp.2009.05.002.

HOSSEINIMEHR, Mousa; TOMALA, Janio Piguave; VUIK, Cornelis; KOBAISI, Mohammed Al; HAJIBEYGI, Hadi. Projection-based embedded discrete fracture model (pEDFM) for flow and heat transfer in real-field geological formations with hexahedral corner-point grids. **Advances in Water Resources**, *[S. l.]*, v. 159, p. 104091, 2022. DOI: 10.1016/j.advwatres.2021.104091.

HOTEIT, Hussein; FIROOZABADI, Abbas. An efficient numerical model for incompressible two-phase flow in fractured media. **Advances in Water Resources**, *[S. l.]*, v. 31, n. 6, p. 891–905, 2008. DOI: 10.1016/j.advwatres.2008.02.004.

HSU, C. J. Numerical Heat Transfer and Fluid Flow. **Nuclear Science and Engineering**, New York, v. 78, n. 2, p. 196–197, 1981. DOI: 10.13182/NSE81-A20112.

ISLAM, M. Rafiqul. Overview of Reservoir Simulation of Unconventional Reservoirs. *In*: **Unconventional Gas Reservoirs**. [s.l.] : Elsevier, 2015. p. 487–547. DOI: 10.1016/B978-0-12-800390-9.00007-4.

JIANG, J.; YOUNIS, R. M. An improved projection-based embedded discrete fracture model (pEDFM) for multiphase flow in fractured reservoirs. **Advances in Water Resources**, *[S. l.]*, v. 109, p. 267–289, 2017. DOI: 10.1016/j.advwatres.2017.09.017.

KARIMI-FARD, M.; DURLOFSKY, L. J.; AZIZ, K. An efficient discrete-fracture model applicable for general-purpose reservoir simulators. **SPE Journal**, *[S. l.]*, v. 9, n. 2, p. 227–236, 2004. DOI: 10.2118/88812-PA.

KAZEMI, H.; MERRILL, L. S.; PORTERFIELD, K. L.; ZEMAN, P. R. Numerical Simulation of Water-Oil Flow in Naturally Fractured Reservoirs. **Society of Petroleum Engineers Journal**, *[S. l.]*, v. 16, n. 06, p. 317–326, 1976. DOI: 10.2118/5719-PA.

KEILEGAVLEN, E.; AAVATSMARK, I. Monotonicity for MPFA methods on triangular grids. **Computational Geosciences**, *[S. l.]*, v. 15, n. 1, p. 3–16, 2011. DOI: 10.1007/s10596-010-9191-5.

KLAUSEN, R. A.; EIGESTAD, G. T. Multi Point Flux Approximations and Finite Element Methods; Practical Aspects of Discontinuous Media. *In*: ECMOR IX -

9TH EUROPEAN CONFERENCE ON THE MATHEMATICS OF OIL RECOVERY 2004, **Anais** [...]. : European Association of Geoscientists & Engineers, 2004. DOI: 10.3997/2214-4609-pdb.9.B003.

KOROTOV, S.; KŘÍŽEK, M.; NEITTAANMÄKI, P. Weakened acute type condition for tetrahedral triangulations and the discrete maximum principle. **Mathematics of Computation**, *[S. l.]*, v. 70, n. 233, p. 107–119, 2000. DOI: 10.1090/S0025-5718-00-01270-9.

KOZDON, J. E.; MALLISON, B. T.; GERRITSEN, M. G. Multidimensional upstream weighting for multiphase transport in porous media. **Computational Geosciences**, *[S. l.]*, v. 15, n. 3, p. 399–419, 2011. DOI: 10.1007/s10596-010-9211-5.

KUZMIN, D.; SHASHKOV, M. J.; SVYATSKIY, D. A constrained finite element method satisfying the discrete maximum principle for anisotropic diffusion problems. **Journal of Computational Physics**, *[S. l.]*, v. 228, n. 9, p. 3448–3463, 2009. DOI: 10.1016/j.jcp.2009.01.031.

LAI, X.; SHENG, Z.; YUAN, G. Monotone Finite Volume Scheme for Three Dimensional Diffusion Equation on Tetrahedral Meshes. **Communications in Computational Physics**, *[S. l.]*, v. 21, n. 1, p. 162–181, 2017. DOI: 10.4208/cicp.220415.090516a.

LE POTIER, C. Schéma volumes finis monotone pour des opérateurs de diffusion fortement anisotropes sur des maillages de triangles non structurés. **Comptes Rendus Mathematique**, *[S. l.]*, v. 341, n. 12, p. 787–792, 2005. DOI: 10.1016/j.crma.2005.10.010.

LE POTIER, C. A nonlinear finite volume scheme satisfying maximum and minimum principles for diffusion operators. **International Journal on Finite Volumes**, *[S. l.]*, p. 1–20, 2009.

LEE, S. H.; LOUGH, M. F.; JENSEN, C. L. Hierarchical modeling of flow in naturally fractured formations with multiple length scales. **Water Resources Research**, *[S. l.]*, v. 37, n. 3, p. 443–455, 2001. DOI: 10.1029/2000WR900340.

LI, L.; LEE, S. H. Efficient field-scale simulation of black oil in a naturally fractured reservoir through discrete fracture networks and homogenized media. **SPE Reservoir Evaluation and Engineering**, *[S. l.]*, v. 11, n. 4, p. 750–758, 2008. DOI: 10.2118/103901-pa.

LIMA, P.; DEVLOO, P. R. B.; VILLEGAS, J. Multi-scale meshing for 3D discrete fracture networks. *In*: PROCEEDINGS OF THE XLI IBERO-LATIN-

AMERICAN CONGRESS ON COMPUTATIONAL METHODS IN ENGINEERING, ABMEC 2020, Foz do Iguaçu, PR, Brazil. **Anais** [...]. Foz do Iguaçu, PR, Brazil

LIRA FILHO, R. J. M.; SANTOS, S. R.; CAVALCANTE, T. M.; CONTRERAS, F. R. L.; LYRA, P. R. M.; CARVALHO, D. K. E. A linearity-preserving finite volume scheme with a diamond stencil for the simulation of anisotropic and highly heterogeneous diffusion problems using tetrahedral meshes. **Computers and Structures**, *[S. l.]*, v. 250, p. 106510, 2021. DOI: 10.1016/j.compstruc.2021.106510.

MAGOON, L. B. Petroleum System: Nature's Distribution System for Oil and Gas. *In*: **Encyclopedia of Energy**. [s.l.] : Elsevier, 2004. p. 823–836. DOI: 10.1016/B0-12-176480-X/00251-5.

MALISKA, C. R. **Transferência de Calor e Mecânica dos Fluidos Computacional**. Rio de Janeiro: LTC - Livros Técnicos e Científicos Editora S.A., 1995.

MANZOCCHI, T.; WALSH, J. J.; NELL, P.; YIELDING, G. Fault transmissibility multipliers for flow simulation models. **Petroleum Geoscience**, *[S. l.]*, v. 5, n. 1, p. 53–63, 1999. DOI: 10.1144/petgeo.5.1.53.

MARTIN, V.; JAFFRÉ, J.; ROBERTS, J. E. Modeling Fractures and Barriers as Interfaces for Flow in Porous Media. **SIAM Journal on Scientific Computing**, *[S. l.]*, v. 26, n. 5, p. 1667–1691, 2005. DOI: 10.1137/S1064827503429363.

MATTHÄI, Stephan K. Modeling Multiphase Flow in Fractured Porous Rock. **Department of Earth Sciences & Engineering, Imperial College London**, London, v. 24, n. 1, p. 45–51, 2018.

MOINFAR, A.; NARR, W.; HUI, M. H.; MALLISON, B.; LEE, S. H. Comparison of Discrete-Fracture and Dual-Permeability Models for Multiphase Flow in Naturally Fractured Reservoirs. *In*: ALL DAYS 2011, **Anais** [...]. : SPE, 2011. DOI: 10.2118/142295-MS.

MOINFAR, A.; VARAVEI, A.; SEPEHRNOORI, K.; JOHNS, R. T. Development of an efficient embedded discrete fracture model for 3D compositional reservoir simulation in fractured reservoirs. **SPE Journal**, *[S. l.]*, v. 19, n. 2, p. 289–303, 2014. DOI: 10.2118/154246-PA.

MØYNER, O.; LIE, K. A. A multiscale two-point flux-approximation method. **Journal of Computational Physics**, *[S. l.]*, v. 275, p. 273–293, 2014. DOI: 10.1016/j.jcp.2014.07.003.

MUIR, B. L.; RABI BALIGA, B. Solution of three-dimensional convection-diffusion problems using tetrahedral elements and flow-oriented upwind interpolation

functions. **Numerical Heat Transfer**, *[S. l.]*, v. 9, n. 2, p. 143–162, 1986. DOI: 10.1080/10407788608913470.

NILSEN, H. M.; LIE, K. A.; NATVIG, J. R. Accurate modeling of faults by multipoint, mimetic, and mixed methods. **SPE Journal**, *[S. l.]*, v. 17, n. 2, p. 568–579, 2012. DOI: 10.2118/149690-PA.

PAL, M.; EDWARDS, M. Flux-Splitting Schemes for Improved Monotonicity of Discrete Solutions of Elliptic Equations with Highly Anisotropic Coefficients. **European Conference on Computational Fluid Dynamics**, *[S. l.]*, n. December 2013, 2006.

PAL, M.; EDWARDS, M. G. Quasimonotonic continuous Darcy-flux approximation for general 3D grids of any element type. **SPE Reservoir Simulation Symposium Proceedings**, *[S. l.]*, n. 1, p. 473–486, 2007. DOI: 10.2118/106486-ms.

PAL, M.; EDWARDS, M. G. Non-linear flux-splitting schemes with imposed discrete maximum principle for elliptic equations with highly anisotropic coefficients. **International Journal for Numerical Methods in Fluids**, *[S. l.]*, v. 66, n. 3, p. 299–323, 2011. DOI: 10.1002/fld.2258.

PEACEMAN, D. W. Fundamentals of numerical reservoir simulation. Amsterdam, p. 175, 1977.

QUEIROZ, L. E. S.; SOUZA, M. R. A.; CONTRERAS, F. R. L.; LYRA, P. R. M.; CARVALHO, D. K. E. On the accuracy of a nonlinear finite volume method for the solution of diffusion problems using different interpolations strategies. **International Journal for Numerical Methods in Fluids**, *[S. l.]*, v. 74, n. 4, p. 270–291, 2014. DOI: 10.1002/fld.3850.

RAO, X.; CHENG, L.; CAO, R.; JIA, P.; LIU, H.; DU, X. A modified projection-based embedded discrete fracture model (pEDFM) for practical and accurate numerical simulation of fractured reservoir. **Journal of Petroleum Science and Engineering**, *[S. l.]*, v. 187, p. 106852, 2020. DOI: 10.1016/j.petrol.2019.106852.

RAVIART, P. A.; THOMAS, J. M. A mixed finite element method for 2-nd order elliptic problems. *In*: **Galligani I., Magenes E. (eds) Mathematical Aspects of Finite Element Methods. Lecture Notes in Mathematics, vol 606.** [s.l.] : Springer, Berlin, Heidelberg, 1977. p. 292–315. DOI: 10.1007/BFb0064470.

SANDVE, T. H.; BERRE, I.; NORDBOTTEN, J. M. An efficient multi-point flux approximation method for Discrete Fracture–Matrix simulations. **Journal of Computational Physics**, *[S. l.]*, v. 231, n. 9, p. 3784–3800, 2012. DOI:

10.1016/j.jcp.2012.01.023.

SHAKIBA, M.; SEPEHRNOORI, K. Using Embedded Discrete Fracture Model (EDFM) and Microseismic Monitoring Data to Characterize the Complex Hydraulic Fracture Networks. *In*: DAY 3 WED, SEPTEMBER 30, 2015 2015, **Anais** [...]. : SPE, 2015. p. 6215–6237. DOI: 10.2118/175142-MS.

STEIMBRUCH, A.; WINTERLE, P. **Geometria Analítica**. [s.l.] : Pearson Universidades, 1995.

SU, S.; DONG, Q.; WU, J. A decoupled and positivity-preserving discrete duality finite volume scheme for anisotropic diffusion problems on general polygonal meshes. **Journal of Computational Physics**, *[S. l.]*, v. 372, p. 773–798, 2018. DOI: 10.1016/j.jcp.2018.06.052.

ŢENE, M.; BOSMA, S. B. M.; AL KOBAISI, M. S.; HAJIBEYGI, H. Projection-based Embedded Discrete Fracture Model (pEDFM). **Advances in Water Resources**, *[S. l.]*, v. 105, p. 205–216, 2017. DOI: 10.1016/j.advwatres.2017.05.009.

THOMAS, L. K.; DIXON, T. N.; PIERSON, R. G. Fractured Reservoir Simulation. **Society of Petroleum Engineers Journal**, *[S. l.]*, v. 23, n. 01, p. 42–54, 1983. DOI: 10.2118/9305-PA.

ULEBERG, K.; KLEPPE, J. **Dual Porosity, Dual Permeability Formulation for Fractured Reservoir Simulation**. Stavanger.

VARGA, Richard S. On a Discrete Maximum Principle. **SIAM Journal on Numerical Analysis**, *[S. l.]*, v. 3, n. 2, p. 355–359, 1966. DOI: 10.1137/0703029.

WANG, L.; WANG, Y.; VUIK, C.; HAJIBEYGI, H. Accurate modeling and simulation of seepage in 3D heterogeneous fractured porous media with complex structures. **Computers and Geotechnics**, *[S. l.]*, v. 150, p. 104923, 2022. DOI: 10.1016/j.compgeo.2022.104923.

WANG, S.; HANG, X.; YUAN, G. A pyramid scheme for three-dimensional diffusion equations on polyhedral meshes. **Journal of Computational Physics**, *[S. l.]*, v. 350, p. 590–606, 2017. DOI: 10.1016/j.jcp.2017.08.060.

WARREN, J. E.; ROOT, P. J. The Behavior of Naturally Fractured Reservoirs. **Society of Petroleum Engineers Journal**, *[S. l.]*, v. 3, n. 03, p. 245–255, 1963. DOI: 10.2118/426-PA.

WILLARD GIBBS, J.; BIDWELL WILSON, E. Vector analysis: a text-book for the use of students of mathematics and physics. New Haven, p. 436, 1901.

WOLFF, M.; CAO, Y.; FLEMISCH, B.; HELMIG, R.; WOHLMUTH, B.

Multipoint flux approximation L-method in 3D: numerical convergence and application to two-phase flow through porous media. *In*: **Simulation of Flow in Porous Media**. [s.l.] : DE GRUYTER, 2013. p. 39–80. DOI: 10.1515/9783110282245.39.

WU, J.; GAO, Z. Interpolation-based second-order monotone finite volume schemes for anisotropic diffusion equations on general grids. **Journal of Computational Physics**, *[S. l.]*, v. 275, p. 569–588, 2014. DOI: 10.1016/j.jcp.2014.07.011.

YANG, D.; GAO, Z. A linearity-preserving vertex interpolation algorithm for cell-centered finite volume approximations of anisotropic diffusion problems. **International Journal of Numerical Methods for Heat and Fluid Flow**, *[S. l.]*, v. 30, n. 3, p. 1167–1188, 2020. DOI: 10.1108/HFF-04-2019-0354.

ZHAO, F.; SHENG, Z.; YUAN, G. A monotone combination scheme of diffusion equations on polygonal meshes. **ZAMM Zeitschrift fur Angewandte Mathematik und Mechanik**, *[S. l.]*, v. 100, n. 5, 2020. DOI: 10.1002/zamm.201900320.

APPENDIX A – INTERPOLATION EXPRESSIONS DERIVATION

This appendix presents the derivation of the weighting expressions used to turn Eq. (3.47) in a completely cell-centered formulation. Considering a node Q, the pressure value at it can be written as a weighted average of the values at the cells sharing Q. Idea which can be generically described by the following expression:

$$p_Q = \sum_{\hat{k} \in \widehat{\mathbb{Q}}} \omega_{\hat{k}} p_{\hat{k}} \tag{A.1}$$

in which $\widehat{\mathbb{Q}}$ is the set of cells sharing Q. The next subsections present some expressions to determine $\omega_{\hat{k}}$.

A.1 Linearity Preserving Explicit Weights Type 1 (LPEW1)

The first strategy is the natural extension, by analogy, to 3-D of the LPEW1 presented by Gao and Wu (2011), in 2-D. For this, in each tetrahedron sharing Q, we define a subregion delimited by 6 tetrahedrons, as shown in Figure A.1: $\hat{t}_1 = T_1T_2\hat{k}Q$, $\hat{t}_2 = T_2T_3\hat{k}Q$, $\hat{t}_3 = T_3T_4\hat{k}Q$, $\hat{t}_4 = T_4T_5\hat{k}Q$, $\hat{t}_5 = T_5T_6\hat{k}Q$ and $\hat{t}_6 = T_6T_1\hat{k}Q$, where T_1 is on the edge QI, T_2 is on the face QIK, T_3 is on the edge QK, T_4 is on the face QJK, T_5 is on the edge QJ, T_6 is on the face QIJ, where IJK is the opposite face to Q in the k-th tetrahedron sharing it (with a colocation point $\hat{k}$). The points I, J and K are named so that $\vec{N} = \left(\overrightarrow{JI} \times \overrightarrow{JK}\right)/2$ is the outward area vector of the face IJK. Then, we can also define, in the subregion shown in Figure A.1, the subfaces $\bar{k}_1 = T_1T_2Q$, $\bar{k}_2 = T_2T_3Q$, $\bar{k}_3 = T_3T_4Q$, $\bar{k}_4 = T_4T_5Q$, $\bar{k}_5 = T_5T_6Q$, $\bar{k}_6 = T_6T_1Q$. Beyond this, we also define the faces $\bar{Q}_1 = T_1T_2\hat{k}$, $\bar{Q}_2 = T_2T_3\hat{k}$, $\bar{Q}_3 = T_3T_4\hat{k}$, $\bar{Q}_4 = T_4T_5\hat{k}$, $\bar{Q}_5 = T_5T_6\hat{k}$ and $\bar{Q}_6 = T_6T_1\hat{k}$, in case of LPEW1. The neighbor cells sharing faces and the node Q with $\hat{k}$ are named as $\hat{o}_J$ (the neighbor cell sharing the face opposing vertex J), $\hat{o}_I$ (the neighbor cell sharing the face opposing vertex I), $\hat{o}_K$ (the neighbor cell sharing the face opposing vertex K), as shown in Figure A.2a.

All this defined, we can start the development of our explicit weighting by the divergence free imposition on the node Q through the following expression:

$$\sum_{\hat{k}\in\hat{\mathbb{Q}}} \mathrm{F}_{Q}^{\hat{k}} = 0 \tag{A.2}$$

where $\mathrm{F}_{Q}^{\hat{k}}$ is defined according to the subregion definition shown in Figure A.1. In this case, $\mathrm{F}_{Q}^{\hat{k}}$ is defined as:

$$\mathrm{F}_{Q}^{\hat{k}} = \mathrm{F}_{\bar{Q}_1}^{\hat{k}} + \mathrm{F}_{\bar{Q}_2}^{\hat{k}} + \mathrm{F}_{\bar{Q}_3}^{\hat{k}} + \mathrm{F}_{\bar{Q}_4}^{\hat{k}} + \mathrm{F}_{\bar{Q}_5}^{\hat{k}} + \mathrm{F}_{\bar{Q}_6}^{\hat{k}} \tag{A.3}$$

Figure A.1 - LPEW1 subregion comprising node Q in $\hat{k}$ (the k-th cell sharing Q).

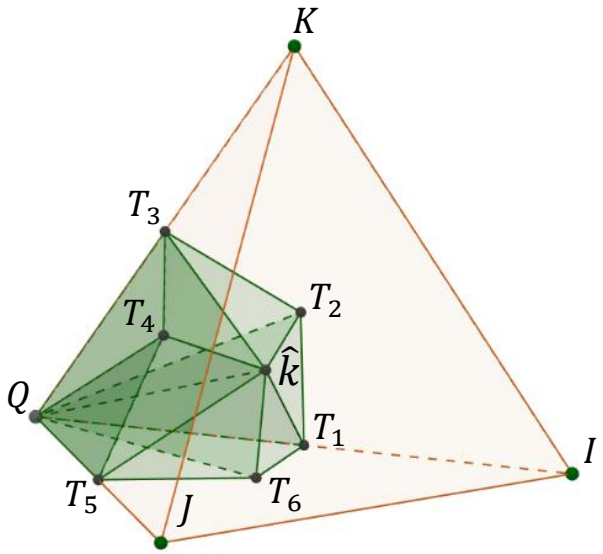

Source: The author (2023).

where $\mathrm{F}_{\bar{Q}_1}^{\hat{k}} = \vec{v}_\alpha \cdot \vec{S}_Q^{\hat{t}_1}$ is the flux through the face $\bar{Q}_1$, which can to be defined, disregarding phase mobility (see Assumption A4 in section 2.1), analogously to Eq. (3.32), as:

$$\mathrm{F}_{\bar{Q}_1}^{\hat{k}} = \frac{1}{3\Omega_{\hat{t}_1}} \mathbf{K}_{\hat{k}} \left[\vec{S}_{T_1}^{\hat{t}_1}(p_{T_1} - p_Q) + \vec{S}_{T_2}^{\hat{t}_1}(p_{T_2} - p_Q) + \vec{S}_{\hat{k}}^{\hat{t}_1}(p_{\hat{k}} - p_Q) \right] \cdot \vec{S}_Q^{\hat{t}_1} \tag{A.4}$$

where $\vec{S}_Q^{\hat{t}_1}$ is the outward area vector of the opposite face to the node Q (analogously to other vertices) in tetrahedron $\hat{t}_1$ (Figure A.1) and $\Omega_{\hat{t}_1}$ is the volume of the tetrahedron $\hat{t}_1$. Note that, since we are going to define the fluid pressure at the vertices (p_I, p_J, p_K) from

the fluid pressure at the grid cells ($p_{\hat{k}}$), we disregard the gravity effects in this divergence free imposition and just consider the flux in consequence of p. The equation above can be simplified as:

$$\mathrm{F}_{\bar{Q}_1}^{\hat{k}} = \xi_{T_1}^{\hat{k},1}\left(p_{T_1} - p_Q\right) + \xi_{T_2}^{\hat{k},1}\left(p_{T_2} - p_Q\right) + \xi_{\hat{k}}^{\hat{k},1}\left(p_{\hat{k}} - p_Q\right) \tag{A.5}$$

where:

$$\xi_{T_j}^{\hat{k},i} = \frac{\left(\vec{S}_Q^{\hat{t}_i}\right)^T \mathbf{K}_{\hat{k}} \vec{S}_{T_j}^{\hat{t}_i}}{3\Omega_{\hat{t}_i}};\ \ \xi_{\hat{k}}^{\hat{k},i} = \frac{\left(\vec{S}_Q^{\hat{t}_i}\right)^T \mathbf{K}_{\hat{k}} \vec{S}_{\hat{k}}^{\hat{t}_i}}{3\Omega_{\hat{t}_i}};\ \ i,j = 1 \ldots 6 \tag{A.6}$$

Figure A.2 - Neighbor cells sharing faces and node Q with $\hat{k}$. (a) $\hat{o}_I$, $\hat{o}_J$ and $\hat{o}_K$. (b) Sketch of tetrahedra participating in flux continuity imposition on faces $\bar{k}_1$ and $\bar{k}_2$.

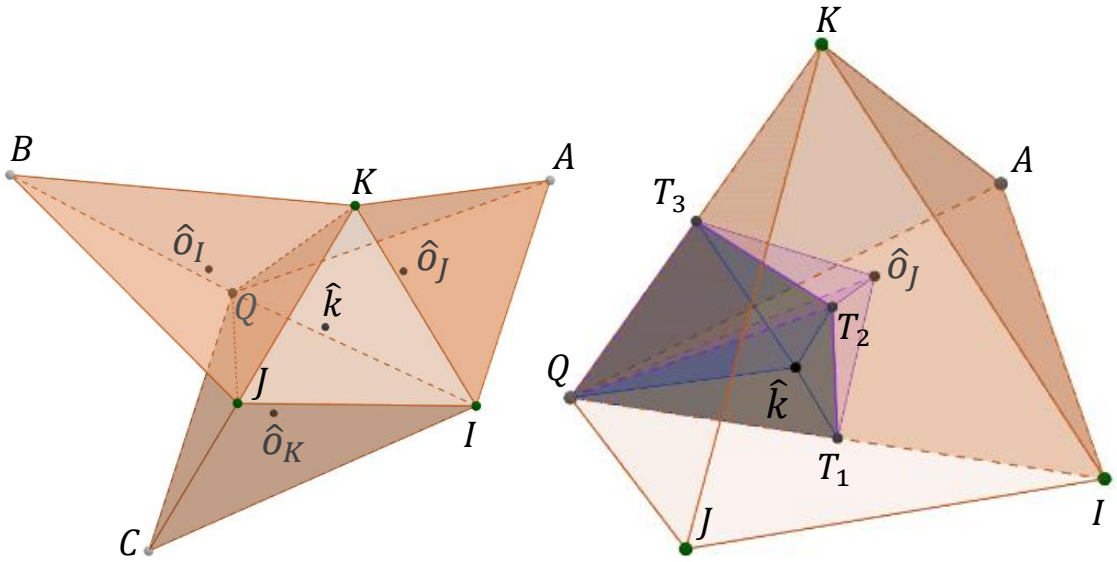

Source: The author (2023).

Writing the same expression for $\bar{Q}_2$ to $\bar{Q}_6$, we have:

$$\begin{cases} \mathrm{F}_{\bar{Q}_1}^{\hat{k}} = \xi_{T_1}^{\hat{k},1}\left(p_{T_1} - p_Q\right) + \xi_{T_2}^{\hat{k},1}\left(p_{T_2} - p_Q\right) + \xi_{\hat{k}}^{\hat{k},1}\left(p_{\hat{k}} - p_Q\right) \\ \mathrm{F}_{\bar{Q}_2}^{\hat{k}} = \xi_{T_2}^{\hat{k},2}\left(p_{T_2} - p_Q\right) + \xi_{T_3}^{\hat{k},2}\left(p_{T_3} - p_Q\right) + \xi_{\hat{k}}^{\hat{k},2}\left(p_{\hat{k}} - p_Q\right) \\ \mathrm{F}_{\bar{Q}_3}^{\hat{k}} = \xi_{T_3}^{\hat{k},3}\left(p_{T_3} - p_Q\right) + \xi_{T_4}^{\hat{k},3}\left(p_{T_4} - p_Q\right) + \xi_{\hat{k}}^{\hat{k},3}\left(p_{\hat{k}} - p_Q\right) \\ \mathrm{F}_{\bar{Q}_4}^{\hat{k}} = \xi_{T_4}^{\hat{k},4}\left(p_{T_4} - p_Q\right) + \xi_{T_5}^{\hat{k},4}\left(p_{T_5} - p_Q\right) + \xi_{\hat{k}}^{\hat{k},4}\left(p_{\hat{k}} - p_Q\right) \\ \mathrm{F}_{\bar{Q}_5}^{\hat{k}} = \xi_{T_5}^{\hat{k},5}\left(p_{T_5} - p_Q\right) + \xi_{T_6}^{\hat{k},5}\left(p_{T_6} - p_Q\right) + \xi_{\hat{k}}^{\hat{k},5}\left(p_{\hat{k}} - p_Q\right) \\ \mathrm{F}_{\bar{Q}_6}^{\hat{k}} = \xi_{T_6}^{\hat{k},6}\left(p_{T_6} - p_Q\right) + \xi_{T_1}^{\hat{k},6}\left(p_{T_1} - p_Q\right) + \xi_{\hat{k}}^{\hat{k},6}\left(p_{\hat{k}} - p_Q\right) \end{cases} \tag{A.7}$$

Summing these 6 fluxes, following Eq. (A.3), and rewriting the expression in the matrix form, we have the expression for $\mathrm{F}_Q^{\hat{k}}$ to be substituted in Eq. (A.2):

$$\mathrm{F}_Q^{\hat{k}} = \left[\mathbf{A}^{\hat{k}}\right]^T \begin{bmatrix} p_{T_1} - p_Q \\ p_{T_2} - p_Q \\ p_{T_3} - p_Q \\ p_{T_4} - p_Q \\ p_{T_5} - p_Q \\ p_{T_6} - p_Q \end{bmatrix} + \mathcal{C}^{\hat{k}}\left(p_{\hat{k}} - p_Q\right) \tag{A.8}$$

where:

$$\mathbf{A}^{\hat{k}} = \begin{bmatrix} \xi_{T_1}^{\hat{k},1} + \xi_{T_1}^{\hat{k},6} \\ \xi_{T_2}^{\hat{k},1} + \xi_{T_2}^{\hat{k},2} \\ \xi_{T_3}^{\hat{k},2} + \xi_{T_3}^{\hat{k},3} \\ \xi_{T_4}^{\hat{k},3} + \xi_{T_4}^{\hat{k},4} \\ \xi_{T_5}^{\hat{k},4} + \xi_{T_5}^{\hat{k},5} \\ \xi_{T_6}^{\hat{k},5} + \xi_{T_6}^{\hat{k},6} \end{bmatrix}; \; \mathcal{C}^{\hat{k}} = \sum_{i=1}^{6} \xi_{\hat{k}}^{\hat{k},i} \tag{A.9}$$

However, Eq. (A.8) is still not a cell-centered expression to be substituted in Eq. (A.2). Then, to eliminate these auxiliary variables p_{T_i} in Eq. (A.8), it is necessary to impose the flux continuity condition on the subfaces $\bar{k}_1$ to $\bar{k}_6$.

For the face $\bar{k}_1 = T_1T_2Q$ (see Figure A.2b), for example, the continuity imposition can be made based on the construction of the tetrahedra $\hat{k}T_1T_2Q$ and $\hat{o}_JT_1T_2Q$. Thus, it is possible to determine the expressions for the flow through the face $\bar{k}_1$ with respect to both tetrahedra, based in Eq. (3.40) and Eq. (3.41):

$$\vec{v}_\alpha \cdot \vec{N}_{\bar{k}_1} = \frac{1}{2h_{\hat{k}}^{\bar{k}_1}\left|\vec{N}_{\bar{k}_1}\right|}\left[\left(\frac{\langle \vec{\tau}_{\bar{k}_1}^{QT_1}, \overrightarrow{\hat{k}Q}\rangle}{\left|\vec{N}_{\bar{k}_1}\right|^2}\vec{N}_{\bar{k}_1}^T\mathbf{K}_{\hat{k}}\vec{N}_{\bar{k}_1} - \frac{h_{\hat{k}}^{\bar{k}_1}}{\left|\vec{N}_{\bar{k}_1}\right|}\vec{N}_{\bar{k}_1}^T\mathbf{K}_{\hat{k}}\vec{\tau}_{\bar{k}_1}^{QT_1}\right)\left(p_Q - p_{T_2}\right) - 2\vec{N}_{\bar{k}_1}^T\mathbf{K}_{\hat{k}}\vec{N}_{\bar{k}_1}\left(p_Q - p_{\hat{k}}\right) + \left(\frac{\langle \vec{\tau}_{\bar{k}_1}^{QT_2}, \overrightarrow{\hat{k}Q}\rangle}{\left|\vec{N}_{\bar{k}_1}\right|^2}\vec{N}_{\bar{k}_1}^T\mathbf{K}_{\hat{k}}\vec{N}_{\bar{k}_1} - \frac{h_{\hat{k}}^{\bar{k}_1}}{\left|\vec{N}_{\bar{k}_1}\right|}\vec{N}_{\bar{k}_1}^T\mathbf{K}_{\hat{k}}\vec{\tau}_{\bar{k}_1}^{QT_2}\right)\left(p_{T_1} - p_Q\right)\right] \tag{A.10}$$

and:

$$\vec{v}_\alpha \cdot \vec{N}_{\bar{k}_1} = \frac{1}{2h_{\hat{o}_J}^{\bar{k}_1}\left|\vec{N}_{\bar{k}_1}\right|}\left[\left(\frac{\langle \vec{\tau}_{\bar{k}_1}^{QT_1}, \overrightarrow{Q\hat{o}_J}\rangle}{\left|\vec{N}_{\bar{k}_1}\right|^2}\vec{N}_{\bar{k}_1}^T\mathbf{K}_{\hat{o}_J}\vec{N}_{\bar{k}_1} - \frac{h_{\hat{o}_J}^{\bar{k}_1}}{\left|\vec{N}_{\bar{k}_1}\right|}\vec{N}_{\bar{k}_1}^T\mathbf{K}_{\hat{o}_J}\vec{\tau}_{\bar{k}_1}^{QT_1}\right)\left(p_Q - p_{T_2}\right) - 2\vec{N}_{\bar{k}_1}^T\mathbf{K}_{\hat{o}_J}\vec{N}_{\bar{k}_1}\left(p_{\hat{o}_J} - p_Q\right) + \left(\frac{\langle \vec{\tau}_{\bar{k}_1}^{QT_2}, \overrightarrow{Q\hat{o}_J}\rangle}{\left|\vec{N}_{\bar{k}_1}\right|^2}\vec{N}_{\bar{k}_1}^T\mathbf{K}_{\hat{o}_J}\vec{N}_{\bar{k}_1} - \frac{h_{\hat{o}_J}^{\bar{k}_1}}{\left|\vec{N}_{\bar{k}_1}\right|}\vec{N}_{\bar{k}_1}^T\mathbf{K}_{\hat{o}_J}\vec{\tau}_{\bar{k}_1}^{QT_2}\right)\left(p_{T_1} - p_Q\right)\right] \tag{A.11}$$

with $\vec{N}_{\bar{k}_1}$ being outward from $\hat{k}$ and $\vec{\tau}_{\bar{k}_1}^{QT_j}$ (with $j = 1,2$) being defined as indicated in Eq. (3.37) and subsequent text. The continuity imposition would be made by equaling the right-hand sides of Eq. (A.10) and Eq. (A.11). These expressions above can be written, generically, for the subface $\bar{k}_i = T_iT_jQ$, shared by the cells $\hat{k}$ and $\hat{o}_\beta$, as:

$$\vec{v}_\alpha \cdot \vec{N}_{\bar{k}_i} = \frac{1}{2h_{\hat{k}}^{\bar{k}_i}\left|\vec{N}_{\bar{k}_i}\right|}\left[\left(\frac{\langle \vec{\tau}_{\bar{k}_i}^{QT_i}, \overrightarrow{\hat{k}Q}\rangle}{\left|\vec{N}_{\bar{k}_i}\right|^2}\vec{N}_{\bar{k}_i}^T\mathbf{K}_{\hat{k}}\vec{N}_{\bar{k}_i} - \frac{h_{\hat{k}}^{\bar{k}_i}}{\left|\vec{N}_{\bar{k}_i}\right|}\vec{N}_{\bar{k}_i}^T\mathbf{K}_{\hat{k}}\vec{\tau}_{\bar{k}_i}^{QT_i}\right)\left(p_Q - p_{T_j}\right) - 2\vec{N}_{\bar{k}_i}^T\mathbf{K}_{\hat{k}}\vec{N}_{\bar{k}_i}\left(p_Q - p_{\hat{k}}\right) + \left(\frac{\langle \vec{\tau}_{\bar{k}_i}^{QT_j}, \overrightarrow{\hat{k}Q}\rangle}{\left|\vec{N}_{\bar{k}_i}\right|^2}\vec{N}_{\bar{k}_i}^T\mathbf{K}_{\hat{k}}\vec{N}_{\bar{k}_i} - \frac{h_{\hat{k}}^{\bar{k}_i}}{\left|\vec{N}_{\bar{k}_i}\right|}\vec{N}_{\bar{k}_i}^T\mathbf{K}_{\hat{k}}\vec{\tau}_{\bar{k}_i}^{QT_j}\right)\left(p_{T_i} - p_Q\right)\right] \tag{A.12}$$

and:

$$\vec{v}_\alpha \cdot \vec{N}_{\bar{k}_i} = \frac{1}{2h_{\hat{o}_\beta}^{\bar{k}_i}\left|\vec{N}_{\bar{k}_i}\right|}\left[\left(\frac{\langle \vec{\tau}_{\bar{k}_i}^{QT_i}, \overrightarrow{Q\hat{o}_\beta}\rangle}{\left|\vec{N}_{\bar{k}_i}\right|^2}\vec{N}_{\bar{k}_i}^T\mathbf{K}_{\hat{o}_\beta}\vec{N}_{\bar{k}_i} - \frac{h_{\hat{o}_\beta}^{\bar{k}_i}}{\left|\vec{N}_{\bar{k}_i}\right|}\vec{N}_{\bar{k}_i}^T\mathbf{K}_{\hat{o}_\beta}\vec{\tau}_{\bar{k}_i}^{QT_i}\right)\left(p_Q - p_{T_j}\right) - 2\vec{N}_{\bar{k}_i}^T\mathbf{K}_{\hat{o}_\beta}\vec{N}_{\bar{k}_i}\left(p_{\hat{o}_\beta} - p_Q\right) + \left(\frac{\langle \vec{\tau}_{\bar{k}_i}^{QT_j}, \overrightarrow{Q\hat{o}_\beta}\rangle}{\left|\vec{N}_{\bar{k}_i}\right|^2}\vec{N}_{\bar{k}_i}^T\mathbf{K}_{\hat{o}_\beta}\vec{N}_{\bar{k}_i} - \frac{h_{\hat{o}_\beta}^{\bar{k}_i}}{\left|\vec{N}_{\bar{k}_i}\right|}\vec{N}_{\bar{k}_i}^T\mathbf{K}_{\hat{o}_\beta}\vec{\tau}_{\bar{k}_i}^{QT_j}\right)\left(p_{T_i} - p_Q\right)\right] \tag{A.13}$$

By equaling the right-hand sides of Eq. (A.12) and Eq. (A.13), and with some algebraic manipulation:

$$\begin{aligned}&\left[\frac{\langle \vec{\tau}_{\bar{k}_i}^{QT_j}, \overrightarrow{\hat{k}Q}\rangle}{2h_{\hat{k}}^{\bar{k}_i}\left|\vec{N}_{\bar{k}_i}\right|}K_{\hat{k}\bar{k}_i}^n - \frac{\langle \vec{\tau}_{\bar{k}_i}^{QT_j}, \overrightarrow{Q\hat{o}_\beta}\rangle}{2h_{\hat{o}_\beta}^{\bar{k}_i}\left|\vec{N}_{\bar{k}_i}\right|}K_{\hat{o}_\beta\bar{k}_i}^n - \frac{1}{2}K_{\hat{k}\bar{k}_i}^{QT_j} + \frac{1}{2}K_{\hat{o}_\beta\bar{k}_i}^{QT_j}\right]\left(p_{T_i} - p_Q\right)\\ &- \left[\frac{\langle \vec{\tau}_{\bar{k}_i}^{QT_i}, \overrightarrow{\hat{k}Q}\rangle}{2h_{\hat{k}}^{\bar{k}_i}\left|\vec{N}_{\bar{k}_i}\right|}K_{\hat{k}\bar{k}_i}^n - \frac{\langle \vec{\tau}_{\bar{k}_i}^{QT_i}, \overrightarrow{Q\hat{o}_\beta}\rangle}{2h_{\hat{o}_\beta}^{\bar{k}_i}\left|\vec{N}_{\bar{k}_i}\right|}K_{\hat{o}_\beta\bar{k}_i}^n - \frac{1}{2}K_{\hat{k}\bar{k}_i}^{QT_i}\right.\\ &\left. + \frac{1}{2}K_{\hat{o}_\beta\bar{k}_i}^{QT_i}\right]\left(p_{T_j} - p_Q\right) + \frac{\left|\vec{N}_{\bar{k}_i}\right|}{h_{\hat{k}}^{\bar{k}_i}}K_{\hat{k}\bar{k}_i}^n\left(p_{\hat{k}} - p_Q\right)\\ &+ \frac{\left|\vec{N}_{\bar{k}_i}\right|}{h_{\hat{o}_\beta}^{\bar{k}_i}}K_{\hat{o}_\beta\bar{k}_i}^n\left(p_{\hat{o}_\beta} - p_Q\right) = 0\end{aligned} \tag{A.14}$$

that can be simplified as:

$$\eta_{ij}^{\hat{k}}\left(p_{T_i} - p_Q\right) - \eta_{ii}^{\hat{k}}\left(p_{T_j} - p_Q\right) + \sigma_i^{\hat{k}}\left(p_{\hat{k}} - p_Q\right) + \sigma_i^{\hat{o}_\beta}\left(p_{\hat{o}_\beta} - p_Q\right) = 0 \tag{A.15}$$

where:

$$\sigma_i^{\hat{x}} = \frac{\left|\vec{N}_{\bar{k}_i}\right|}{h_{\hat{x}}^{\bar{k}_i}}K_{\hat{x}\bar{k}_i}^n \quad \text{with} \quad x = k, o_\beta \tag{A.16}$$

and:

$$\eta_{ij}^{\hat{k}} = \frac{\langle \vec{\tau}_{\bar{k}_i}^{QT_j}, \overrightarrow{\hat{k}Q} \rangle}{2h_{\hat{k}}^{\bar{k}_i} |\vec{N}_{\bar{k}_i}|} K_{\hat{k}\bar{k}_i}^{n} - \frac{\langle \vec{\tau}_{\bar{k}_i}^{QT_j}, \overrightarrow{Q\hat{o}_\beta} \rangle}{2h_{\hat{o}_\beta}^{\bar{k}_i} |\vec{N}_{\bar{k}_i}|} K_{\hat{o}_\beta\bar{k}_i}^{n} - \frac{1}{2} K_{\hat{k}\bar{k}_i}^{QT_j} + \frac{1}{2} K_{\hat{o}_\beta\bar{k}_i}^{QT_j} \tag{A.17}$$

with $K_{\hat{k}\bar{k}_i}^{n}$ and $K_{\hat{k}\bar{k}_i}^{QT_j}$ and other analogous terms defined according to Eq. (3.44). Finally, $i = 1,2 \rightarrow \beta = J$, $i = 3,4 \rightarrow \beta = I$ and $i = 5,6 \rightarrow \beta = K$. Then, applying the Eq. (A.15) to all the 6 subfaces $\bar{k}_i$ defined according Figure A.1, we have:

$$\begin{cases} \eta_{12}^{\hat{k}}(p_{T_1} - p_Q) - \eta_{11}^{\hat{k}}(p_{T_2} - p_Q) + \sigma_1^{\hat{k}}(p_{\hat{k}} - p_Q) + \sigma_1^{\hat{o}_J}\left(p_{\hat{o}_J} - p_Q\right) = 0 \\ \eta_{23}^{\hat{k}}(p_{T_2} - p_Q) - \eta_{22}^{\hat{k}}(p_{T_3} - p_Q) + \sigma_2^{\hat{k}}(p_{\hat{k}} - p_Q) + \sigma_2^{\hat{o}_J}\left(p_{\hat{o}_J} - p_Q\right) = 0 \\ \eta_{34}^{\hat{k}}(p_{T_3} - p_Q) - \eta_{33}^{\hat{k}}(p_{T_4} - p_Q) + \sigma_3^{\hat{k}}(p_{\hat{k}} - p_Q) + \sigma_3^{\hat{o}_I}(p_{\hat{o}_I} - p_Q) = 0 \\ \eta_{45}^{\hat{k}}(p_{T_4} - p_Q) - \eta_{44}^{\hat{k}}(p_{T_5} - p_Q) + \sigma_4^{\hat{k}}(p_{\hat{k}} - p_Q) + \sigma_4^{\hat{o}_I}(p_{\hat{o}_I} - p_Q) = 0 \\ \eta_{56}^{\hat{k}}(p_{T_5} - p_Q) - \eta_{55}^{\hat{k}}(p_{T_6} - p_Q) + \sigma_5^{\hat{k}}(p_{\hat{k}} - p_Q) + \sigma_5^{\hat{o}_K}(p_{\hat{o}_K} - p_Q) = 0 \\ \eta_{61}^{\hat{k}}(p_{T_6} - p_Q) - \eta_{66}^{\hat{k}}(p_{T_1} - p_Q) + \sigma_6^{\hat{k}}(p_{\hat{k}} - p_Q) + \sigma_6^{\hat{o}_K}(p_{\hat{o}_K} - p_Q) = 0 \end{cases} \tag{A.18}$$

which, in matrix form, we have:

$$\begin{bmatrix} \eta_{12}^{\hat{k}} & -\eta_{11}^{\hat{k}} & 0 & 0 & 0 & 0 \\ 0 & \eta_{23}^{\hat{k}} & -\eta_{22}^{\hat{k}} & 0 & 0 & 0 \\ 0 & 0 & \eta_{34}^{\hat{k}} & -\eta_{33}^{\hat{k}} & 0 & 0 \\ 0 & 0 & 0 & \eta_{45}^{\hat{k}} & -\eta_{44}^{\hat{k}} & 0 \\ 0 & 0 & 0 & 0 & \eta_{56}^{\hat{k}} & -\eta_{55}^{\hat{k}} \\ -\eta_{66}^{\hat{k}} & 0 & 0 & 0 & 0 & \eta_{61}^{\hat{k}} \end{bmatrix} \begin{bmatrix} p_{T_1} - p_Q \\ p_{T_2} - p_Q \\ p_{T_3} - p_Q \\ p_{T_4} - p_Q \\ p_{T_5} - p_Q \\ p_{T_6} - p_Q \end{bmatrix} + \begin{bmatrix} \sigma_1^{\hat{k}} & \sigma_1^{\hat{o}_J} & 0 & 0 \\ \sigma_2^{\hat{k}} & \sigma_2^{\hat{o}_J} & 0 & 0 \\ \sigma_3^{\hat{k}} & 0 & \sigma_3^{\hat{o}_I} & 0 \\ \sigma_4^{\hat{k}} & 0 & \sigma_4^{\hat{o}_I} & 0 \\ \sigma_5^{\hat{k}} & 0 & 0 & \sigma_5^{\hat{o}_K} \\ \sigma_6^{\hat{k}} & 0 & 0 & \sigma_6^{\hat{o}_K} \end{bmatrix} \begin{bmatrix} p_{\hat{k}} - p_Q \\ p_{\hat{o}_J} - p_Q \\ p_{\hat{o}_I} - p_Q \\ p_{\hat{o}_K} - p_Q \end{bmatrix} = \begin{bmatrix} 0 \\ 0 \\ 0 \\ 0 \\ 0 \\ 0 \end{bmatrix} \tag{A.19}$$

Then:

$$\begin{bmatrix} p_{T_1} - p_Q \\ p_{T_2} - p_Q \\ p_{T_3} - p_Q \\ p_{T_4} - p_Q \\ p_{T_5} - p_Q \\ p_{T_6} - p_Q \end{bmatrix} = \mathbf{B}^{\hat{k}} \begin{bmatrix} -\sigma_1^{\hat{k}} & -\sigma_1^{\hat{o}_J} & 0 & 0 \\ -\sigma_2^{\hat{k}} & -\sigma_2^{\hat{o}_J} & 0 & 0 \\ -\sigma_3^{\hat{k}} & 0 & -\sigma_3^{\hat{o}_I} & 0 \\ -\sigma_4^{\hat{k}} & 0 & -\sigma_4^{\hat{o}_I} & 0 \\ -\sigma_5^{\hat{k}} & 0 & 0 & -\sigma_5^{\hat{o}_K} \\ -\sigma_6^{\hat{k}} & 0 & 0 & -\sigma_6^{\hat{o}_K} \end{bmatrix} \begin{bmatrix} p_{\hat{k}} - p_Q \\ p_{\hat{o}_J} - p_Q \\ p_{\hat{o}_I} - p_Q \\ p_{\hat{o}_K} - p_Q \end{bmatrix} \tag{A.20}$$

where:

$$\mathbf{B}^{\hat{k}} = \begin{bmatrix} \eta_{12}^{\hat{k}} & -\eta_{11}^{\hat{k}} & 0 & 0 & 0 & 0 \\ 0 & \eta_{23}^{\hat{k}} & -\eta_{22}^{\hat{k}} & 0 & 0 & 0 \\ 0 & 0 & \eta_{34}^{\hat{k}} & -\eta_{33}^{\hat{k}} & 0 & 0 \\ 0 & 0 & 0 & \eta_{45}^{\hat{k}} & -\eta_{44}^{\hat{k}} & 0 \\ 0 & 0 & 0 & 0 & \eta_{56}^{\hat{k}} & -\eta_{55}^{\hat{k}} \\ -\eta_{66}^{\hat{k}} & 0 & 0 & 0 & 0 & \eta_{61}^{\hat{k}} \end{bmatrix}^{-1} \tag{A.21}$$

This way, each entry of this matrix can be defined as:

$$\begin{cases} \mathrm{B}_{ij}^{\hat{k}} = \left(\dfrac{1}{\prod_{n=1}^{6} \eta_{n\,n+1}^{\hat{k}} - \prod_{n=1}^{6} \eta_{nn}^{\hat{k}}} \right) \left(\prod_{n=1}^{6} \eta_{nn}^{\hat{k}} \dfrac{\prod_{n=j+1}^{i-1} \eta_{n\,n+1}^{\hat{k}}}{\prod_{n=j}^{i-1} \eta_{nn}^{\hat{k}}} \right) & \text{if} \quad i > j \\ \mathrm{B}_{ij}^{\hat{k}} = \left(\dfrac{1}{\prod_{n=1}^{6} \eta_{n\,n+1}^{\hat{k}} - \prod_{n=1}^{6} \eta_{nn}^{\hat{k}}} \right) \left(\prod_{n=1}^{6} \eta_{n\,n+1}^{\hat{k}} \dfrac{\prod_{n=i}^{j-1} \eta_{nn}^{\hat{k}}}{\prod_{n=i}^{j} \eta_{n\,n+1}^{\hat{k}}} \right) & \text{if} \quad i \leq j \end{cases} \tag{A.22}$$

In case of LPEW1, substituting Eq. (A.20) in Eq. (A.8), we have:

$$\mathrm{F}_Q^{\hat{k}} = \left[\mathbf{A}^{\hat{k}}\right]_{1\times 6}^{T} \left[\mathbf{B}^{\hat{k}}\right]_{6\times 6} \begin{bmatrix} -\sigma_1^{\hat{k}} & -\sigma_1^{\hat{o}_J} & 0 & 0 \\ -\sigma_2^{\hat{k}} & -\sigma_2^{\hat{o}_J} & 0 & 0 \\ -\sigma_3^{\hat{k}} & 0 & -\sigma_3^{\hat{o}_I} & 0 \\ -\sigma_4^{\hat{k}} & 0 & -\sigma_4^{\hat{o}_I} & 0 \\ -\sigma_5^{\hat{k}} & 0 & 0 & -\sigma_5^{\hat{o}_K} \\ -\sigma_6^{\hat{k}} & 0 & 0 & -\sigma_6^{\hat{o}_K} \end{bmatrix} \begin{bmatrix} p_{\hat{k}} - p_Q \\ p_{\hat{o}_J} - p_Q \\ p_{\hat{o}_I} - p_Q \\ p_{\hat{o}_K} - p_Q \end{bmatrix} + \mathcal{C}^{\hat{k}} \left(p_{\hat{k}} - p_Q \right) \tag{A.23}$$

which results, through Eq. (A.22), in:

$$\mathrm{F}_{Q}^{\hat{k}} = \begin{bmatrix} -\sum_{j=1}^{6} \sigma_{j}^{\hat{k}} \sum_{i=1}^{6} \mathrm{A}_{i}^{\hat{k}} \mathrm{B}_{ij}^{\hat{k}} \\ -\sum_{j=1}^{2} \sigma_{j}^{\hat{o}_J} \sum_{i=1}^{6} \mathrm{A}_{i}^{\hat{k}} \mathrm{B}_{ij}^{\hat{k}} \\ -\sum_{j=3}^{4} \sigma_{j}^{\hat{o}_I} \sum_{i=1}^{6} \mathrm{A}_{i}^{\hat{k}} \mathrm{B}_{ij}^{\hat{k}} \\ -\sum_{j=5}^{6} \sigma_{j}^{\hat{o}_K} \sum_{i=1}^{6} \mathrm{A}_{i}^{\hat{k}} \mathrm{B}_{ij}^{\hat{k}} \end{bmatrix}^{T} \begin{bmatrix} p_{\hat{k}} - p_Q \\ p_{\hat{o}_J} - p_Q \\ p_{\hat{o}_I} - p_Q \\ p_{\hat{o}_K} - p_Q \end{bmatrix} + \mathcal{C}^{\hat{k}} \left(p_{\hat{k}} - p_Q \right) \tag{A.24}$$

So, imposing the divergence-free condition on Q, according to Eq. (A.2), we have:

$$\sum_{\hat{k} \in \hat{\mathbb{Q}}} \mathrm{F}_{Q}^{\hat{k}} = \sum_{\hat{k} \in \hat{\mathbb{Q}}} \left\{ \left[-\sum_{j=1}^{6} \sigma_{j}^{\hat{k}} \sum_{i=1}^{6} \mathrm{A}_{i}^{\hat{k}} \mathrm{B}_{ij}^{\hat{k}} \right] + \sum_{\beta=I,J,K} \left[-\sum_{j=m_\beta}^{m_\beta+1} \sigma_{j}^{\hat{k}} \sum_{i=1}^{6} \mathrm{A}_{i}^{\hat{o}_\beta} \mathrm{B}_{ij}^{\hat{o}_\beta} \right] + \mathcal{C}^{\hat{k}} \right\} \left(p_{\hat{k}} - p_Q \right) = 0 \tag{A.25}$$

where $m_\beta = 1$ if $\hat{k}$ is opposing the node named as J in $\hat{o}_\beta$, $m_\beta = 3$ if $\hat{k}$ is opposing the node named as I in $\hat{o}_\beta$, $m_\beta = 5$ if $\hat{k}$ is opposing the node named as K in $\hat{o}_\beta$. Thus, we can write the LPEW1 explicit interpolation expression for p_Q:

$$p_Q = \sum_{\hat{k} \in \hat{\mathbb{Q}}} \frac{w_{\hat{k}}}{\sum_{\hat{k} \in \hat{\mathbb{Q}}} w_{\hat{k}}} p_{\hat{k}} \tag{A.26}$$

where:

$$w_{\hat{k}} = \left[-\sum_{j=1}^{6} \sigma_{j}^{\hat{k}} \sum_{i=1}^{6} \mathrm{A}_{i}^{\hat{k}} \mathrm{B}_{ij}^{\hat{k}} \right] + \sum_{\beta=I,J,K} \left[-\sum_{j=m_\beta}^{m_\beta+1} \sigma_{j}^{\hat{k}} \sum_{i=1}^{6} \mathrm{A}_{i}^{\hat{o}_\beta} \mathrm{B}_{ij}^{\hat{o}_\beta} \right] + \mathcal{C}^{\hat{k}} \tag{A.27}$$

with $A_i^{\hat{k}}$ defined as in Eq. (A.9).

However, if the vertex unknown to be interpolated is on a Neumann boundary, we need to consider the prescribed flux in the interpolation. Consider, for example, that the subface $\bar{k}_i$, in $\hat{k}$, is now on a Neumann boundary. Then, we can impose the flux continuity, based in Eq. (A.15), by the following expression:

$$\tilde{\eta}_{ij}^{\hat{k}}\left(p_{T_i}-p_Q\right)-\tilde{\eta}_{ii}^{\hat{k}}\left(p_{T_j}-p_Q\right)+\sigma_i^{\hat{k}}\left(p_{\hat{k}}-p_Q\right)-\mathcal{N}_i^{\hat{k}}=0 \tag{A.28}$$

with:

$$\tilde{\eta}_{ij}^{\hat{k}}=\frac{\langle\vec{\tau}_{\bar{k}_i}^{QT_j},\overrightarrow{\hat{k}Q}\rangle}{2h_{\hat{k}}^{\bar{k}_i}\left|\vec{N}_{\bar{k}_i}\right|}K_{\hat{k}\bar{k}_i}^{n}-\frac{1}{2}K_{\hat{k}\bar{k}_i}^{QT_j} \tag{A.29}$$

For the faces which are not on the boundary, we can define $\tilde{\eta}_{ij}^{\hat{k}}$ in the same way that $\eta_{ij}^{\hat{k}}$ in Eq. (A.17). Besides that:

$$\mathcal{N}_i^{\hat{k}}=\left|\vec{N}_{\bar{k}_i}\right|g_N^{\bar{k}_i} \tag{A.30}$$

where $g_N^{\bar{k}_i}$ is the prescribed flux value (disregarding gravity effects) for the subface $\bar{k}_i$ in $\hat{k}$. Thus, the Eq. (A.19) becomes:

$$\left[\mathbf{H}^{\hat{k}}\right]\begin{bmatrix}p_{T_1}-p_Q\\p_{T_2}-p_Q\\p_{T_3}-p_Q\\p_{T_4}-p_Q\\p_{T_5}-p_Q\\p_{T_6}-p_Q\end{bmatrix}+\left[\mathbf{X}^{\hat{k}}\right]\begin{bmatrix}p_{\hat{k}}-p_Q\\p_{\hat{o}_J}-p_Q\\p_{\hat{o}_I}-p_Q\\p_{\hat{o}_K}-p_Q\end{bmatrix}+\begin{bmatrix}-\left(1-\chi_1^{\hat{k}}\right)\mathcal{N}_1^{\hat{k}}\\-\left(1-\chi_2^{\hat{k}}\right)\mathcal{N}_2^{\hat{k}}\\-\left(1-\chi_3^{\hat{k}}\right)\mathcal{N}_3^{\hat{k}}\\-\left(1-\chi_4^{\hat{k}}\right)\mathcal{N}_4^{\hat{k}}\\-\left(1-\chi_5^{\hat{k}}\right)\mathcal{N}_5^{\hat{k}}\\-\left(1-\chi_6^{\hat{k}}\right)\mathcal{N}_6^{\hat{k}}\end{bmatrix}=\begin{bmatrix}0\\0\\0\\0\\0\\0\end{bmatrix} \tag{A.31}$$

where:

$$\mathbf{H}^{\hat{k}} = \begin{bmatrix} \tilde{\eta}_{12}^{\hat{k}} & -\tilde{\eta}_{11}^{\hat{k}} & 0 & 0 & 0 & 0 \\ 0 & \tilde{\eta}_{23}^{\hat{k}} & -\tilde{\eta}_{22}^{\hat{k}} & 0 & 0 & 0 \\ 0 & 0 & \tilde{\eta}_{34}^{\hat{k}} & -\tilde{\eta}_{33}^{\hat{k}} & 0 & 0 \\ 0 & 0 & 0 & \tilde{\eta}_{45}^{\hat{k}} & -\tilde{\eta}_{44}^{\hat{k}} & 0 \\ 0 & 0 & 0 & 0 & \tilde{\eta}_{56}^{\hat{k}} & -\tilde{\eta}_{55}^{\hat{k}} \\ -\tilde{\eta}_{66}^{\hat{k}} & 0 & 0 & 0 & 0 & \tilde{\eta}_{61}^{\hat{k}} \end{bmatrix} \tag{A.32}$$

and:

$$\mathbf{X}^{\hat{k}} = \begin{bmatrix} \sigma_1^{\hat{k}} & \chi_1^{\hat{k}}\sigma_1^{\hat{o}_J} & 0 & 0 \\ \sigma_2^{\hat{k}} & \chi_2^{\hat{k}}\sigma_2^{\hat{o}_J} & 0 & 0 \\ \sigma_3^{\hat{k}} & 0 & \chi_3^{\hat{k}}\sigma_3^{\hat{o}_I} & 0 \\ \sigma_4^{\hat{k}} & 0 & \chi_4^{\hat{k}}\sigma_4^{\hat{o}_I} & 0 \\ \sigma_5^{\hat{k}} & 0 & 0 & \chi_5^{\hat{k}}\sigma_5^{\hat{o}_K} \\ \sigma_6^{\hat{k}} & 0 & 0 & \chi_6^{\hat{k}}\sigma_6^{\hat{o}_K} \end{bmatrix} \tag{A.33}$$

where $\chi_i^{\hat{k}} = 0$ if the subface $\bar{k}_i$ in $\hat{k}$ is on a Neumann boundary and $\chi_i^{\hat{k}} = 1$ else. Then:

$$\begin{bmatrix} p_{T_1} - p_Q \\ p_{T_2} - p_Q \\ p_{T_3} - p_Q \\ p_{T_4} - p_Q \\ p_{T_5} - p_Q \\ p_{T_6} - p_Q \end{bmatrix} = \widetilde{\mathbf{B}}^{\hat{k}}\left[\mathbf{X}^{\hat{k}}\right] \begin{bmatrix} p_{\hat{k}} - p_Q \\ p_{\hat{o}_J} - p_Q \\ p_{\hat{o}_I} - p_Q \\ p_{\hat{o}_K} - p_Q \end{bmatrix} + \widetilde{\mathbf{B}}^{\hat{k}} \begin{bmatrix} (1-\chi_1^{\hat{k}})\mathcal{N}_1^{\hat{k}} \\ (1-\chi_2^{\hat{k}})\mathcal{N}_2^{\hat{k}} \\ (1-\chi_3^{\hat{k}})\mathcal{N}_3^{\hat{k}} \\ (1-\chi_4^{\hat{k}})\mathcal{N}_4^{\hat{k}} \\ (1-\chi_5^{\hat{k}})\mathcal{N}_5^{\hat{k}} \\ (1-\chi_6^{\hat{k}})\mathcal{N}_6^{\hat{k}} \end{bmatrix} \tag{A.34}$$

in which $\widetilde{\mathbf{B}}^{\hat{k}} = \left[\mathbf{H}^{\hat{k}}\right]^{-1}$. Then, in case of LPEW1, the Eq. (A.24) becomes:

$$\mathrm{F}_Q^{\hat{k}} = \begin{bmatrix} -\sum_{j=1}^{6} \sigma_j^{\hat{k}} \sum_{i=1}^{6} \mathrm{A}_i^{\hat{k}} \widetilde{\mathrm{B}}_{ij}^{\hat{k}} \\ -\sum_{j=1}^{2} \chi_j^{\hat{k}} \sigma_j^{\hat{o}_J} \sum_{i=1}^{6} \mathrm{A}_i^{\hat{k}} \widetilde{\mathrm{B}}_{ij}^{\hat{k}} \\ -\sum_{j=3}^{4} \chi_j^{\hat{k}} \sigma_j^{\hat{o}_I} \sum_{i=1}^{6} \mathrm{A}_i^{\hat{k}} \widetilde{\mathrm{B}}_{ij}^{\hat{k}} \\ -\sum_{j=5}^{6} \chi_j^{\hat{k}} \sigma_j^{\hat{o}_K} \sum_{i=1}^{6} \mathrm{A}_i^{\hat{k}} \widetilde{\mathrm{B}}_{ij}^{\hat{k}} \end{bmatrix}^T \begin{bmatrix} p_{\hat{k}} - p_Q \\ p_{\hat{o}_J} - p_Q \\ p_{\hat{o}_I} - p_Q \\ p_{\hat{o}_K} - p_Q \end{bmatrix} + \mathcal{C}^{\hat{k}} \left(p_{\hat{k}} - p_Q \right) + \sum_{j=1}^{6} \left(1 - \chi_j^{\hat{k}} \right) \mathcal{N}_j^{\hat{k}} \sum_{i=1}^{6} \mathrm{A}_i^{\hat{k}} \widetilde{\mathrm{B}}_{ij}^{\hat{k}} \tag{A.35}$$

where $\widetilde{\mathrm{B}}_{ij}^{\hat{k}}$ defined analogously to $\mathrm{B}_{ij}^{\hat{k}}$ in Eq. (A.22). Then imposing the divergence free surrounding the node Q, now considering the flux through the boundary, we have:

$$\sum_{\hat{k} \in \widehat{\mathbb{Q}}} \mathrm{F}_Q^{\hat{k}} = \sum_{\hat{k} \in \widehat{\mathbb{Q}}} w_k \left(p_{\hat{k}} - p_Q \right) + \sum_{\hat{k} \in \widehat{\mathbb{B}}} \sum_{j=1}^{6} \left(1 - \chi_j^{\hat{k}} \right) \mathcal{N}_j^{\hat{k}} \left(1 + \sum_{i=1}^{6} \mathrm{A}_i^{\hat{k}} \widetilde{\mathrm{B}}_{ij}^{\hat{k}} \right) = 0 \tag{A.36}$$

where:

$$w_k = \left[-\sum_{j=1}^{6} \sigma_j^{\hat{k}} \sum_{i=1}^{6} \mathrm{A}_i^{\hat{k}} \widetilde{\mathrm{B}}_{ij}^{\hat{k}} \right] + \sum_{\beta = I,J,K} \left[-\sum_{j=m_\beta}^{m_\beta + 1} \chi_j^{\hat{k}} \sigma_j^{\hat{k}} \sum_{i=1}^{6} \mathrm{A}_i^{\hat{o}_\beta} \widetilde{\mathrm{B}}_{ij}^{\hat{o}_\beta} \right] + \mathcal{C}^{\hat{k}} \tag{A.37}$$

m_β is defined in the same way that for Eq. (A.25) and $\widehat{\mathbb{B}}$ is the set of boundaries tetrahedra sharing the node Q. Thus, we can write the LPEW1 explicit interpolation expression for p_Q if Q is on a Neumann boundary:

$$p_Q = \sum_{\hat{k} \in \widehat{\mathbb{Q}}} \frac{w_k}{\sum_{\hat{k} \in \widehat{\mathbb{Q}}} w_k} p_{\hat{k}} + \frac{\sum_{\hat{k} \in \widehat{\mathbb{B}}} \sum_{j=1}^{6} \left(1 - \chi_j^{\hat{k}} \right) \mathcal{N}_j^{\hat{k}} \left(1 + \sum_{i=1}^{6} \mathrm{A}_i^{\hat{k}} \widetilde{\mathrm{B}}_{ij}^{\hat{k}} \right)}{\sum_{\hat{k} \in \widehat{\mathbb{Q}}} w_k} \tag{A.38}$$

A.2 Linearity Preserving Explicit Weights Type 2 (LPEW2)

The first strategy is the natural extension, by analogy, to 3-D of the LPEW2 presented by Gao and Wu in 2-D (GAO; WU, 2011), which is also analogous to the LPEW3 presented by Lira Filho et al. (2021). For this, in each tetrahedron sharing Q, we define a subregion delimited by 4 tetrahedrons, as shown in Figure A.3: $\hat{t}_1 = T_1T_2T_6Q$, $\hat{t}_2 = T_2T_3T_4Q$, $\hat{t}_3 = T_4T_5T_6Q$ and $\hat{t}_4 = T_2T_4T_6Q$, where T_1 is on the edge QI, T_2 is on the face QIK, T_3 is on the edge QK, T_4 is on the face QJK, T_5 is on the edge QJ, T_6 is on the face QIJ, where IJK is the opposite face to Q in the k-th tetrahedron sharing it (with a colocation point $\hat{k}$).

Figure A.3 - LPEW2 subregion comprising node Q in $\hat{k}$ (the k-th cell sharing Q).

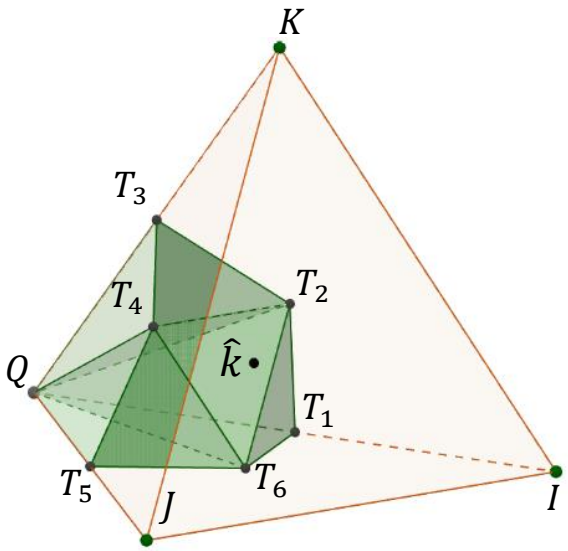

Source: The author (2023).

The points I, J and K are named so that $\vec{N} = (\overrightarrow{JI} \times \overrightarrow{JK})/2$ is the outward area vector of the face IJK. Then, we can also define, in the subregion shown in Figure A.3, the subfaces $\bar{k}_1 = T_1T_2Q$, $\bar{k}_2 = T_2T_3Q$, $\bar{k}_3 = T_3T_4Q$, $\bar{k}_4 = T_4T_5Q$, $\bar{k}_5 = T_5T_6Q$, $\bar{k}_6 = T_6T_1Q$. Beyond this, we also define the faces $\bar{Q}_1 = T_1T_2T_6$, $\bar{Q}_2 = T_2T_3T_4$, $\bar{Q}_3 = T_4T_5T_6$ and $\bar{Q}_4 = T_2T_4T_6$. The neighbor cells sharing faces and the node Q with $\hat{k}$ are named as $\hat{o}_J$ (the neighbor cell sharing the face opposing vertex J), $\hat{o}_I$ (the neighbor cell sharing the face opposing vertex I), $\hat{o}_K$ (the neighbor cell sharing the face opposing vertex K), as shown in Figure A.2a. The method presented by Lira Filho et al. (2021), called LPEW3,

is an variation of the LPEW2 in which $T_1 = I$, $T_3 = K$, $T_5 = J$, T_2 is on edge IK, T_4 is on edge JK and T_6 is on edge IJ.

All this defined, we can start the development of our explicit weighting by the divergence free imposition on the node Q through the Eq. (A.2). If we consider the case of LPEW2, or even LPEW3, (Figure A.3), $\mathrm{F}_Q^{\hat{k}}$ is defined as:

$$\mathrm{F}_Q^{\hat{k}} = \mathrm{F}_{\bar{Q}_1}^{\hat{k}} + \mathrm{F}_{\bar{Q}_2}^{\hat{k}} + \mathrm{F}_{\bar{Q}_3}^{\hat{k}} + \mathrm{F}_{\bar{Q}_4}^{\hat{k}} \tag{A.39}$$

with $\mathrm{F}_{\bar{Q}_1}^{\hat{k}}$ defined, in this case, as:

$$\mathrm{F}_{\bar{Q}_1}^{\hat{k}} = \frac{1}{3\Omega_{\hat{t}_1}} \mathbf{K}_{\hat{k}} \left[\vec{S}_{T_1}^{\hat{t}_1} (p_{T_1} - p_Q) + \vec{S}_{T_2}^{\hat{t}_1} (p_{T_2} - p_Q) + \vec{S}_{T_6}^{\hat{t}_1} (p_{T_6} - p_Q) \right] \cdot \vec{S}_Q^{\hat{t}_1} \tag{A.40}$$

that can be simplified as:

$$\mathrm{F}_{\bar{Q}_1}^{\hat{k}} = \xi_{T_1}^{\hat{k},1} (p_{T_1} - p_Q) + \xi_{T_2}^{\hat{k},1} (p_{T_2} - p_Q) + \xi_{T_6}^{\hat{k},1} (p_{T_6} - p_Q) \tag{A.41}$$

Writing the same expression for $\bar{Q}_2$, $\bar{Q}_3$ and $\bar{Q}_4$, we have:

$$\begin{cases} \mathrm{F}_{\bar{Q}_1}^{\hat{k}} = \xi_{T_1}^{\hat{k},1} (p_{T_1} - p_Q) + \xi_{T_1}^{\hat{k},1} (p_{T_2} - p_Q) + \xi_{T_1}^{\hat{k},1} (p_{T_6} - p_Q) \\ \mathrm{F}_{\bar{Q}_2}^{\hat{k}} = \xi_{T_2}^{\hat{k},2} (p_{T_2} - p_Q) + \xi_{T_3}^{\hat{k},2} (p_{T_3} - p_Q) + \xi_{T_4}^{\hat{k},2} (p_{T_4} - p_Q) \\ \mathrm{F}_{\bar{Q}_3}^{\hat{k}} = \xi_{T_4}^{\hat{k},3} (p_{T_4} - p_Q) + \xi_{T_5}^{\hat{k},3} (p_{T_5} - p_Q) + \xi_{T_6}^{\hat{k},3} (p_{T_6} - p_Q) \\ \mathrm{F}_{\bar{Q}_4}^{\hat{k}} = \xi_{T_2}^{\hat{k},4} (p_{T_2} - p_Q) + \xi_{T_4}^{\hat{k},4} (p_{T_4} - p_Q) + \xi_{T_6}^{\hat{k},4} (p_{T_6} - p_Q) \end{cases} \tag{A.42}$$

Summing these 4 fluxes, following Eq. (A.39), and rewriting the expression in the matrix form, we have the expression for $\mathrm{F}_Q^{\hat{k}}$ to be substituted in Eq. (A.2):

$$\mathrm{F}_Q^{\hat{k}} = \left[\widetilde{\mathbf{A}}^{\hat{k}} \right]^T \begin{bmatrix} p_{T_1} - p_Q \\ p_{T_2} - p_Q \\ p_{T_3} - p_Q \\ p_{T_4} - p_Q \\ p_{T_5} - p_Q \\ p_{T_6} - p_Q \end{bmatrix} \tag{A.43}$$

where, in this case of LPEW2 (or LPEW3), $\widetilde{\mathbf{A}}^{\hat{k}}$ is defined as:

$$\widetilde{\mathbf{A}}^{\hat{k}} = \begin{bmatrix} \xi_{T_1}^{\hat{k},1} \\ \xi_{T_2}^{\hat{k},1} + \xi_{T_2}^{\hat{k},2} + \xi_{T_2}^{\hat{k},4} \\ \xi_{T_3}^{\hat{k},2} \\ \xi_{T_4}^{\hat{k},2} + \xi_{T_4}^{\hat{k},3} + \xi_{T_4}^{\hat{k},4} \\ \xi_{T_5}^{\hat{k},3} \\ \xi_{T_6}^{\hat{k},1} + \xi_{T_6}^{\hat{k},3} + \xi_{T_6}^{\hat{k},4} \end{bmatrix} \tag{A.44}$$

Substituting Eq. (A.20) in Eq. (A.43), we have:

$$\mathrm{F}_Q^{\hat{k}} = \left[\widetilde{\mathbf{A}}^{\hat{k}}\right]_{1\times 6}^{T} \left[\mathbf{B}^{\hat{k}}\right]_{6\times 6} \begin{bmatrix} -\sigma_1^{\hat{k}} & -\sigma_1^{\hat{o}_J} & 0 & 0 \\ -\sigma_2^{\hat{k}} & -\sigma_2^{\hat{o}_J} & 0 & 0 \\ -\sigma_3^{\hat{k}} & 0 & -\sigma_3^{\hat{o}_I} & 0 \\ -\sigma_4^{\hat{k}} & 0 & -\sigma_4^{\hat{o}_I} & 0 \\ -\sigma_5^{\hat{k}} & 0 & 0 & -\sigma_5^{\hat{o}_K} \\ -\sigma_6^{\hat{k}} & 0 & 0 & -\sigma_6^{\hat{o}_K} \end{bmatrix} \begin{bmatrix} p_{\hat{k}} - p_Q \\ p_{\hat{o}_J} - p_Q \\ p_{\hat{o}_I} - p_Q \\ p_{\hat{o}_K} - p_Q \end{bmatrix} \tag{A.45}$$

which results, through Eq. (A.22), in:

$$\mathrm{F}_Q^{\hat{k}} = \begin{bmatrix} -\sum_{j=1}^{6} \sigma_j^{\hat{k}} \sum_{i=1}^{6} \widetilde{\mathrm{A}}_i^{\hat{k}} \mathrm{B}_{ij}^{\hat{k}} \\ -\sum_{j=1}^{2} \sigma_j^{\hat{o}_J} \sum_{i=1}^{6} \widetilde{\mathrm{A}}_i^{\hat{k}} \mathrm{B}_{ij}^{\hat{k}} \\ -\sum_{j=3}^{4} \sigma_j^{\hat{o}_I} \sum_{i=1}^{6} \widetilde{\mathrm{A}}_i^{\hat{k}} \mathrm{B}_{ij}^{\hat{k}} \\ -\sum_{j=5}^{6} \sigma_j^{\hat{o}_K} \sum_{i=1}^{6} \widetilde{\mathrm{A}}_i^{\hat{k}} \mathrm{B}_{ij}^{\hat{k}} \end{bmatrix}^{T} \begin{bmatrix} p_{\hat{k}} - p_Q \\ p_{\hat{o}_J} - p_Q \\ p_{\hat{o}_I} - p_Q \\ p_{\hat{o}_K} - p_Q \end{bmatrix} \tag{A.46}$$

So, imposing the divergence-free condition on Q, according to Eq. (A.2), we have:

$$\sum_{\hat{k}\in\hat{\mathbb{Q}}} \mathrm{F}_Q^{\hat{k}} = \sum_{\hat{k}\in\hat{\mathbb{Q}}} \left\{ \left[-\sum_{j=1}^{6} \sigma_j^{\hat{k}} \sum_{i=1}^{6} \widetilde{\mathrm{A}}_i^{\hat{k}} \mathrm{B}_{ij}^{\hat{k}} \right] + \sum_{\beta=I,J,K} \left[-\sum_{j=m_\beta}^{m_\beta+1} \sigma_j^{\hat{k}} \sum_{i=1}^{6} \widetilde{\mathrm{A}}_i^{\hat{o}_\beta} \mathrm{B}_{ij}^{\hat{o}_\beta} \right] \right\} \left(p_{\hat{k}} - p_Q \right) = 0 \tag{A.47}$$

where again $m_\beta = 1$ if $\hat{k}$ is opposing the node named as J in $\hat{o}_\beta$, $m_\beta = 3$ if $\hat{k}$ is opposing the node named as I in $\hat{o}_\beta$, $m_\beta = 5$ if $\hat{k}$ is opposing the node named as K in $\hat{o}_\beta$. Thus, we can write the LPEW2 explicit interpolation expression for p_Q:

$$p_Q = \sum_{\hat{k}\in\hat{\mathbb{Q}}} \frac{\widetilde{w}_k}{\sum_{\hat{k}\in\hat{\mathbb{Q}}} \widetilde{w}_k} p_{\hat{k}} \tag{A.48}$$

where:

$$\widetilde{w}_k = \left[-\sum_{j=1}^{6} \sigma_j^{\hat{k}} \sum_{i=1}^{6} \widetilde{\mathrm{A}}_i^{\hat{k}} \mathrm{B}_{ij}^{\hat{k}} \right] + \sum_{\beta=I,J,K} \left[-\sum_{j=m_\beta}^{m_\beta+1} \sigma_j^{\hat{k}} \sum_{i=1}^{6} \widetilde{\mathrm{A}}_i^{\hat{o}_\beta} \mathrm{B}_{ij}^{\hat{o}_\beta} \right] \tag{A.49}$$

with $\widetilde{\mathrm{A}}_i^{\hat{k}}$ defined as in Eq (A.44).

In case of the node being on a Neumann boundary condition, through the application of Eq. (A.34) in Eq. (A.43), the Eq. (A.46) becomes:

$$\mathrm{F}_Q^{\hat{k}} = \begin{bmatrix} -\sum_{j=1}^{6} \sigma_j^{\hat{k}} \sum_{i=1}^{6} \widetilde{\mathrm{A}}_i^{\hat{k}} \widetilde{\mathrm{B}}_{ij}^{\hat{k}} \\ -\sum_{j=1}^{2} \chi_j^{\hat{k}} \sigma_j^{\hat{o}_J} \sum_{i=1}^{6} \widetilde{\mathrm{A}}_i^{\hat{k}} \widetilde{\mathrm{B}}_{ij}^{\hat{k}} \\ -\sum_{j=3}^{4} \chi_j^{\hat{k}} \sigma_j^{\hat{o}_I} \sum_{i=1}^{6} \widetilde{\mathrm{A}}_i^{\hat{k}} \widetilde{\mathrm{B}}_{ij}^{\hat{k}} \\ -\sum_{j=5}^{6} \chi_j^{\hat{k}} \sigma_j^{\hat{o}_K} \sum_{i=1}^{6} \widetilde{\mathrm{A}}_i^{\hat{k}} \widetilde{\mathrm{B}}_{ij}^{\hat{k}} \end{bmatrix}^T \begin{bmatrix} p_{\hat{k}} - p_Q \\ p_{\hat{o}_J} - p_Q \\ p_{\hat{o}_I} - p_Q \\ p_{\hat{o}_K} - p_Q \end{bmatrix} + \sum_{j=1}^{6} \left(1 - \chi_j^{\hat{k}}\right) \mathcal{N}_j^{\hat{k}} \sum_{i=1}^{6} \widetilde{\mathrm{A}}_i^{\hat{k}} \widetilde{\mathrm{B}}_{ij}^{\hat{k}} \tag{A.50}$$

where again $\widetilde{\mathrm{B}}_{ij}^{\hat{k}}$ is defined analogously to $\mathrm{B}_{ij}^{\hat{k}}$ in Eq. (A.22). Then imposing the divergence free surrounding the node Q, now considering the flux through the boundary, we have:

$$\sum_{\hat{k}\in\widehat{\mathbb{Q}}} \mathrm{F}_Q^{\hat{k}} = \sum_{\hat{k}\in\widehat{\mathbb{Q}}} \widetilde{w}_k\left(p_{\hat{k}} - p_Q\right) + \sum_{\hat{k}\in\widehat{\mathbb{B}}}\sum_{j=1}^{6}\left(1-\chi_j^{\hat{k}}\right)\mathcal{N}_j^{\hat{k}}\left(1+\sum_{i=1}^{6}\widetilde{\mathrm{A}}_i^{\hat{k}}\widetilde{\mathrm{B}}_{ij}^{\hat{k}}\right) = 0 \qquad \text{(A.51)}$$

where:

$$\widetilde{w}_k = \left[-\sum_{j=1}^{6}\sigma_j^{\hat{k}}\sum_{i=1}^{6}\widetilde{\mathrm{A}}_i^{\hat{k}}\widetilde{\mathrm{B}}_{ij}^{\hat{k}}\right] + \sum_{\beta=I,J,K}\left[-\sum_{j=m_\beta}^{m_\beta+1}\chi_j^{\hat{k}}\sigma_j^{\hat{k}}\sum_{i=1}^{6}\widetilde{\mathrm{A}}_i^{\hat{O}_\beta}\widetilde{\mathrm{B}}_{ij}^{\hat{O}_\beta}\right] \qquad \text{(A.52)}$$

and m_β is defined in the same way that for Eq. (A.47) and $\widehat{\mathbb{B}}$ is the set of boundaries tetrahedra sharing the node Q. Thus, we can write the LPEW2 explicit interpolation expression for p_Q if Q is on a Neumann boundary:

$$p_Q = \sum_{\hat{k}\in\widehat{\mathbb{Q}}}\frac{\widetilde{w}_k}{\sum_{\hat{k}\in\widehat{\mathbb{Q}}}\widetilde{w}_k}p_{\hat{k}} + \frac{\sum_{\hat{k}\in\widehat{\mathbb{B}}}\sum_{j=1}^{6}\left(1-\chi_j^{\hat{k}}\right)\mathcal{N}_j^{\hat{k}}\left(1+\sum_{i=1}^{6}\widetilde{\mathrm{A}}_i^{\hat{k}}\widetilde{\mathrm{B}}_{ij}^{\hat{k}}\right)}{\sum_{\hat{k}\in\widehat{\mathbb{Q}}}\widetilde{w}_k} \qquad \text{(A.53)}$$

A.3 Global Least Square (GLS)

The Global Least Square (GLS) interpolation was presented by Dong ang Kang (2021, 2022) and give us another interpolation for p_Q that is linearity preserving under some conditions they detailed in their papers. Consider that the node Q is shared by $n_{\widehat{\mathbb{Q}}}$ cells, $n_{\overline{\mathbb{Q}}}$ faces and that there are $n_{\mathbb{Q}}$ nodes sharing faces with it. Thus, a piecewise linear approximation for pressure in the i-th cell surrounding Q, $P_{\hat{\imath}}(\vec{x}_{\hat{\imath}})$, can be introduced as follows:

$$P_{\hat{\imath}}(\vec{x}_{\hat{\imath}}) = \left(\vec{x}_{\hat{\imath}} - \vec{x}_Q\right)^T\nabla p_{\hat{\imath}} + p_Q \;\; \forall \;\; 1 \le i \le n \qquad \text{(A.54)}$$

in which $\vec{x}_Q$ and $\vec{x}_{\hat{\imath}}$ are the position vectors of Q and of the centroid of the i-th cell surrounding Q. Then we define the functions we intend to minimize:

$$\begin{cases} \delta P_{\hat{\imath}} = P_{\hat{\imath}}(\vec{x}_{\hat{\imath}}) - p_{\hat{\imath}} \\ \delta G_i = \left(\vec{x}_i - \vec{x}_Q\right)^T (\nabla p_{\hat{L}} - \nabla p_{\hat{R}}) \\ \delta V_{\bar{\jmath}} = \vec{n}_{\bar{\jmath}}^T (\mathbf{K}_{\hat{L}} \nabla p_{\hat{L}} - \mathbf{K}_{\hat{R}} \nabla p_{\hat{R}}) \end{cases} \tag{A.55}$$

where the L-th and R-th cells surrounding Q are sharing the i-th node and the j-th face surrounding Q. In addition, $\vec{n}_{\bar{\jmath}}$ is the unitary normal vector of the j-th face surrounding node Q and $\vec{x}_i$ is the position vector of the i-th node surrounding node Q. All the position vectors are column vectors. Imposing $\delta P_{\hat{\imath}} = 0$ and writing its equation for all the grid cells surrounding Q, imposing $\delta G_i = 0$ and writing its equation for all the nodes surrounding Q, and, finally, imposing $\delta V_{\bar{\jmath}} = 0$ and writing its equation (continuity imposition) for all the faces surrounding Q, we obtain a system of equations that can be written as:

$$\boldsymbol{M} \begin{bmatrix} \nabla p_{\hat{1}} \\ \nabla p_{\hat{2}} \\ \dots \\ \nabla p_{\hat{n}} \\ p_Q \end{bmatrix} = \boldsymbol{N} \begin{bmatrix} p_{\hat{1}} \\ p_{\hat{2}} \\ \dots \\ p_{\hat{n}} \end{bmatrix} \tag{A.56}$$

with $\boldsymbol{M}$ being a sparse matrix defined as:

$$\boldsymbol{M}_{\left(n_{\bar{\mathbb{Q}}}+n_{\bar{\mathbb{Q}}}+n_{\mathbb{Q}}\right)\times\left(3n_{\bar{\mathbb{Q}}}+1\right)} = \begin{bmatrix} [\boldsymbol{M}_1]_{n_{\mathbb{Q}}\times\left(3n_{\bar{\mathbb{Q}}}+1\right)} \\ [\boldsymbol{M}_2]_{n_{\mathbb{Q}}\times\left(3n_{\bar{\mathbb{Q}}}+1\right)} \\ [\boldsymbol{M}_3]_{n_{\bar{\mathbb{Q}}}\times\left(3n_{\bar{\mathbb{Q}}}+1\right)} \end{bmatrix} \tag{A.57}$$

in which the entries of $\boldsymbol{M}_1$, $\boldsymbol{M}_2$ and $\boldsymbol{M}_3$ are defined by the following expressions.

$$\begin{cases} [\boldsymbol{M}_1]_{i,3(i-1)+1:3(i-1)+3} = \left(\vec{x}_{\hat{\imath}} - \vec{x}_Q\right)^T \\ [\boldsymbol{M}_1]_{i,3n_{\bar{\mathbb{Q}}}+1} = 1 \end{cases} \tag{A.58}$$

Beyond this:

$$\begin{cases} [\boldsymbol{M}_2]_{i,3(R-1)+1:3(R-1)+3} = -\left(\vec{x}_i - \vec{x}_Q\right)^T \\ [\boldsymbol{M}_2]_{i,3(L-1)+1:3(L-1)+3} = \left(\vec{x}_i - \vec{x}_Q\right)^T \end{cases} \tag{A.59}$$

Moreover:

$$\begin{cases} [\boldsymbol{M}_3]_{i,3(R-1)+1:3(R-1)+3} = -\vec{n}_i^T \mathbf{K}_{\hat{R}} \\ [\boldsymbol{M}_3]_{i,3(L-1)+1:3(L-1)+3} = \vec{n}_i^T \mathbf{K}_{\hat{L}} \end{cases} \tag{A.60}$$

In addition to that, we need to define the entries of $\boldsymbol{N}_{\left(n_{\mathbb{Q}}+n_{\bar{\mathbb{Q}}}+n_{\mathbb{Q}}\right)\times n_{\mathbb{Q}}}$ as:

$$\begin{cases} N_{i,i} = 1 \\ N_{i,j} = 0 \; \forall \; i \neq j \end{cases} \tag{A.61}$$

Then, from the solution of the system in Eq. (A.56), we can get the expression defining the weights of the GLS interpolation:

$$\omega_{1\times n_{\hat{\mathbb{Q}}}} = [0 \quad \dots \quad 0 \quad 1]_{1\times\left(3n_{\hat{\mathbb{Q}}}+1\right)} (\boldsymbol{M}^T\boldsymbol{M})^{-1}\boldsymbol{M}^T\boldsymbol{N} \tag{A.62}$$

to be applied in the following equation:

$$p_Q = \omega_{1\times n_{\hat{\mathbb{Q}}}} \begin{bmatrix} p_{\hat{1}} \\ p_{\hat{2}} \\ \dots \\ p_{\hat{n}} \end{bmatrix} \tag{A.63}$$

In the case of Q being on a Neumann boundary, the Eq. (A.56) is modified as follows:

$$\widetilde{\boldsymbol{M}} \begin{bmatrix} \nabla p_{\hat{1}} \\ \nabla p_{\hat{2}} \\ \dots \\ \nabla p_{\hat{n}} \\ p_Q \end{bmatrix} = \boldsymbol{N} \begin{bmatrix} p_{\hat{1}} \\ p_{\hat{2}} \\ \dots \\ p_{\hat{n}} \end{bmatrix} + \boldsymbol{F} \tag{A.64}$$

in which $\widetilde{\boldsymbol{M}}$ is defined as a modification of $\boldsymbol{M}$ defined as:

$$\widetilde{\boldsymbol{M}}_{\left(n_{\hat{\mathbb{Q}}}+n_{\bar{\mathbb{Q}}}+n_{\dot{\mathbb{Q}}}\right)\times\left(3n_{\hat{\mathbb{Q}}}+1\right)}=\begin{bmatrix}[\boldsymbol{M}_1]_{n_{\hat{\mathbb{Q}}}\times\left(3n_{\hat{\mathbb{Q}}}+1\right)}\\ [\widetilde{\boldsymbol{M}}_2]_{n_{\dot{\mathbb{Q}}}\times\left(3n_{\hat{\mathbb{Q}}}+1\right)}\\ [\widetilde{\boldsymbol{M}}_3]_{n_{\bar{\mathbb{Q}}}\times\left(3n_{\hat{\mathbb{Q}}}+1\right)}\end{bmatrix} \tag{A.65}$$

where $\widetilde{\boldsymbol{M}}_2$ is defined using only the $n_{\dot{\mathbb{Q}}}$ internal nodes surrounding Q and $\widetilde{\boldsymbol{M}}_3$ is defined as:

$$\begin{cases}[\widetilde{\boldsymbol{M}}_3]_{i,3(R-1)+1:3(R-1)+3}=0\\ [\widetilde{\boldsymbol{M}}_3]_{i,3(L-1)+1:3(L-1)+3}=\vec{n}_{\bar{\imath}}^{T}\mathbf{K}_{\hat{L}}\end{cases} \tag{A.66}$$

and $\boldsymbol{F}$ is defined as:

$$\boldsymbol{F}_{\left(n_{\hat{\mathbb{Q}}}+n_{\bar{\mathbb{Q}}}+n_{\dot{\mathbb{Q}}}\right)\times1}=\begin{bmatrix}[\boldsymbol{F}_1]_{\left(n_{\hat{\mathbb{Q}}}+n_{\dot{\mathbb{Q}}}\right)\times1}\\ [\boldsymbol{F}_2]_{n_{\bar{\mathbb{Q}}}\times1}\end{bmatrix} \tag{A.67}$$

where $\boldsymbol{F}_1$ and $\boldsymbol{F}_2$ are defined by:

$$\begin{cases}[F_1]_i=0\\ [F_2]_i=\left|\vec{N}_{\bar{\imath}}\right|g_N\ \forall\ \bar{\imath}\in\Gamma_m^N\\ [F_2]_i=0\ \forall\ \bar{\imath}\notin\Gamma_m^N\end{cases} \tag{A.68}$$

Then, the Eq. (A.63) becomes:

$$p_Q=\omega_{1\times n_{\hat{\mathbb{Q}}}}\begin{bmatrix}p_{\hat{1}}\\ p_{\hat{2}}\\ \dots\\ p_{\hat{n}}\end{bmatrix}+[0\quad\dots\quad0\quad1]_{1\times\left(3n_{\hat{\mathbb{Q}}}+1\right)}\left(\widetilde{\boldsymbol{M}}^T\widetilde{\boldsymbol{M}}\right)^{-1}\widetilde{\boldsymbol{M}}^T\boldsymbol{F} \tag{A.69}$$

with:

$$\omega_{1\times n_{\hat{\mathbb{Q}}}}=[0\quad\dots\quad0\quad1]_{1\times\left(3n_{\hat{\mathbb{Q}}}+1\right)}\left(\widetilde{\boldsymbol{M}}^T\widetilde{\boldsymbol{M}}\right)^{-1}\widetilde{\boldsymbol{M}}^T\boldsymbol{N} \tag{A.70}$$

A.4 Linearity Preserving Explicit Weights Based on Harmonic Averaging Points (LPEW-HAP)

The linearity preserving explicit weighting strategy based on harmonic averaging points (LPEW-HAP) was presented by Yang and Gao (2020). This strategy can also achieve second order accuracy depending on the mesh. This strategy, as mentioned, is based on harmonic averaging points, which is necessary to be defined for all the faces sharing the node to be interpolated (Q). Considering the configuration shown in Figure A.2a, the harmonic points are defined on the faces of $\hat{k}$ sharing Q by the following expression:

$$\bar{\bar{k}}_\beta = \frac{\mathcal{H}_{\hat{k}\bar{k}_\beta}\vec{x}_{\hat{k}} + \mathcal{H}_{\hat{o}_\beta\bar{k}_\beta}\vec{x}_{\hat{o}_\beta} + \left(\mathbf{K}_{\hat{k}} - \mathbf{K}_{\hat{o}_\beta}\right)\vec{n}_{\bar{k}_\beta}}{\mathcal{H}_{\hat{k}\bar{k}_\beta} + \mathcal{H}_{\hat{o}_\beta\bar{k}_\beta}} \tag{A.71}$$

in which $\bar{k}_\beta$ is the face shared by $\hat{k}$ and $\hat{o}_\beta$ with $\beta = I, J, K$. Beyond this:

$$\mathcal{H}_{\hat{k}\bar{k}_\beta} = \frac{K^n_{\hat{k}\bar{k}_\beta}}{h^{\bar{k}_\beta}_{\hat{k}}} \tag{A.72}$$

with $K^n_{\hat{k}\bar{k}_\beta}$ defined according to Eq. (3.44). Thus:

$$p_{\bar{\bar{k}}_\beta} = \left(w^{\hat{o}_\beta}_{\hat{k}}\right)p_{\hat{k}} + \left(1 - w^{\hat{o}_\beta}_{\hat{k}}\right)p_{\hat{o}_\beta} \tag{A.73}$$

with:

$$w^{\hat{o}_\beta}_{\hat{k}} = \frac{\mathcal{H}_{\hat{k}\bar{k}_\beta}}{\mathcal{H}_{\hat{k}\bar{k}_\beta} + \mathcal{H}_{\hat{o}_\beta\bar{k}_\beta}} \tag{A.74}$$

with $\mathcal{H}_{\hat{o}_\beta\bar{k}_\beta}$ calculated analogously to Eq. (A.72). This way, the pressure at Q can be approximated, with respect to $\hat{k}$, as:

$$p_Q^{\hat{k}} = \varphi_{\hat{k}}^{\hat{k}} p_{\hat{k}} + \varphi_{\hat{k}}^{\hat{o}_I} p_{\bar{\bar{k}}_I} + \varphi_{\hat{k}}^{\hat{o}_J} p_{\bar{\bar{k}}_J} + \varphi_{\hat{k}}^{\hat{o}_K} p_{\bar{\bar{k}}_K} \tag{A.75}$$

in which $\varphi_{\hat{k}}^{\hat{k}}$ and $\varphi_{\hat{k}}^{\hat{o}_\beta}$ are linear basis functions defined as:

$$\varphi_{\hat{k}}^{\hat{k}} = \frac{\psi_{\hat{k}}^{\hat{k}}}{\Psi_{\hat{k}}};\ \varphi_{\hat{k}}^{\hat{o}_\beta} = \frac{\psi_{\hat{k}}^{\hat{o}_\beta}}{\Psi_{\hat{k}}}; \tag{A.76}$$

with:

$$\begin{gathered}
\psi_{\hat{k}}^{\hat{k}} = \det\begin{bmatrix} Q_x & \bar{\bar{k}}_{Ix} & \bar{\bar{k}}_{Jx} & \bar{\bar{k}}_{Kx} \\ Q_y & \bar{\bar{k}}_{Iy} & \bar{\bar{k}}_{Jy} & \bar{\bar{k}}_{Ky} \\ Q_z & \bar{\bar{k}}_{Iz} & \bar{\bar{k}}_{Jz} & \bar{\bar{k}}_{Kz} \\ 1 & 1 & 1 & 1 \end{bmatrix};\ \psi_{\hat{k}}^{\hat{o}_I} = \det\begin{bmatrix} \hat{k}_x & Q_x & \bar{\bar{k}}_{Jx} & \bar{\bar{k}}_{Kx} \\ \hat{k}_y & Q_y & \bar{\bar{k}}_{Jy} & \bar{\bar{k}}_{Ky} \\ \hat{k}_z & Q_z & \bar{\bar{k}}_{Jz} & \bar{\bar{k}}_{Kz} \\ 1 & 1 & 1 & 1 \end{bmatrix}; \\
\psi_{\hat{k}}^{\hat{o}_J} = \det\begin{bmatrix} \hat{k}_x & \bar{\bar{k}}_{Ix} & Q_x & \bar{\bar{k}}_{Kx} \\ \hat{k}_y & \bar{\bar{k}}_{Iy} & Q_y & \bar{\bar{k}}_{Ky} \\ \hat{k}_z & \bar{\bar{k}}_{Iz} & Q_z & \bar{\bar{k}}_{Kz} \\ 1 & 1 & 1 & 1 \end{bmatrix};\ \psi_{\hat{k}}^{\hat{o}_K} = \det\begin{bmatrix} \hat{k}_x & \bar{\bar{k}}_{Ix} & \bar{\bar{k}}_{Jx} & Q_x \\ \hat{k}_y & \bar{\bar{k}}_{Iy} & \bar{\bar{k}}_{Jy} & Q_y \\ \hat{k}_z & \bar{\bar{k}}_{Iz} & \bar{\bar{k}}_{Jz} & Q_z \\ 1 & 1 & 1 & 1 \end{bmatrix}; \\
\Psi_{\hat{k}} = \det\begin{bmatrix} \hat{k}_x & \bar{\bar{k}}_{Ix} & \bar{\bar{k}}_{Jx} & \bar{\bar{k}}_{Kx} \\ \hat{k}_y & \bar{\bar{k}}_{Iy} & \bar{\bar{k}}_{Jy} & \bar{\bar{k}}_{Ky} \\ \hat{k}_z & \bar{\bar{k}}_{Iz} & \bar{\bar{k}}_{Jz} & \bar{\bar{k}}_{Kz} \\ 1 & 1 & 1 & 1 \end{bmatrix};
\end{gathered} \tag{A.77}$$

Then, performing an average mean of the approximations indicated in Eq. (A.75), considering all the $\hat{k} \in \widehat{\mathbb{Q}}$, we can get:

$$p_Q = \frac{1}{n_{\widehat{\mathbb{Q}}}} \sum_{\hat{k} \in \widehat{\mathbb{Q}}} p_Q^{\hat{k}} \tag{A.78}$$

expression which can be rewritten from the terms $p_{\hat{k}}$ as:

$$p_Q = \sum_{\hat{k} \in \widehat{\mathbb{Q}}} \omega_{\hat{k}} p_{\hat{k}} \tag{A.79}$$

with:

$$\omega_{\hat{k}} = \frac{1}{n_{\mathbb{Q}}}\Big[\varphi_{\hat{k}}^{\hat{k}} + w_{\hat{k}}^{\hat{o}_I}\varphi_{\hat{k}}^{\hat{o}_I} + w_{\hat{k}}^{\hat{o}_J}\varphi_{\hat{k}}^{\hat{o}_J} + w_{\hat{k}}^{\hat{o}_K}\varphi_{\hat{k}}^{\hat{o}_K} + \left(1 - w_{\hat{o}_I}^{\hat{k}}\right)\varphi_{\hat{o}_I}^{\hat{k}} + \left(1 - w_{\hat{o}_J}^{\hat{k}}\right)\varphi_{\hat{o}_J}^{\hat{k}} + \left(1 - w_{\hat{o}_K}^{\hat{k}}\right)\varphi_{\hat{o}_K}^{\hat{k}}\Big] \tag{A.80}$$

In the case of Q being on a Neumann boundary, we follow the development shown in Eq. (A.64) to Eq. (A.70).